

# Resonant optical trapping in hollow photonic crystal cavities and its potential use for bacterial characterisation

Thèse N° 9661

Présentée le 12 août 2019  
à la Faculté des sciences de base  
Groupe SCI SB RH  
Programme doctoral en physique

pour l'obtention du grade de Docteur ès Sciences

par

**Rita THERISOD**

Acceptée sur proposition du jury  
Prof. V. Savona, président du jury  
Prof. R. Houdré, directeur de thèse  
Prof. F. Marabelli, rapporteur  
Dr P. Marcoux, rapporteur  
Prof. N. Grandjean, rapporteur

2019





# Abstract

During the last decade, the development of optofluidic chips has become a large field of research. The integration of nano and microstructures with microfluidics layers allowed for the miniaturisation of a number of tools traditionally used in laboratories and optofluidic systems found their main applications in lab-on-a-chip and sensing platforms. At the same time, optical tweezers have become the tool of choice for the trapping and the manipulation of nano and micrometer-sized objects, that can be inert (dielectric or metallic particles) or biological (proteins, bacteria, viruses,...). In this context, nanostructures are the ideal candidate for tweezers miniaturisation, thanks to their ability to strongly confine light in small volumes and hence to generate intense gradient forces. This work reports on the fabrication of an optofluidic chip based on a two-dimensional photonic crystal cavity and on its use in particle and bacteria differentiation. The cavity has a hollow design that maximises the overlap between the confined field and the trapped objects and it supports Self-Induced Back-Action effects that allow for reducing the trapping power (down to few microwatts) and to simultaneously acquire information of the trapped specimen. The system is excited in an end-fire setup and the detection is carried out by recording the light intensity transmitted through the photonic crystal. The fabrication process, that is entirely carried out in the Institutue of Physics and in the Center of MicroNanoTechnology cleanrooms, is first detailed. For the cavity design normally used, typical quality factors of 10000 were obtained. Moreover, SU8 mode adaptors were developed to increase the coupling with lensed fibers and a microfluidic membrane presenting two injection channels is proposed for rapid switch between liquids. The trapping and the differentiation of 250 and 500 nm polystyrene is then presented. The differentiation can be achieved qualitatively by direct observation of the transmitted intensity records and quantitatively by the use of histograms and of statistical moments. Finally, the trapping of seven species of living bacteria is shown and their Gram-type is determined by the analysis of the induced transmission increase. This ability to probe the cell wall of bacteria in a fast, label-free and non-destructive way paves the way for applications in biological and biomedical environments.



# Résumé

Pendant la dernière décennie, le développement de puces optofluidiques est devenu un important domaine de recherche. L'intégration de nano et de microstructures avec des couches microfluidiques a permis la miniaturisation de nombreux outils habituellement utilisés dans les laboratoires et les systèmes optofluidiques ont trouvé leurs applications naturelles dans des dispositifs de type laboratoire sur puce et de détection. En même temps, les pinces optiques sont devenues l'outil le plus répandu pour le piégeage et la manipulation d'objets dont la taille est de l'ordre du nanomètre et du micromètre, qui peuvent être à la fois inertes (particules diélectrique ou métallique) ou biologiques (protéines, bactéries, virus,..). Dans ce contexte, les nanostructures sont des candidats idéaux pour la miniaturisation de pinces optiques, grâce à leur capacité à confiner fortement la lumière dans de très petits volumes, créant ainsi les nécessaires forces de gradient. Cette thèse décrit la fabrication d'une puce optofluidique basée sur une cavité à cristal photonique et son utilisation dans la différenciation de particules et de bactéries. Une des caractéristiques principales de cette cavité est d'être creuse, ce qui permet de maximiser la superposition entre le champs confiné et les objets piégés. De plus, elle supporte des effets de rétroaction, ce qui conduit à une forte réduction des puissances nécessaires au piégeage et en même temps à l'obtention d'informations sur l'échantillon piégé. Le système est excité par un laser accordable et la détection est faite en mesurant la puissance transmise à travers le cristal photonique. Les étapes de fabrication, qui sont exécutées entièrement dans les salles blanches de l'Institut de Physique et du Centre de MicroNanoTechnologie ici à l'EPFL, sont d'abord détaillées. Pour les cavités utilisées habituellement, des facteurs de qualité de 10000 ont été obtenus. De plus, des adaptateurs de modes en SU8 ont été développés pour augmenter le couplage avec les fibres lentillées pour l'injection de la lumière. Une membrane microfluidique avec deux canaux d'injection a également été proposée, pour changer rapidement de liquide pendant les manipulations. Ensuite, le piégeage de particules en polystyrène avec des diamètres de 250 et de 500 nm est présenté. Les deux tailles peuvent être distinguées qualitativement par la simple observation de l'intensité transmise et quantitativement par l'utilisation d'histogrammes et de moments statistiques. Finalement, le piégeage de sept espèces bactériennes est montré et leur type de Gram est déterminé grâce à l'analyse de l'augmentation de l'intensité transmise. Cette faculté à sonder la membrane cellulaire bactérienne de façon rapide, non-destructive et sans besoin de marquages ouvre la route pour nombreuses applications dans les domaines biologiques et biomédicaux.



# Contents

<b>Abstracts (English/Français)</b>	<b>i</b>
<b>List of figures</b>	<b>vii</b>
<b>Table of symbols and acronyms</b>	<b>xi</b>
<b>1 Introduction</b>	<b>1</b>
1.1 Photonic crystals . . . . .	3
1.1.1 Band structure and photonic band gap . . . . .	4
1.1.2 Defects in 2D photonic crystals . . . . .	6
1.1.3 Q factor and modal volume . . . . .	7
1.1.4 2D hollow photonic crystal cavity . . . . .	8
1.2 Optical trapping . . . . .	9
1.2.1 Optical forces . . . . .	9
1.2.2 Dipole and ray-optics approximations . . . . .	11
1.3 Nanostructures for optical trapping . . . . .	14
1.3.1 Backaction . . . . .	15
1.4 Optofluidic chip . . . . .	17
<b>2 Fabrication</b>	<b>19</b>
2.1 Process overview . . . . .	19
2.2 Lithographic techniques . . . . .	20
2.3 Cr masks fabrication . . . . .	21
2.4 Electron beam lithography . . . . .	22
2.4.1 Pattern fracturing . . . . .	23
2.4.2 Dose determination . . . . .	25
2.4.3 Sample preparation . . . . .	27
2.4.4 Exposure . . . . .	28
2.5 ICP etching . . . . .	28
2.6 Membrane suspension . . . . .	31
2.6.1 AZ5214 coating . . . . .	32
2.6.2 Cleaving and facets protection . . . . .	33
2.6.3 Membrane release . . . . .	35
2.7 Anti-reflection coating . . . . .	35

## Contents

---

2.8	SU8 mode adaptors . . . . .	37
2.9	Microfluidic layers . . . . .	39
2.10	PDMS mold . . . . .	42
2.11	PDMS membrane . . . . .	43
2.12	Glass layer . . . . .	44
2.13	Microfluidic layers assembly . . . . .	45
<b>3</b>	<b>Experimental setup and characterisation</b>	<b>47</b>
3.1	Preexisting setup . . . . .	47
3.1.1	Optical setup . . . . .	47
3.1.2	Microfluidics control . . . . .	51
3.2	Modified setup . . . . .	52
3.2.1	Optical setup . . . . .	52
3.2.2	Manipulation and storage of bacteria . . . . .	55
3.3	Experimental setup in CEA Grenoble . . . . .	56
3.4	Experimental procedure . . . . .	57
3.5	Device characterisation . . . . .	58
3.5.1	Optical characterisation . . . . .	58
<b>4</b>	<b>Self-Induced Back-Action and “cage” trapping</b>	<b>67</b>
4.1	Resonant optical trapping in hollow 2D PhC cavity . . . . .	67
4.1.1	Experimental procedure . . . . .	68
4.1.2	Brownian motion . . . . .	70
4.1.3	Trapping capabilities . . . . .	70
4.2	Particle-dependent resonance frequency shift . . . . .	71
4.3	“Classical” and “cage” trapping regimes . . . . .	72
4.4	Particle differentiation: the case of 250 and 500 nm nanospheres . . . . .	76
4.5	Conclusions . . . . .	81
<b>5</b>	<b>Bacterial Gram-type differentiation</b>	<b>83</b>
5.1	Bacterial properties . . . . .	84
5.1.1	Morphology . . . . .	84
5.1.2	Motility . . . . .	84
5.1.3	Cellular membrane . . . . .	85
5.2	Bacteria studied . . . . .	87
5.3	Trapping capabilities . . . . .	88
5.3.1	Bacterial preparation . . . . .	88
5.3.2	Experimental procedure . . . . .	91
5.3.3	Minimum trapping power . . . . .	92
5.4	Bacterial Gram-type distinction . . . . .	95
5.4.1	Gram-type differentiation . . . . .	96
5.4.2	Bacteria identification . . . . .	98
5.5	Conclusions . . . . .	100

<b>6 Conclusions and perspectives</b>	<b>101</b>
<b>Bibliography</b>	<b>116</b>
<b>Acknowledgements</b>	<b>117</b>
<b>Curriculum Vitae</b>	<b>119</b>





# List of Figures

1.1 Photonic crystals in nature . . . . .	3
1.2 Lattice-dependent colour . . . . .	3
1.3 Band diagram and PBG . . . . .	5
1.4 Band structure of a 2D PhC membrane with defects . . . . .	6
1.5 Q factor definition . . . . .	7
1.6 2D hollow photonic crystal cavity . . . . .	9
1.7 Classical tweezers . . . . .	10
1.8 Ray-optics approximation . . . . .	14
1.9 Backaction . . . . .	16
1.10 SIBA effect in “cage regime” . . . . .	17
1.11 Optofluidic chip . . . . .	18
2.1 Fabrication process overview . . . . .	20
2.2 Schematic representation of a photolithography process. . . . .	21
2.3 Direct writing vs mask . . . . .	21
2.4 Cr mask fabrication . . . . .	22
2.5 EBL system . . . . .	23
2.6 Fracturing resolution . . . . .	24
2.7 Curved vs sequence fracturing . . . . .	24
2.8 Stitching errors . . . . .	25
2.9 Floating fields . . . . .	25
2.10 Proximity effects . . . . .	26
2.11 Ebeam sample holder . . . . .	27
2.12 Beam choice . . . . .	28
2.13 ICP etcher . . . . .	29
2.14 Etchest . . . . .	30
2.15 Sample preparation . . . . .	32
2.16 AZ5214 residues . . . . .	33
2.17 Sample cleaving . . . . .	34
2.18 Facets protection . . . . .	34
2.19 Fabry-Perot interferences . . . . .	35
2.20 Magnetron sputtering . . . . .	36
2.21 Absolute reflection spectra for AR coating. . . . .	37

## List of Figures

---

2.22	Waveguide tapers and SU8 mode adaptors . . . . .	38
2.23	Schematic representation of the SU8 spin steps. . . . .	38
2.24	SU8 mode adaptors . . . . .	39
2.25	Optofluidic chip . . . . .	39
2.26	Microfluidic layers . . . . .	40
2.27	The three microfluidic configurations used . . . . .	41
2.28	Quake valve . . . . .	41
2.29	Two injection channels . . . . .	42
2.30	PDMS mold . . . . .	43
2.31	Channel profile before and after reflow . . . . .	43
2.32	Glass channels layout. . . . .	44
2.33	Glass channels before and after polishing. . . . .	45
3.1	Preexisting optical setup. . . . .	48
3.2	End-fire arrangement. . . . .	48
3.3	Setup for simultaneous trapping and $\lambda$ scanning. . . . .	50
3.4	Microfluidic connections. . . . .	51
3.5	Microfluidics control . . . . .	52
3.6	Fluorescent particles and LED spectra. . . . .	53
3.7	Modified optical setup. . . . .	53
3.8	Sample holder. . . . .	54
3.9	Peltier module. . . . .	55
3.10	Bacteria working station. . . . .	56
3.11	Experimental setup in CEA Grenoble. . . . .	56
3.12	Setup for sample characterisation. . . . .	57
3.13	Setup for optical trapping experiments. . . . .	58
3.14	Hollow optical cavities. . . . .	59
3.15	Lorentzian fit. . . . .	61
3.16	Water induced resonant wavelength shift. . . . .	62
3.17	Silicon surface properties. . . . .	63
3.18	Temperature dependence of the resonance wavelength. . . . .	63
3.19	Anti-reflection coating . . . . .	64
3.20	SU8 mode adaptors . . . . .	64
4.1	Experimental setup. . . . .	69
4.2	Fluorescent particle trapping. . . . .	69
4.3	Resonant trapping. . . . .	71
4.4	FEM simulations of induced shift. . . . .	72
4.5	Classical regime. . . . .	73
4.6	Cage regime. . . . .	74
4.7	Existence of the cage regime. . . . .	74
4.8	Cutoff frequencies. . . . .	75
4.9	Particle-dependent transmission increment. . . . .	76

4.10	Transmission for 250 and 500 nm polystyrene nanospheres. . . . .	77
4.11	Qualitative analysis of the trapping of a 500 nm nanosphere. . . . .	78
4.12	Histograms for the entire set of measurements. . . . .	79
4.13	Average histograms. . . . .	80
4.14	Variance and skewness. . . . .	80
5.1	Bacterial morphology. . . . .	84
5.2	Bacterial motility. . . . .	85
5.3	Gram positive and Gram negative mcellular membrane. . . . .	86
5.4	Gram staining technique. . . . .	86
5.5	SEM images of the bacteria studied. . . . .	87
5.6	<i>Escherichia coli</i> culture on a CBA Petri dish. . . . .	89
5.7	Bacterial growth curve. . . . .	89
5.8	Experiemntal setup for bacteria . . . . .	91
5.9	Bacteria identification in 1D PhC . . . . .	92
5.10	Transmission curve for the trapping of <i>Y. ruckeri</i> . . . . .	93
5.11	Injected power dependence for the trapping of <i>Y. ruckeri</i> . . . . .	93
5.12	Histograms for different injected powers . . . . .	94
5.13	Bacteria-dependent resonance frequency shift . . . . .	96
5.14	Mean transmission increase . . . . .	97
5.15	Cavity field and cell wall . . . . .	97
5.16	Mean bacteria histograms . . . . .	98
5.17	Distances between transmission curves . . . . .	99
5.18	Standard deviations . . . . .	100



## Table of Symbols and Acronyms

Symbol/Acronym	Correspondence
BHF	Buffered HydroFluoric acid
BSA	Bovine Serum Albumine
CAD	Computer-Aided Drafting
CBA	Columbia Blood Agar
COC	Cyclic Olefin Copolymer
DI water	Deionized water
DNQ-sulphonates	Diazonaphthoquinone-sulphonates
EBL	Electron Beam Litography
EMCCD	Electron Multiplying Charge-Coupled Device
HDMS	Hexamethyldisilazane
ICP	Inductively Coupled Plasma
IPA	Isopropanol
NA	Numerical Aperture
PBG	Photonic Band Gap
PDMS	Polydimethylsiloxane
PGMEA	Propylene Glycol Monomethyl Ether Acetate
PhC	Photonic Crystal
PS	Polystyrene
PSD	Power Spectrum Density
Q factor	Quality factor
QS135	Quickstick 135
sccm	Standard Cubic Centimeters per Minute
SEM	Scanning Electron Microscope
SIBA	Self-Induced Back-Action
SOI	Silicon-On-Insulator
TBS	Thermal Bonding System
TE / TM	Transverse Electric / Transverse Magnetic
TEC	Thermo-Electric Cooler
TMCS	Trimethylchlorosilane
TSA	Tryptic Soy Agar
WEC	Wedge Error Compensation
WFG	Wave Form Generator
WH	Writing Head



# 1 Introduction

During the last decade, the miniaturisation of laboratory tools and their implementation in lab-on-a-chip platforms have proven to be crucial fields of research. The simplification and size-reduction of scientific apparatuses is of great interest for a number of applications where it is desirable to obtain fast and accurate results with portable instruments, such as diagnostics, environmental analysis, food and water quality control, etc.

At the same time, optical tweezers consisting in a tightly focused laser beam have found an increasing range of application, going from sensing to particle manipulation, force measurements and optical cooling. However, in their classical configuration they require bulky instrumentation, at least of the size of a microscope. A miniaturisation of such kind of optical tools is possible with the use of nanostructures, thanks to their small footprint combined with their ability to strongly confine light and hence provide the necessary field gradients.

This thesis reports on the use of a 2D hollow photonic crystal cavity, integrated with microfluidic layers, for optical trapping applications. The hollow nature of the cavity results in a large overlap between the confined field and the trapped objects, while the resonant nature of the trapping mechanism gives rise to Self-Induced Back-Action (SIBA) effects and to two different trapping regimes that allow to trap particles and biological entities with ultralow powers (of the order of few hundreds of microwatts). In particular, a peculiar regime that we referred to as “cage regime” was used to trap and distinguish polystyrene nanospheres with different sizes and living bacteria with different cell wall properties.

In this chapter, the basic concepts and the state of the art are presented. Photonic crystals (PhC) and the light confinement in these structures are first introduced, together with a description of our cavity. Secondly, an overview on optical forces and on their applications is given. Their derivation in the dipole and in the ray-optics limits is also presented. Finally, a state of the art of nanostructure-based optical tweezers systems is provided, with particular attention on optofluidic systems.

The second chapter reports on the fabrication of the optofluidic chip. The entire fabrication of

## Chapter 1. Introduction

---

the chip and its integration with microfluidic layers is performed at EPFL cleanrooms and in this chapter the process is detailed.

In the third chapter, the experimental setups are presented. Experiments were performed here at EPFL and in CEA Grenoble laboratories, in the framework of a collaboration with the groups of Emmanuel Hadji, David Peyrade and Pierre Marcoux: the optical setups are very similar but some differences are highlighted. In this chapter, the sample characterisation is also reported.

The fourth chapter permits to introduce the experimental procedure and the the two trapping regimes supported by our cavity. The exploitation of the SIBA effects to distinguish objects with different sizes, refractive indexes and shapes is also shown and it is exemplified by the distinction of 250 and 500 nm polystyrene nanoparticles.

Finally, the fifth chapter contains the results on optical trapping and on Gram-type determination of seven species of living bacteria with a simple transission measurement. With this result we show that we can probe the cell wall of bacteria, and this could be of great interest for applications in antibiotic susceptibility determination, as it will be shown in the conclusions.



## 1.1 Photonic crystals

Photonic Crystals (PhC) are materials in which the dielectric constant is periodic in one, two or three dimensions. This periodic arrangement, under well chosen conditions, can generate a Photonic Band Gap (PBG), i.e. a frequency window within which the propagation of light through the crystal is prohibited. In order to permit the interaction between photons and the periodic medium through interference effects, the periodicity of the lattice has to be comparable with the wavelength: this results in a lattice constant of the order of few hundreds of nanometers for visible and near-IR light.

Photonic crystals are present in nature and are responsible for the structural colours of butterflies wings [1, 2], peacock feathers [3], and opals [4], but also of beetles [5] and chameleons [6] (Fig. 1.1 and 1.2). As a matter of fact, these colours arise from the presence of a PBG and, differently from pigment-based colours, they depend on the angle of illumination, in a phenomenon known as iridescence.

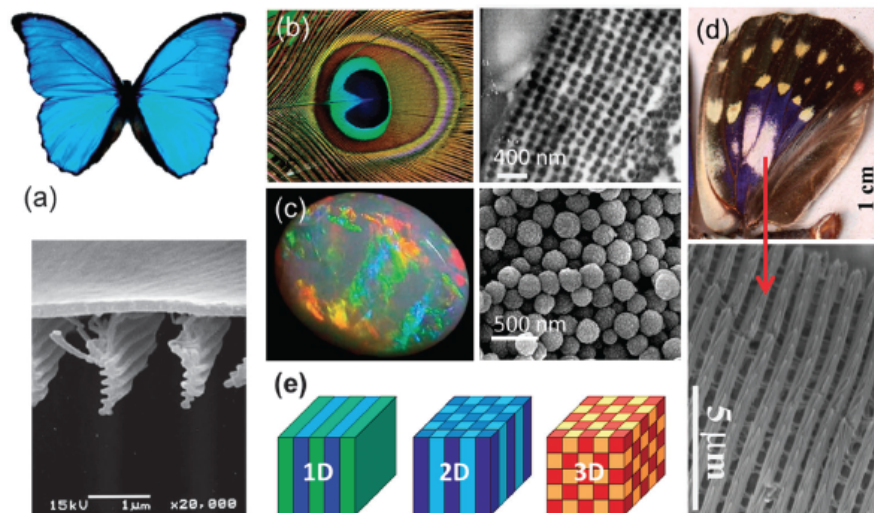


**Figure 1.1** – Examples of photonic crystals in nature. Figure from [7].

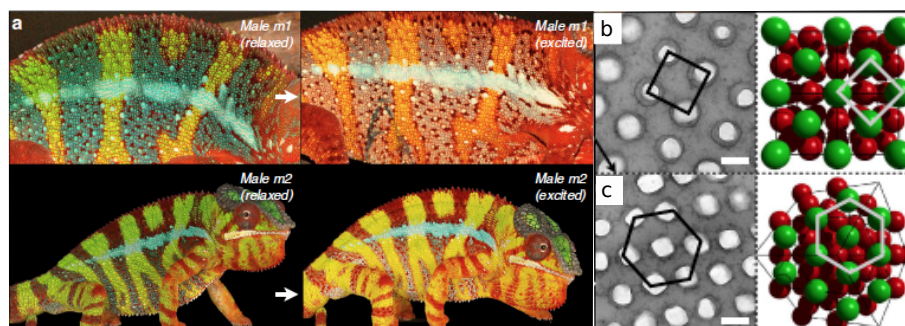


**Figure 1.2** – Chameleons change their colour thanks to their ability to modify the arrangement of guanine nanocrystals. (a) Pictures of two chameleons in their relaxed and excited state). (b) Lattice structure in the relaxed state. (c) Lattice structure in the excited state. Figure adapted from Ref. [6].

The propagation of light in such periodic structures can be described by a band diagram, that shows the frequencies for which propagation in the crystal is possible and those for which it is inhibited. Naturally this band structure (and hence the PBG) not only depends on the dielectric constant of the two media, but also on their spatial periodicity. For the structures mentioned beforehand the iridescence is a direct cause of the different lattice parameters with respect to different incidence angles. As an other example of the lattice effects in the photonic bandgap, the case of chameleons can be considered: their ability to rapidly and reversibly change colours is provided by the modification of the periodic arrangement of guanine nanocrystals [6], as shown in Fig. 1.2, that pass from a square configuration when the chameleons are relaxed to a triangular lattice when the animals are excited.

However, the description of these phenomena in terms of photonic crystals is quite recent. One-dimensional structures consisting in a stack of dielectric materials are known since the end of 19th century, but the official birth of the general concept of PhC dates 1987, with the works of Eli Yablonovitch [8] (a full 3D photonic band gap can be used to suppress spontaneous emission) and of Sajeev John [9] (disorder close to the edge of a PBG can be used to produce strong Anderson localization of light). First structures presenting photonic band gaps were proposed and fabricated at the beginning of the 1990s [10, 11, 12, 13]. As the spatial constant has to be of the same order of the wavelength, the photonic crystal development was strongly linked to the concurrent state of the fabrication technology and the earlier structures ([12, 13]) were operating in the microwave range.

Since then, photonic crystals became a large field of research and they found a huge range of applications in all the fields where it is desirable to confine or manipulate light. For instance, light-matter interactions were studied [14], integrated optoelectronics circuits were developed (like modulators [15] or optical switches [16]) and biological systems were investigated [17, 18, 19].

### 1.1.1 Band structure and photonic band gap

To illustrate the formation of the band structure and of the photonic bandgap, for simplicity the case of a 1D photonic crystal structure will be considered, consisting in a stack of materials with alternating dielectric constant. The properties of an harmonic wave propagating in a dielectric medium can be obtained by solving the Maxwell's equations and the following master equation is obtained (for its derivation, see for instance [20] or [21]):

$$\left( \vec{\nabla} \times \frac{1}{\epsilon(\vec{r})} \vec{\nabla} \right) \times \vec{H}_\omega(\vec{r}) = \left( \frac{\omega}{c} \right)^2 \vec{H}_\omega(\vec{r}) \quad (1.1)$$

which is an eigenvalue problem.

For periodic media, the Bloch-Floquet theorem holds and solutions of 1.1 have to be of the form

$$\vec{H}(\vec{r}, t) = e^{i(\vec{k}\vec{r} - \omega t)} \vec{H}_k(\vec{r}) \quad (1.2)$$

For each of these Bloch modes there is a unique relation between  $\omega$  and the wavevector  $\vec{k}$ , called dispersion, and the set of all the Bloch modes supported by a periodic medium forms the band structure. An important consequence of Eq. 1.2 is the fact that the wavevector is also periodic:  $\vec{k} = \vec{k} + \frac{2\pi}{a}$ , where  $a$  is the periodicity of the perturbation in dielectric constant. It is thus possible to fold the diagram by a period equivalent to  $\frac{2\pi}{a}$  and to completely describe the propagation properties in the first Brillouin zone, extending from  $k = -\frac{\pi}{a}$  to  $k = \frac{\pi}{a}$ , as shown in Fig. 1.3. For every frequency  $\omega$ , a forward and a backward propagating modes are present, identified by positive and negative wavevectors respectively.

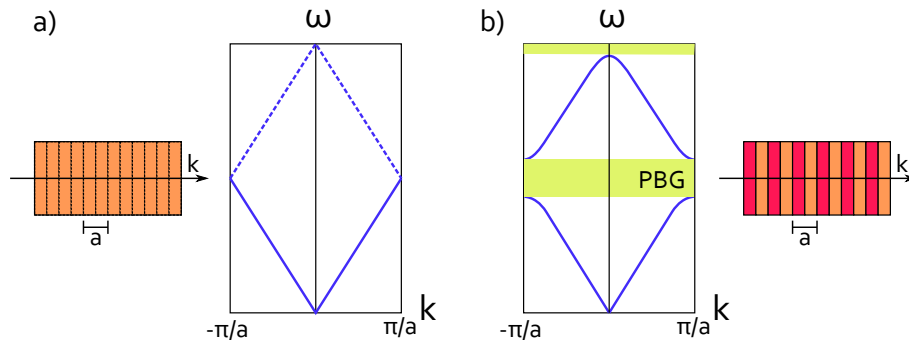


**Figure 1.3** – (a) Band diagram for a uniform medium. An artificial periodicity can be introduced and the band diagram can be folded at the limits of the Brillouin zone, that extends from  $k = -\frac{\pi}{a}$  to  $k = \frac{\pi}{a}$ . Positive wavevectors correspond to forward-propagating modes while negatives  $k$  correspond to backwards-propagating modes. (b) Band diagram for a periodic medium. Reflections at the interfaces between media cause interference and coupling between forward and backward-propagating modes, that hybridize. A window of frequencies for which no  $k$  are available, called photonic bandgap, is created.

In the case of a single dielectric medium, the same description can be carried out by introducing an artificial periodicity. As it is shown in Fig. 1.3 (a), the band structure simply folds and all the frequencies can propagate in the medium. In the case of periodic media with two dielectric constants, on the contrary, reflections occur at the interfaces. Those reflections result in a coupling between the forward and the backward-propagating modes and cause an anticrossing of the modes at the edges of the Brillouin zone. A photonic band gap is thus created: for some frequencies, no wavevector is available and the propagation through the PhC is not possible. The width of this forbidden frequency range grows for increasing refractive index contrast between the two media.

The same principle can be applied to two- and three-dimensional photonic crystals, but the

complexity of the systems requires numerical computations to obtain the eigenmodes. An example of band structure for a 2D photonic crystal is showed in Fig. 1.4, where the PhC is created by a triangular lattice of air holes in a silicon slab. In analogy to the solid state physics treatment, the band structure is projected on the symmetry directions of the first Brillouin zone, which in this case is a hexagon.

Bloch modes with frequencies lower than the bandgap form the dielectric band and are mainly confined in the medium with larger  $\epsilon$ , while the eigenmodes with larger frequencies form the air band and are mainly confined in the lower refractive index medium. Moreover, the larger the dielectric constant contrast between the two materials, the most the modes are confined into their corresponding medium. This leads to important consequences for the exploitation of the fields, as it will be shown in the following.

### 1.1.2 Defects in 2D photonic crystals

One major interest in the use of photonic bandgap materials is the possibility to strongly confine light and to create cavities and waveguides. This is achieved by introducing defects in the lattice structure, that result in the perturbation of the periodicity and hence in a “pulling” of some modes inside the PBG. Two main classes of defects can be introduced: point-like (that

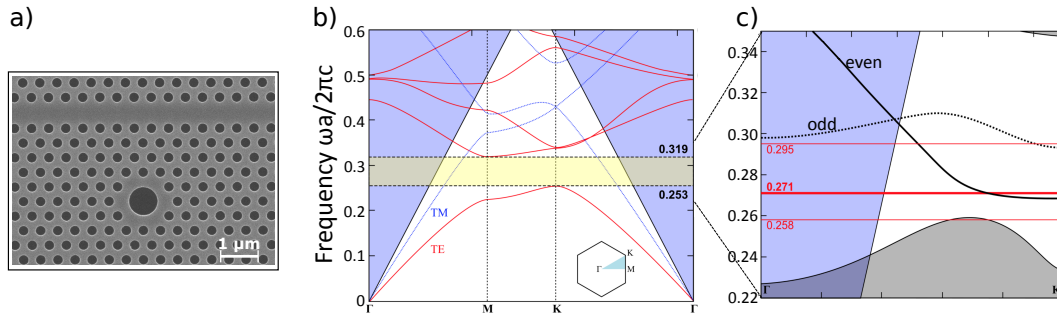


**Figure 1.4** – (a) SEM micrograph of the system considered. It is a 2D photonic crystal silicon membrane. The periodicity is interrupted by a W1 waveguide and by a H0 cavity. (b) The band structure calculated for a perfectly periodic lattice for TE polarisation. A bandgap is shown. (c) Detail of the bandgap while considering the modes supported by W1 waveguide (in black) and by the cavity (in red).

create a cavity) and line-like (creating a waveguide). A point-like defect can be created in a variety of ways, for instance by removing or changing the size of one or few lattice holes. A waveguide, on the other hand, is generally created by removing one or several lines of holes and it is referred to as W1, W2, .. Wn depending on the number of lines removed.

To illustrate this, the band structure of the system used in this thesis (that will be detailed in section 1.1.4) is shown. It consists in a 2D photonic crystal formed by a triangular lattice of holes in a silicon membrane. Moreover, two defects are introduced: a W1 waveguide and a HO cavity obtained by enlarging one of the holes (Fig. 1.4 (a)). This structure has a complete band gap for TE (Transverse Electric) polarisation (Fig. 1.4 (b)). On the figure, the light line is also showed, *i.e.* the line given by the relation  $\omega = \frac{c}{n}k$  that separates the continuum of

radiating modes (above) from the modes that are allowed to propagate in the slab. In Fig. 1.4 (c) the modes introduced in the PBG by the presence of a W1 and of the cavity are depicted in black and red respectively. In general, a waveguide permits the propagation for a range of frequencies, while a cavity creates a discrete state inside the bandgap, thus strongly confining light for a certain frequency (in our case, 0.27 of reduced frequency).

### 1.1.3 Q factor and modal volume

The two most important figures of merit of a resonant cavity are the quality factor  $Q$  and the modal volume  $V$ , together with their  $Q/V$  ratio.

#### Quality factor

The quality factor is a dimensionless number that is used to measure the losses of a resonant cavity. Light is confined in a 2D photonic crystal cavity by two mechanisms: by the PBG confinement in the plane of the photonic crystal and by total internal reflection in the out-of-plane direction, due to the contrast index between the silicon and the surrounding medium. The electromagnetic field is confined for a finite time in the cavity and in its formal definition the  $Q$  factor is the ratio of the energy stored in the system with respect to the losses per cycle at the resonance frequency  $\omega_0$ :

$$Q = \frac{\omega_0 E_{\text{stored}}}{P_{\text{dissipated}}} \quad (1.3)$$

The field decays exponentially and when plotting the mode energy with respect to the frequency a Lorentzian-type of curve is obtained (Fig. 1.5) and the quality factor is simply given by

$$Q = \frac{\nu_0}{\Delta\nu} \quad (1.4)$$

where  $\Delta\nu$  is the full width of half maximum of the curve shown in Fig. 1.5.

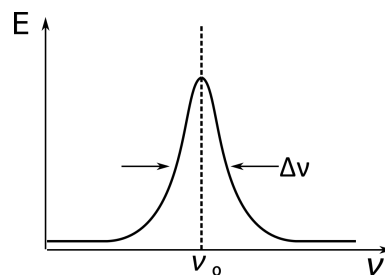


**Figure 1.5** – Energy of the localised mode as a function of frequency. The  $Q$  factor can be defined as  $Q = \nu_0/\Delta\nu$ .

## Chapter 1. Introduction

---

The Q factor experimentally measured is usually expressed as a sum of several factors to take into account the different decay mechanisms that occur:

$$\frac{1}{Q_{measured}} = \frac{1}{Q_{intrinsic}} + \frac{1}{Q_{coupling}} + \frac{1}{Q_{extrinsic}} \quad (1.5)$$

The first term,  $Q_{intrinsic}$ , takes into account the geometrical properties of the cavity. This factor is linked to the field distribution and to its coupling with the continuum of radiative modes above the light line [22, 23]. The second term,  $Q_{coupling}$ , takes into account the coupling mechanism to excite the resonance. For cavity excited by evanescent coupling, the distance from the exciting mode is of crucial importance. Finally, the  $Q_{extrinsic}$  factor considers both the losses due to material absorption and the ones due to scattering from impurities and imperfections, such as surface roughness or lattice disorder.

### Modal volume

The modal volume gives a measure of the spatial extent of the confined mode and in its most common definition it is given by [24]:

$$V = \frac{\iiint \epsilon(\mathbf{r}) |\mathbf{E}(\mathbf{r})|^2 d^3\mathbf{r}}{\max[\epsilon(\mathbf{r}) |\mathbf{E}(\mathbf{r})|^2]}. \quad (1.6)$$

It is usually expressed in  $\left(\frac{\lambda}{n}\right)^3$  units and to smaller modal volumes correspond stronger field confinements.

#### 1.1.4 2D hollow photonic crystal cavity

In this section the cavity used during the thesis is presented. It consists in a hollow cavity, evanescently coupled to a W1 waveguide in a silicon 2D photonic crystal membrane (Fig. 1.6). Light injection and collection are carried out in an end-fire setup.

The bulk material is a 220 nm thick silicon membrane and the photonic crystal structure is created by a triangular lattice of holes, 250 nm in diameter and with a lattice constant of 420 nm. An optical cavity is created by enlarging one of the lattice holes to a diameter of 700 nm. Finally, a W1 waveguide allows for light propagation and for evanescent excitation of the cavity mode.

Evanescent excitation of cavity modes with a W1 waveguide was first shown by Noda in 2000 [26], while the proposal to use this hollow cavity design for particle detection was introduced by Lee and Fauchet in 2007 [27]. According to the definition 1.6, this cavity presents a modal volume of  $2.3(\lambda/n)^3$  and typical quality factors are of the order of 8000-10000 in air and of 3000-5000 in water, as it will be discussed in Chapter 3. This combination of small  $V$  and high field confinement creates strong field gradients, that are fundamental for optical trapping.

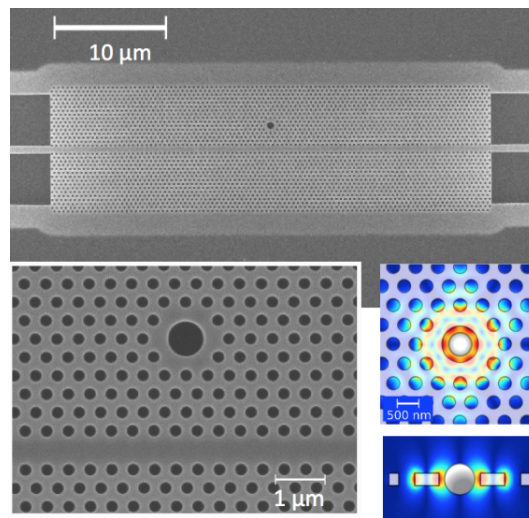


**Figure 1.6** – SEM micrograph of our 2D hollow photonic crystal cavity and finite element calculation of the confined field. Calculation from Ref. [25].

It has to be mentioned that cavities presenting larger quality factors [28, 29, 30] or smaller modal volumes have been presented [23, 31, 32]. Nevertheless, the main interest of this cavity design resides in the large overlap between the confined mode and the hollow volume, leading to a maximum interaction with the objects to be trapped and analysed. Indeed, more than 30% of the confined electric field overlaps with the low index medium and more than 10% of the total is located inside the cylindrical volume of the hole.

Moreover, large quality factors are not necessarily the best choice for trapping applications, as it will be discussed in Chapter 4 where the “cage trapping” mechanism will be discussed. Finally, the size of this cavity makes it particularly adapted for trapping particles that measure few hundreds of nanometers, but the trapping of larger objects such as bacteria was successful as well. For these reasons, this hollow cavity design is a very promising tool for sensing and biological analysis.

## 1.2 Optical trapping

### 1.2.1 Optical forces

The fact that light can exert mechanical forces is an idea with a long story: as early as 1609, Johannes Kepler suggested that light might cause the deflection of the tails of the comets and the classical Maxwell theory (1873) showed that the electromagnetic field carries momentum and that a radiation pressure is exerted on illuminated objects. In 1905 Einstein introduced the concept of “photon” and showed that energy transfer between light and matter happens in discrete quanta. The discrete momentum transfer between X-rays and electrons was demonstrated 20 years later by Compton, while in 1933 the recoil momentum transferred from photons to atoms was observed by Frisch [33].



Starting from 1970, the group of Ashkin at Bell Laboratories showed acceleration and trapping of micron-sized particles with a cw visible laser [34]. These experiments led to the development of optical tweezers in the late Eighties [35, 36], for which Ashkin was awarded the Nobel Prize in Physics in 2018. In their classical form, optical tweezers consist in a tightly focused beam that can confine microscopic particles stably in three dimensions (Fig. 1.7). Typical sizes of trapped objects are on the order of  $0.1\text{-}10\ \mu\text{m}$  and the forces produced are of the order of piconewtons, for milliwatts of laser power [37]. As it will be discussed in the next section, a particle near the focus experiences a force that can be decomposed into two components: a scattering force, directed in the direction of propagation of the beam, and a gradient force, directed towards the higher beam intensity. When the gradient forces dominate, the particle can be trapped near the focal point [38, 39, 40]. In classical cases, the trapped object is subject to an harmonic potential. One can thus define a trap stiffness as the slope of this linear approximation: it depends on the field gradients, the particle polarizability and the laser power.

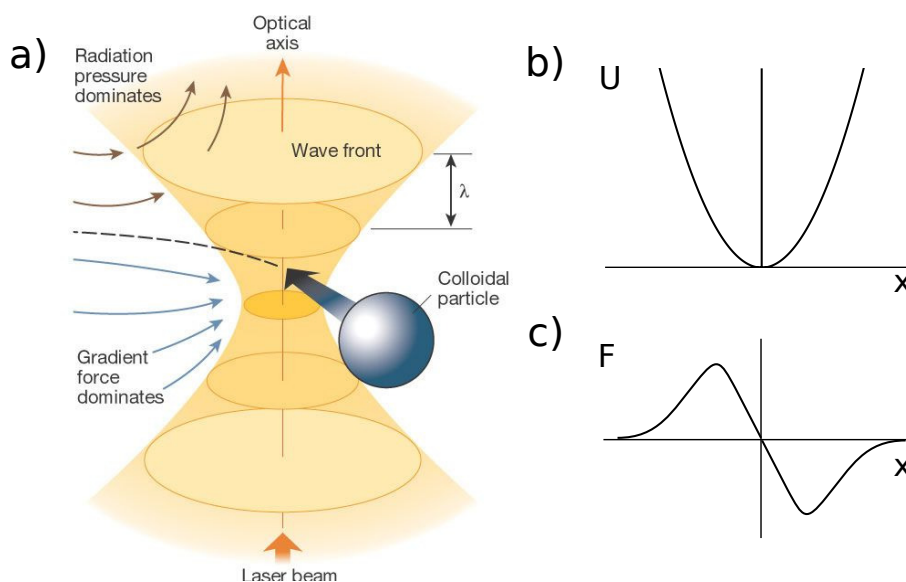


**Figure 1.7** – (a) Representation of classical optical tweezers. Figure from Ref. [41]. (b) The potential experienced by the trapped object is harmonic and (c) the force is linear for small displacements from the equilibrium position.

Optical tweezers have found a large variety of application, especially in the biological field [42]: for instance, they were used to stretch DNA [43], to detect single proteins [44], to characterise the surface of bacterial spores [45], to manipulate organelles in cells [46] and even to manipulate cells inside living zebrafishes [47]. Applications to inorganic materials are also shown [48] such as the trapping of metallic particles [49], carbon nanotubes [50, 51], quantum dots [52] and plasmonic nanoparticles [53] to give few examples.

Besides sensing and manipulation of objects, optical trapping has also applications in force measurement, in the pN range [39, 48] and down to 10 aN for the gravitational force [54].



Finally, another large and exciting field of applications of optical forces is optical cooling, where the scattering forces (that are linked to the momentum transfer between the impinging photons and the particles) are predominant. In 1975, Hänsch and Schawlow showed that a gas could be cooled by laser radiation [55]. This was the starting point for the works that led to the 1997 Nobel Prize in physics, awarded to Steven Chu, Claude Cohen-Tannoudji and William Daniel Phillips. Since then, many experiments have been carried out, cooling microparticles [56] and nanoparticles [57] to subkelvin temperatures and opening the routes for testing quantum mechanics with mesoscopic objects.

### 1.2.2 Dipole and ray-optics approximations

The calculation of optical forces on an arbitrary object requires solving Maxwell's equations. The forces exerted on an object can be fully determined by the Maxwell's stress tensor formalism [58] but often an analytical solution is not possible and numerical methods have to be invoked. However, in limiting cases such as very small or very big particles (with respect to the incident wavelength), simple analytical expressions for gradient and scattering forces can be retrieved.

#### The dipole approximation

Particles much smaller than the wavelength of the illumination beam can be considered as point-like electric dipoles and it is possible to derive an analytical expression for the optical forces acting on them. This approach is particularly adapted for atoms or molecules [59], while for bigger particles (but still smaller than the wavelength) the coupled-dipole approach can be used. This consists in modelling an arbitrary-shaped object as a sum of individual dipoles, that are treated separately. This method was first introduced by Purcell and Pennypacker [60] and it was also used, for instance, to estimate the forces acting on small particles such as stellar dust grains [61] or colloids [62].

Let us consider a single dipole composed by two particles of charges  $q$  and  $-q$  immersed in an external electromagnetic field. We use the force law

$$\vec{F}(\vec{r}, t) = q[\vec{E}(\vec{r}, t) + \vec{v}(\vec{r}, t) \times \vec{B}(\vec{r}, t)] \quad (1.7)$$

and the definition of the dipole moment

$$\vec{p} = q\vec{s} \quad (1.8)$$

where  $\vec{s}$  is the distance between the two particles.

A straightforward calculation, that can be found for instance in Ref. [63], leads to the following relation for the force acting on the dipole

$$\vec{F} = (\vec{p} \cdot \vec{\nabla})\vec{E} + \frac{\partial \vec{p}}{\partial t} \times \vec{B} + \frac{\partial \vec{p}}{\partial t} \times (\vec{p} \cdot \vec{\nabla})\vec{B} \quad (1.9)$$

## Chapter 1. Introduction

---

where the dependence from  $(\vec{r}, t)$  was omitted for clarity.

The force is the sum of three terms: the first one originates from the spatial inhomogeneities of the electric field, the second is the Lorentz force and the third one is due to the inhomogeneous magnetic field. For non-relativistic speeds this term is much smaller than the others and it is usually neglected.

If we consider a time-averaged force, the second term also drops and the force can be written in the compact form

$$\langle \vec{F} \rangle = \sum_i \langle p_i(t) \nabla E_i(t) \rangle \quad (1.10)$$

Considering a monochromatic field, a linear relation between the fields and the dipole and the absence of static dipole moment we can write

$$\vec{E}(\vec{r}, t) = \text{Re}\{\vec{E}_0 e^{-i\omega t}\}$$

$$\vec{B}(\vec{r}, t) = \text{Re}\{\vec{B}_0 e^{-i\omega t}\}$$

$$\vec{p}(\vec{r}, t) = \text{Re}\{\vec{p}_0 e^{-i\omega t}\}$$

and

$$\vec{p}_0 = \alpha \vec{E}_0$$

where  $\alpha$  is the polarizability of the particle.

Finally, eq. 1.10 can be expressed as

$$\langle \vec{F} \rangle = \frac{\alpha'}{2} \sum_i \text{Re}\{E_{0i}^* \nabla E_{0i}\} + \frac{\alpha''}{2} \sum_i \text{Im}\{E_{0i}^* \nabla E_{0i}\} \quad (1.11)$$

where  $\alpha = \alpha' + i\alpha''$ . The first term can be rewritten as a gradient,  $(\alpha'/4)\nabla(\vec{E}_0^* \cdot \vec{E}_0)$ , and it is referred to as the gradient force. It is proportional to the field gradient and to the real part of the particle polarizability and it accelerates particles towards the maximum of the radiation field, allowing for their optical trapping. The second one, on the contrary, cannot be expressed as a gradient of a potential and it is thus a non-conservative component. It is proportional to the dissipative part of the polarizability and it is usually called scattering force.

This expression was obtained considering the propagating beam and the particle to be trapped in vacuum. However, most often optical tweezers act in aqueous media, and hence the dielectric constant of the “background medium”,  $\epsilon_b$ , needs to be included in the expression [64]:

$$\langle \vec{F} \rangle = \epsilon_b \frac{\alpha'}{2} \sum_i \text{Re}\{E_{0i}^* \nabla E_{0i}\} + \epsilon_b \frac{\alpha''}{2} \sum_i \text{Im}\{E_{0i}^* \nabla E_{0i}\} \quad (1.12)$$

Finally, considering the corrections due to radiation reaction ([63]), the imaginary part of the polarizability can be written as

$$\alpha'' = \frac{k^3}{6\pi\epsilon_0} \alpha'^2 \quad (1.13)$$

where  $k$  is the wavevector.

Introducing also the Clausius-Mossotti relation for the polarizability, this leads to the following explicit expression for the time-averaged forces acting on a sphere in the dipole approximation:

$$\langle \vec{F} \rangle = \epsilon_0 \epsilon_b \pi a^3 \left( \frac{\rho^2 - 1}{\rho^2 + 2} \right) \nabla E_0^2 + \frac{4}{3} \epsilon_0 \epsilon_b \pi k^4 a^6 \left( \frac{\rho^2 - 1}{\rho^2 + 2} \right)^2 E_0^2 \quad (1.14)$$

where  $a$  is the particle radius and  $\rho$  is the refractive index contrast between the particle and the medium,  $\rho = n_{particle}/n_{background}$ .

In this expression some constraints for optical trapping can be observed: first, a strong dependence on the particle size is shown. As the gradient force scales with the third power of the radius, smaller particles are more difficult to trap. Moreover, this difficulty is increased by the fact that at the same time their Brownian motion is increased, according to the diffusion expression:

$$D = \frac{k_B T}{6\pi r \eta} \quad (1.15)$$

where  $\eta$  is the viscosity of the liquid [65].

Secondly, optical forces are more intense for particles with a larger index contrast with respect to the surrounding medium. In this sense, the trapping of biological objects is more challenging than the trapping of metallic or dielectric nanoparticles, as their refractive index is very close to the one of water where they are usually immersed.

These mechanisms result in the need of larger laser powers to optically trap small objects (on the order of few hundreds of nanometers) or biological entities. The necessary powers can easily be of the order of hundreds of milliwatts, above the damage threshold of trapped specimen [66].

### The ray-optics approximation

For particles much larger than the incident wavelength, on the other hand, optical trapping can be explained by a ray-optics analysis, as shown in Fig. 1.8. In this model, a single ray impinging on the particle is refracted twice and its momentum change  $\Delta \vec{p}$  is calculated by considering the vectorial difference of the incoming and outgoing rays. For momentum

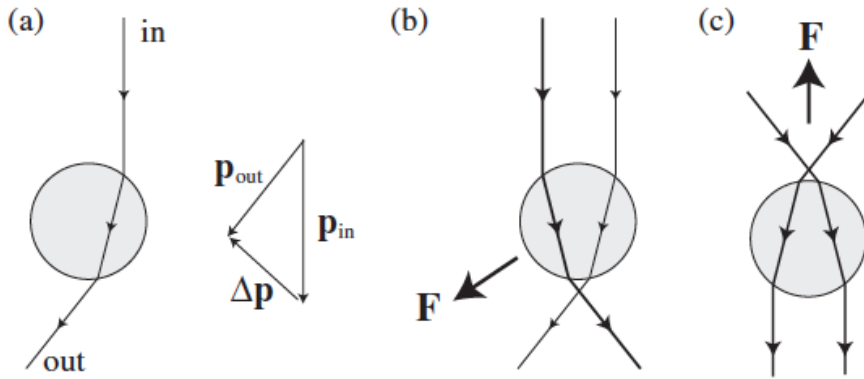


**Figure 1.8** – Illustration of the optical forces induced on a dielectric particle in the ray-optics approximation. (a) A momentum  $-\Delta\vec{p}$  is transferred to the particle. (b) In case of inhomogeneous field distribution, a force pulling the particle towards the higher intensity appears. (c) In a symmetric beam, a particle placed over the focal point is pulled back to the focus. Figure from Ref. [63].

conservation, the momentum transferred to the particle is  $-\Delta\vec{p}$ . In a uniform field, all the components but the ones directed in the forward direction cancel and the particle is pulled in the direction of propagation of the beam [67]. However, if the field intensity is not uniform, such as near to the focus of a laser, a force directed towards the higher intensity is generated, as shown in Fig. 1.8 (b). Stable trapping is achieved for systems where the sum of the forces is zero and any displacement results in a restoring force towards the equilibrium position. For instance, a particle initially located beneath the focus of a laser beam (Fig. 1.8 (c)) is pulled towards the focus [39].

The forces generated by classical optical tweezers are of the order of piconewtons, for milliwatts of laser power, and particles up to  $10\ \mu\text{m}$  can commonly be trapped [37].

### 1.3 Nanostructures for optical trapping

Classical optical tweezers have proven to be extremely useful tools. However, they suffer two major drawbacks: first, their bulky nature limits their use to laboratory applications. Secondly, they are intrinsically diffraction-limited and this has negative consequences in the trapping of nano-scaled objects. Gradient forces depend on the polarizability, and as the object to be trapped is reduced in size, its polarizability also decreases. On the contrary, its Brownian motion is increased (Eq. 1.15): it is thus more difficult to obtain stable trapping and few hundreds of milliwatts of optical power can be required. This is particularly inconvenient for biological samples, that can be damaged by such high powers. Proteins can change their shape [68], cell cycles can be stopped [69] and even micrometer-sized bacteria can be damaged [66].

A first strategy to overcome this limit consists in using the gradients created by rapidly decaying evanescent fields in nanostructures and several schemes were suggested. Amongst them,

plasmonic nanostructures, dielectric waveguides and resonant cavities are the most common.

The idea that the large field gradients generated in the evanescent near-field of a metallic tip could be used to trap small particles was suggested by Novotny at the end of the 90's [70]. Ten years later, an experimental demonstration of plasmonic optical trapping was realised by the group of Quidant [71]: optical trapping of few micron-sized polystyrene particles was achieved on a glass substrate patterned with gold pillars. Since then, many schemes have been suggested and plasmonic tweezers showed to have a wide range of applications, especially in the trapping of dielectric [72, 73] and metallic particles [74, 75].

The use of dielectric waveguides, on the other hand, was shown as early as 1996 by Kawata [76] that showed the trapping and the propulsion of both dielectric and metallic micron-sized particles on channel waveguides. This mechanism was used also for biological objects, such as red blood cells [77]. The introduction of slotted waveguides [78] allowed to increase the overlap between the confined field and the objects to analyse, and trapping of  $\lambda$ -DNA molecules and 75 nm dielectric particles. Finally, tapered waveguides were also proposed and used to trap and transport micro and nanoparticles [79].

Finally, a third nanostructure-based trapping scheme makes use of resonant cavities and a large variety of structures was presented, going from ring resonators [80] to photonic crystal cavities. In particular, the possibility of using the field enhancement in a PhC for optical trapping and laser cooling was suggested in 2001 by Toader [81]. In 2006, two papers about optical trapping of particles in 2D PhC cavities were published by Rahmani and Chaumet and by Barth and Benson [82, 83] and in 2009 optical trapping in the vicinity of a 1D photonic crystal cavity was experimentally proven [84]. Bacteria were trapped for the first time on a 2D photonic crystal cavity in 2013 by Mandal [19], opening the way for a range of biological studies.

#### 1.3.1 Backaction

The photonic structures described in the previous section showed great improvements in the reduction of the size and of the trapping power necessary to trap various micro- and nano-sized objects. However, they still present some drawbacks. In particular, plasmonic structures are limited to particles larger than 100 nm because of photothermal effects, and for the same reason they are not adapted for the trapping of biological entities. On the other hand, waveguides do not allow for trapping in one point but only for trapping and propulsion along the waveguide itself.

In all the structures described beforehand, the trapped objects are passive: they are simply trapped but don't participate in the trapping dynamics. Systems where the trapped specimen play an active role in the trapped dynamics are defined as systems that support Self-Induced Back-Action effects.

The concept of SIBA was first introduced in optomechanics, and it can be conceptually

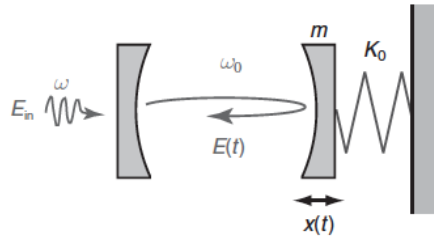


**Figure 1.9** – An optical cavity is coupled to a mechanical oscillator. A displacement in the mirror shifts the resonance frequency of the cavity, which in turn changes the light intensity and hence the force acting on the mirror. Figure from Ref. [63].

understood by considering the system depicted in Fig. 1.9. two mirrors form an optical cavity. One of them is fixed while the other one is connected to a spring. In this way, the optical cavity is coupled to a mechanical oscillator. The system is characterised by the coupling of the cavity field  $E(t)$  and by the displacement  $x(t)$  of the mirror. A displacement of the mirror creates a resonance frequency shift, but at the same time a change in the resonance frequency results in a variation of the light intensity and hence in the force acting on the oscillator. Thus, a displacement of the mirror acts back to itself.

The same idea can be reported in optical trapping, while considering resonant structures: the trapping field acts on the particle, but at the same time the specimen acts on the field. This idea was suggested by the beforehand cited paper of Barth and Benson, and several experimental evidences have been reported. Several systems can support SIBA effects, amongst them photonic crystal cavities [85, 86, 87] and plasmonic structures [88]. In all cases the basic phenomenon consists in the fact that the frequency of the trapping beam is altered by the position of the trapped object and this leads to an active contribution of the trapped specimen in the trapping dynamics.

To illustrate this, the trapping dynamics of our cavity is considered. As a matter of fact, two trapping regimes are supported by our cavity. They can both be described in terms of SIBA effects and they will be detailed in Chapter 4. In Fig. 1.10 the case of the “cage regime” is illustrated: the cavity is excited at its resonance wavelength, thus a maximum of the field is confined in it. A particle in the vicinity of the cavity will thus experience the gradient forces and be trapped. However, in this way, the resonance wavelength varies, as the medium overlapping with the field changes, resulting in a decoupling between the excitation mode and the cavity one. Free to move by Brownian motion, the particle will thus escape from the cavity region, but as soon as it happens, the resonance wavelength is shifted back and the gradient forces are restored. This results in a dynamic trapping mechanism, where the particle is a “free particle in a cage” and where the temporary “freedom” of the particle is generated by the particle itself.

One major advantage of exploiting SIBA effects is that stable confinement in a dynamic trap requires much lower average intensities compared with a static potential [89]. In addition, information on the trapped object can be retrieved by observing the field variations and thus

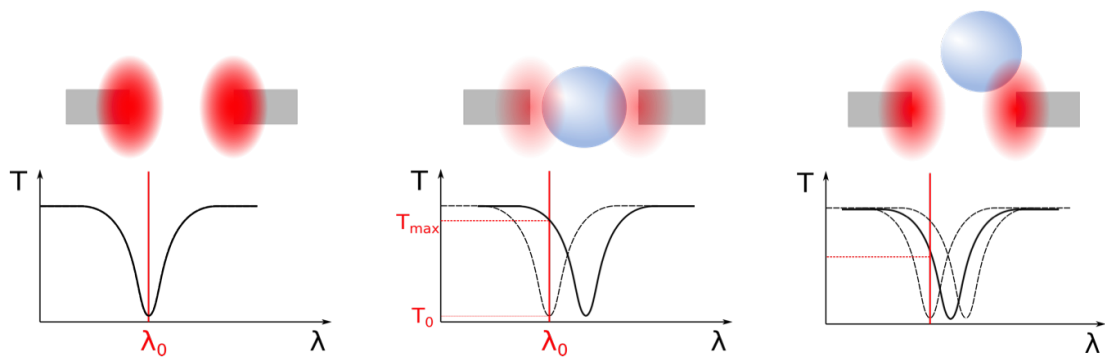


**Figure 1.10** – Schematic representation of the SIBA effect in the “cage configuration”. (a) The cavity is excited at its resonance wavelength,  $\lambda_0$ , and a maximum of the field is confined. (b) When a particle is trapped, a redshift in the resonance wavelength is induced and the field is de-coupled. (c) The particle is free to move by Brownian motion away from the cavity region but as soon as it happens, the field is coupled again and the trapping forces are restored.

this kind of system is particularly suitable for biological analysis.

## 1.4 Optofluidic chip

To exploit the trapping capabilities of nanostructures, in most cases it is essential to immerse them in aqueous environments, where the objects to be trapped are suspended. Starting from the 90's, the development of the first microfluidic techniques [90] allowed for the control of the movement of liquids in micro-channels and in the 2000s technologies based on molding micro-channels in polymers such as PDMS (polydimethylsiloxane) [91, 92] experienced a huge growth, pushed by the arising research in the development of lab-on-a-chip devices [93].

In particular, the integration of photonic structures with microfluidic systems, i.e. the so-called optofluidic systems, have become more and more popular during the last decade, especially for biological and bio-medical applications [94, 95]. This success is mainly due to the fact that microfluidics layers are easy of fabrication, low cost, highly bio-compatible and that they made it possible to create “lab-on-a-chip” devices.

Depending on the application, a large variety of materials is used: silicon [96], glass, hydrogels, paper [97] and predominantly polymers [98] such as SU8, polystyrene (PS), cyclic olefin copolymer (COC) and polydimethylsiloxane (PDMS) [99, 92, 100, 101]. In particular, PDMS is the most used material in research laboratories due to its simple manufacturing using soft lithography techniques [102, 103]. Moreover, hybrid platforms consisting in the combination of layers of different materials are used in multilayers systems that allow for the creation of elements like valves or mixers [104, 105].

In our case, the photonic chip is integrated with two microfluidic layers of different materials. A thin (30  $\mu\text{m}$ ) PDMS layer contains channels that allow for the transport of nanoparticles and of bacteria on the photonic crystal structures. Moreover, this layer is covered by a glass

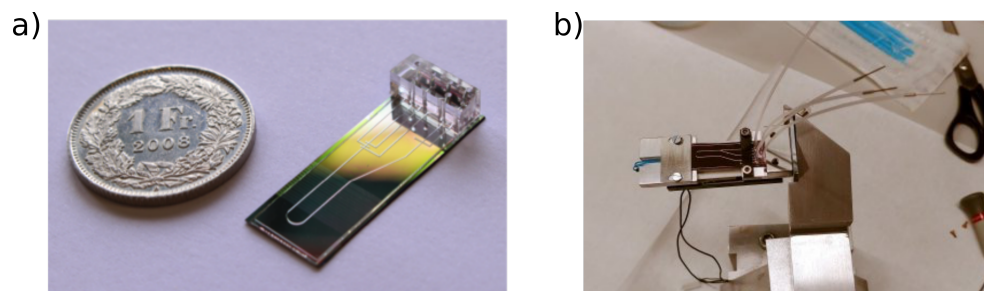


**Figure 1.11** – (a) Picture of one of the optofluidic chips used during this thesis. On top of the silicon PhC chip a PDMS layer contains transport channels. A glass coverslip ensures robustness and excellent optical access and finally a thick PDMS block allows for tubes injection. Picture from Ref. [105]. (b) An optofluidic chip mounted with tubes on its sample holder.

coverslip that gives excellent optical access from the top and sample robustness. In addition, channels are etched in the glass layer to allow for flux control. Finally, a thick (3 mm) PDMS block enables the connection of the optofluidic chip to tubes for liquid injection. The sample is shown in Fig. 1.11 and the microfluidic integration will be detailed in Section 2.9.



## 2 Fabrication

### 2.1 Process overview

In this section, a brief description of the fabrication process will be given; a detailed discussion of each step can be found in the following sections. The entire process is performed at EPFL, in the Institute of Physics (IPHYS) and CMi (Center of Micronanotechnology) cleanrooms, and it is based on the one developed by previous students of the group. During this thesis, the existing recipes were optimized, some steps were added (SU8 mode adaptors for the 2D photonic crystals) and the competences to realize some of the steps that previously were carried out by the technical staff were obtained. In particular, this is the case of the chrome masks fabrication and of the anti-reflection coating deposition. The optofluidic sample is fabricated in a top-down approach using techniques widely employed in semiconductor processing. The main steps are illustrated in Fig. 2.1

The starting material is a Silicon-On-Insulator (SOI) 8 inches wafer from SOITEC (ref. G8P-110-01). It consists in a 220 nm silicon layer and in a 2  $\mu\text{m}$  sacrificial  $\text{SiO}_2$  layer on top of a 750  $\mu\text{m}$  silicon substrate. The silicon orientation is [100]. Before starting the processing, the wafer is diced in pieces and the substrate thickness is reduced to 250  $\mu\text{m}$  by mechanical polishing, to facilitate the final cleaving.

The desired pattern is first defined with electron beam lithography and further transferred onto the silicon layer by dry etching with a gas mixture of  $\text{SF}_6$  and  $\text{C}_4\text{F}_8$  in an Inductively Coupled Plasma (ICP) etcher. A resist coating, followed by UV lithography, is then performed to protect the entire surface of the sample except for the PhC structures. The sample is next immersed in a Buffered HydroFluoric acid (BHF) solution that removes the sacrificial  $\text{SiO}_2$  layer and leaves the photonic crystal membranes fully suspended. Optical coupling to the photonic crystal structures is achieved through waveguides in an end-fire setup, with the sample cleaved at the extremities of the waveguides. To optimize the coupling between the lensed fibers and the waveguides, and to avoid Fabry-Perot interferences due to reflections between the cleaved facets, either anti-reflection coating or SU8 mode adaptors are created. Finally, the photonic chip is integrated with microfluidic layers, consisting in a PDMS membrane and in a glass

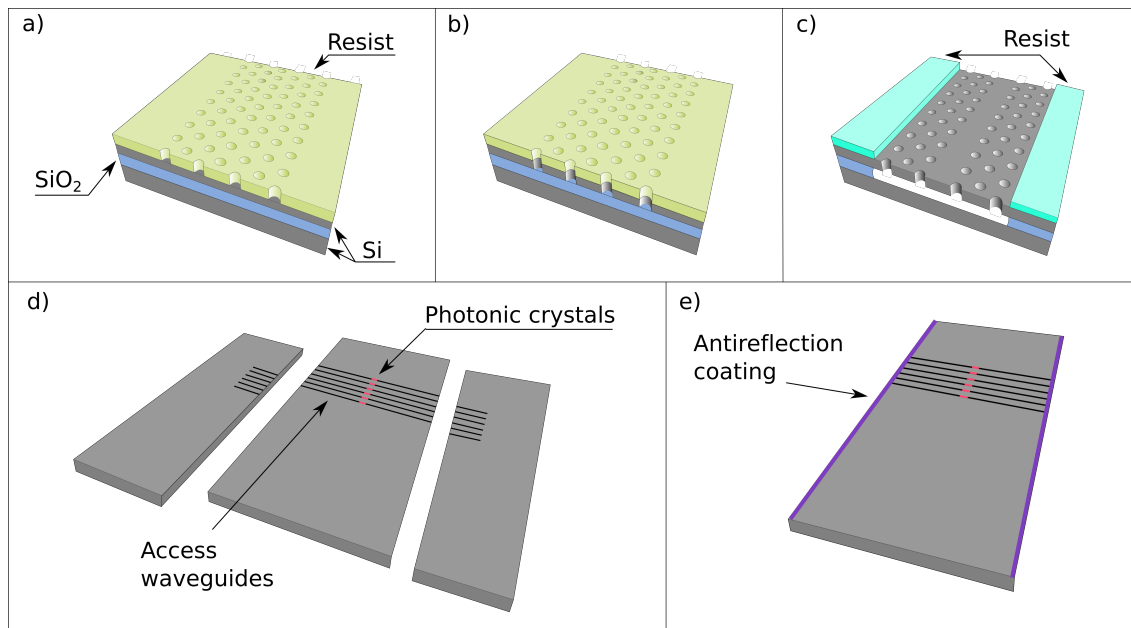


**Figure 2.1** – Main steps of the fabrication process: the patterns is first defined with ebeam lithography (a) and transferred to silicon with ICP etching (b). The photonic crystal structures are suspended via wet etching (c) and the sample is cleaved (d) to enable end-fire coupling. Finally, an anti-reflection coating is deposited (e) to prevent Fabry-Perot interferences between the facets.

coverslip.

## 2.2 Lithographic techniques

The fabrication process relies largely on the use of lithographic techniques. They make use of polymers (“photoresists” or simply “resists”) that are sensitive to light (in the case of photolithography) or to electrons (in the case of ebeam lithography). The resist is first coated on the substrate and then the desired pattern is defined by exposing it to a high-energy beam that modifies the resist structure when the exposure dose (with the units of an energy density,  $\text{mJ}/\text{cm}^2$ ) surpasses a threshold value. Depending on the reaction that is induced, the resists can be divided in two groups: positive resists or negative ones. In positive resists the impinging beam degrades the material by breaking the molecular chains, while in negative resists it causes molecular cross-linking. After exposure, a solvent (called developer) is applied on the surface of the resist and the weakest parts are washed away: the exposed regions in the case of positive resist and the non-exposed ones in the case of negative resist. The process is shown in Fig. 2.2.

The pattern can be drawn onto the resist surface either by direct writing or by using a mask (Fig. 2.3). In the direct writing case, the beam is focused on the resist surface and exposure is achieved by scanning the surface. If a mask is used, on the other hand, a single exposure to the light source is needed, with the mask that allows for pattern transfer by blocking parts of

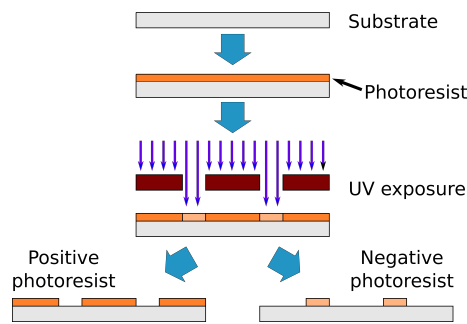


Figure 2.2 – Schematic representation of a photolithography process.

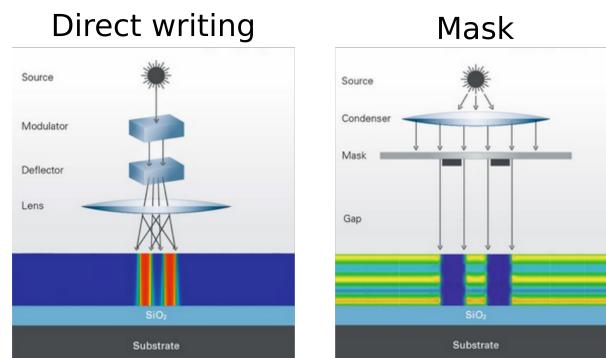


Figure 2.3 – Two possibilities to perform photolithography: by direct writing or using a mask. Adapted from Ref. [106].

the incoming light. More details on the different types of lithographic techniques used will be presented in the following sections.

## 2.3 Cr masks fabrication

Several of the fabrication steps are performed through UV lithography and make use of a hard chrome mask. One preliminary step consists therefore in the mask fabrication. The process is performed on a 5”x5” photoresist-coated Cr mask (Nanofilm, 90 nm of Cr, 500 nm of AZ1518 photoresist) by direct writing with a Heidelberg VPG200 photoresist laser writer and it is illustrated in Fig. 2.4. Illumination is provided by a high energy UV laser and the writing is performed through mechanical scan, synchronized with the laser pulse. Two parallel beams are used, to reduce edge roughness. Moreover, three different front lenses, referred to as “Writing Head (WH)”, can be chosen: they give different spot sizes and hence different resolutions and writing speeds, as reported in Tab. 2.1. Features as small as 0.6 μm can be obtained with the 4 mm focal length WH and in our case it is used for few micron-sized structures. Larger structures are exposed with the standard 10 mm focal length WH.

The file is first created with a CAD software (Tanner L-Edit) in GDSII format and then it is fractured and converted to the format used by the tool with the dedicated *x-convert* software.

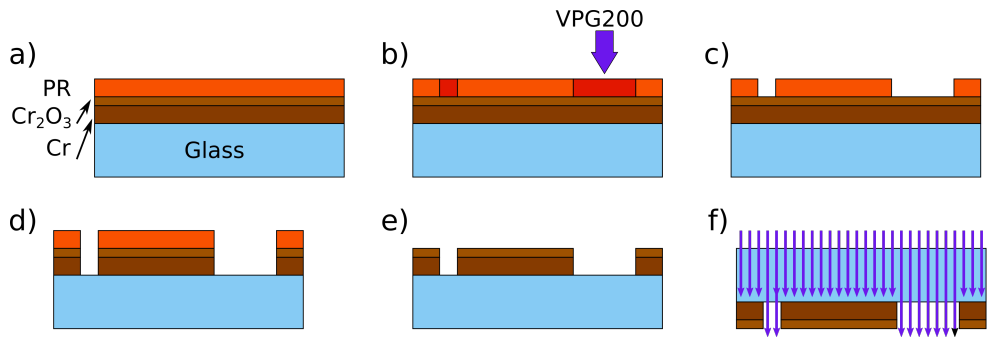


Figure 2.4 – Cr mask fabrication steps.

Write mode	Advanced	Standard	Fast
WH focal length	4 mm	10 mm	20 mm
Beam spot diameter (μm)	0.55/0.65	0.9/10	1.8/2.5

Table 2.1 – Beam spot diameters for the 3 available writing heads at CMi. Values obtained from [107].

During this step, the pattern is divided in vertical stripes, the thickness of which depends on the required resolution. Finally, it is also possible to mirror the pattern, if it was not previously done in the GDSII file: the reason is that during operation the Cr mask will be used “upside-down” and the resulting mirroring needs to be taken into account. After writing, the mask fabrication is finalized by an automatic Hamatech HMR 900 mask processor: the photoresist is first developed (with AZ 351 and De-Ionized (DI) water in a 1:3 ratio), then the chromium is etched (with CR0), the remaining resist is stripped (with pure AZ400K) and finally the mask is rinsed and dried.

Cr masks were fabricated for several subsequent steps: for the membrane suspension (section 2.6.1), for the SU8 mode adaptors (section 2.8) and for the fabrication of the mold used to create microfluidic channels (section 2.10).

## 2.4 Pattern definition: electron beam lithography

For pattern definition a Raith EBPG5000+ electron beam lithography (EBL, often referred to as ebeam lithography) system is used. EBL systems provide a resolution suitable for nm-scale features, thus they are the tool of choice for photonic crystals fabrication, where the critical dimensions are of the order of tenths of nanometers. A very high resolution in pattern definition is crucial to obtain good quality structures, as the defects in the pattern are propagated and amplified through the subsequent fabrication steps. In particular, for the PhC fabrication it is important to draw holes as circular as possible to ensure the correct periodic alternation air/silicon that gives rise to the photonic bandgap. Moreover, having circular shape as smooth as possible limits the scattering losses that lead to degradation of the Q factor.

Electron beam lithography is performed through direct writing: an electron beam scans

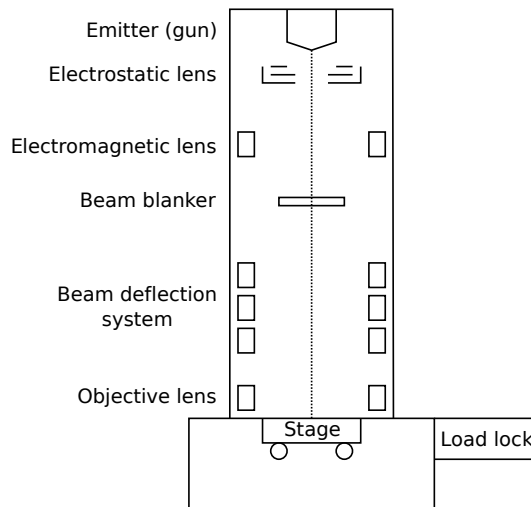


**Figure 2.5** – Schematic representation on an EBL system.

the surface of the electron-sensitive photoresist, in our case ZEP520A. An EBL system is represented in Fig. 2.5. Schematically, it consists in an ultra-high vacuum chamber set on a vibration-isolated support that contains an electron source and electromagnetic lenses. In the EBPG5000+, electrons with energy of 100 keV are generated by thermal field emission and accelerated through a column containing deflector coils and electromagnetic lenses to adjust and focus the beam, as well as a blanking unit to rapidly switch on/off the beam during scan. Gaussian beams can be chosen with currents ranging from 100 pA to 200 nA, corresponding to spot sizes comprised between 4.2 nm and 100 nm [108]. The pattern is divided into pixels, the size of which determines the resolution, and the writing is done by exposing the single pixels one after the other. The writing time, as well as the smoothness of the written shape, is thus directly related to the chosen resolution. Different combinations between pixel size and spot size are possible, provided that the resulting writing frequency is not exceeding the maximum frequency of the system, 50 MHz. The final quality of the designed pattern is the result of the combination of resolution, beam size and dose delivered to the resist and the writing time needs also to be taken into account. Those aspects will be treated separately in the following subsections.

### 2.4.1 Mask preparation: pattern fracturing

The desired pattern is first created with Tanner L-Edit software and exported in .gds format. During the design, a grid of 1 nm is chosen, that corresponds to the minimum beam step provided by the EBPG5000+. The pattern is then fractured with GenISys Layout Beamer software and transformed in a .gpf file that will be used by the ebeam tool: in this procedure, the pattern is broken down into small polygons that will be swept by the ebeam scan. This step defines the number and the position of pixels, as well as the order in which the pixels will be exposed by the electron beam. As the writing time depends on the number of pixels and

the whole pattern extends over a few square millimeters area, different resolutions are used for different parts of the design: for photonic crystals, the smallest pixel size of 1 nm is chosen, while for waveguides and alignment marks a resolution of 20 nm is employed, to accelerate the exposure. In Fig. 2.6 the example of a fracturing of a 100 nm radius hole is presented. Resolutions of 1 nm (a) and 5 nm (b) are used and it is evident that for good quality circular shape the 1nm resolution is required.

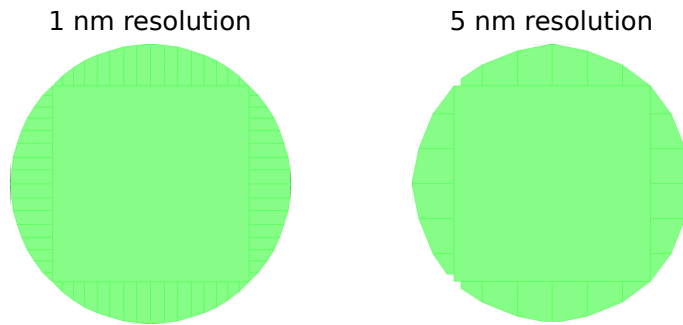


Figure 2.6 – A 100 nm radius holes fractured with 1 nm resolution (a) and with 5 nm resolution (b).

To increase further the smoothness of circular edges, it is possible to use a sequencing fracturing mode, consisting in dividing the hole in an inner part surrounded by a ring-shaped outer part, called sleeve. The advantage of this fracturing mode resides in the fact that the outer sleeve is written in a concentric way, in opposition to what happens in the curved one, where polygons are scanned one after the other (Fig. 2.7). This ensures a better hole symmetry, but on the other hand it is very time-consuming as the displacements on the sample surface are larger. Moreover, it creates a very large .gpf file (easily of the order of 10 GB) that is more difficult for the tool to handle. During this thesis, most of the photonic crystals were fabricated using a curved fracturing mode with 1 nm resolution.

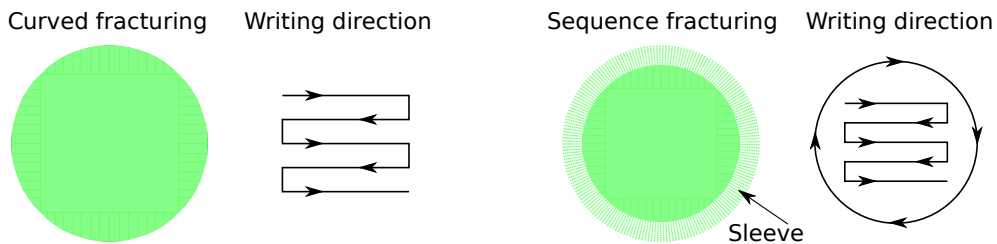
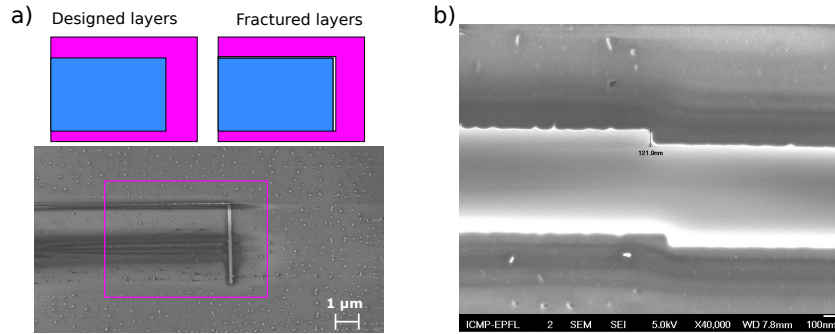


Figure 2.7 – A 100 nm radius hole fractured with curved mode (a) and with sequence mode (b). In sequence mode, the pixels of the sleeve are exposed concentrically.

During the fracturing procedure, the writing fields are also defined. In fact, the position of the beam on the sample surface is determined by a beam deflection system (Fig. 2.5) formed by electromagnetic coils. However, those coils can only deflect the beam by a few 100 microns. The pattern is thus divided into smaller parts called writing fields, whose size depends on the setted resolution. Once the region included in a field is exposed, the stage moves to another field, and so on until the full pattern is covered. The junction between patterns belonging to two different fields (stitching) is delicate and crucial for the final quality of the structure.

Typically the EBPG5000+ stitches fields with an accuracy of 18 nm, but stitching errors may occur during the fracturing procedure (Fig. 2.8) or in the case of thermal drift of the beam. To minimize the damage that could be induced by bad stitching, it is possible to define floating writing fields, in opposition to fixed ones (Fig. 2.9 (a),(b)). With this technique, it is possible to have photonic crystals fully contained in a field, as showed in Fig. 2.9(c).



**Figure 2.8** – Two examples of stitching errors. (a) The fracturing induced a shift between to layers. (b) Stitching induced by thermal drift, resulting in a bad connection between writing fields. Both samples are slightly underexposed and the silicon is not completely removed.

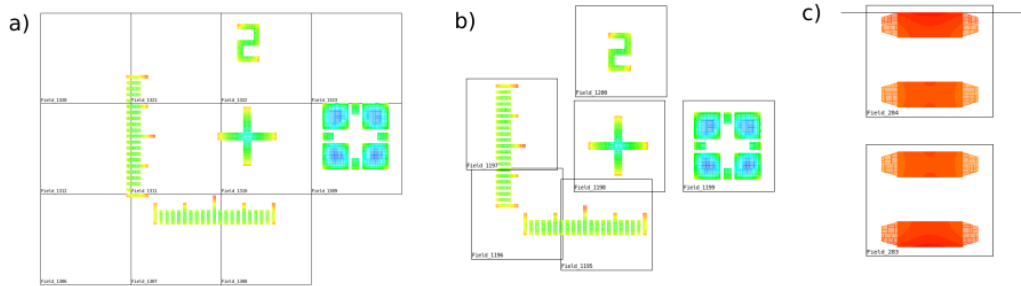


**Figure 2.9** – (a) An alignment mark divided into fixed writing fields. (b) The same alignment mark divided into floating fields. (c) Every writing field fully contains two photonic crystals.

### 2.4.2 Dose determination

To obtain high pattern quality a correct dose determination is crucial, besides the use of the best resolution achievable. The dose for ebeam exposure is typically expressed in  $\mu C/cm^2$  and it is given by:

$$D \left[ \frac{\mu C}{cm^2} \right] = \frac{10^3 \cdot I_{beam} [pA]}{f_{shot} [MHz] \cdot \Delta x^2 [nm]} \quad (2.1)$$

where  $I_{beam}$  is the current of the beam,  $f_{shot}$  is the exposure frequency and  $\Delta x$  is the beam step size. However, a precise dose determination has to be carried out experimentally through dose tests as it depends on many aspects, such as the resist thickness, the temperature and

humidity of the processing room, the thermal processing story of the resist and the pattern density. For ZEP resist and 100 keV electrons, typical doses are comprised between 160 and 400  $\mu C/cm^2$ . In our case, a dose of 165  $\mu C/cm^2$  was used.

Regarding the pattern density, proximity effects can be observed due to the interactions with neighboring exposed pixels. In fact, during exposure, impinging electrons interact with the atoms of the resist and of the substrate and scattering events occur, both elastic and inelastic. Secondary electrons are created when inelastic collisions occur, and they propagate in the material following random walks. Moreover, impinging electrons can elastically collide with the atomic nuclei and they can be backscattered. Forward scattering can also happen, when electrons collide with the electronic cloud of the atoms, and their initial trajectory is modified, generally enlarging the shape of the beam.

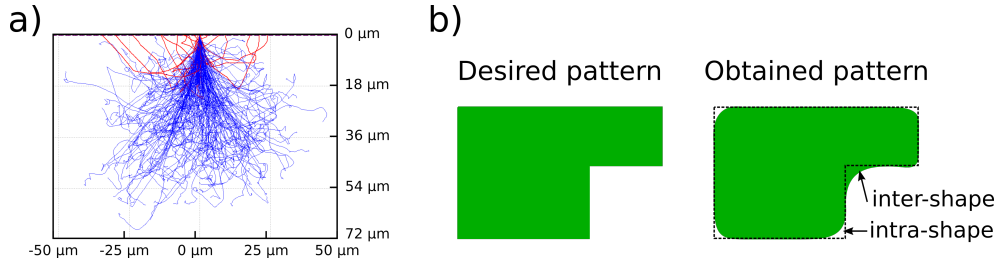


**Figure 2.10** – (a) Simulation of a 100 keV beam impinging on a 200 nm ZEP520A layer on top of a silicon substrate. Blue lines correspond to the secondary electrons trajectories, while red lines to the backscattered electrons ones. (b) The two types of proximity effects that can occur.

The sum of those interactions gives rise to the typical “pear-shape” that is created when electrons penetrate a material, as illustrated in Fig. 2.10 (a) that represents a Monte Carlo simulation of a 5 nm beam of 100 keV electrons impinging on a 200 nm ZEP520A layer on top of a silicon substrate. The simulation was performed with CASINO software [109]. The secondary and backscattered electrons can have sufficient energy to break the molecular bonds of the resist (ZEP520A is a positive resist), thus enlarging the actual exposed region. Proximity effects can extend over a 30 microns distance, and they can be divided in two classes: intra-shape and inter-shape (Fig. 2.10 (b)). Intra-shape proximity effects consist in the under-exposure of the smaller features with respect to the bigger ones when exposed with the same dose: a smaller number of neighboring pixels contribute with scattered electrons. Inter-shape effects, on the contrary, consist in a over-exposure of regions densely patterned, because of the large number of neighboring pixels. One possible solution consists in varying the dose depending on the pattern density and it can be done using a dedicated module in the Layout Beamer software. The proximity effects correction algorithm is based on the point spread function of every pixel that is usually expressed as the sum of a short range and of a long range terms as follows:

$$PSF(r) = \frac{1}{1 + \eta} \left( \frac{1}{\pi\alpha^2} e^{-\left(\frac{r}{\alpha}\right)^2} + \frac{\eta}{\pi\beta^2} e^{-\left(\frac{r}{\beta}\right)^2} \right) \quad (2.2)$$



where  $\eta$  is the ratio of the backscattering component to the forward-scattering one,  $\alpha$  is the forward scattering parameter and  $\beta$  is the backscattering range parameter.

### 2.4.3 Sample preparation

As mentioned before, the resist used is ZEP 502A, diluted at 50% and spin-coated on the sample for 30 seconds at 1500 rpm to obtain a 200 nm layer. Before spin-coating the resist, the surface is carefully cleaned with acetone in an ultrasonic bath and rinsed with isopropanol. This procedure is repeated until the surface is perfectly clean under microscope inspection, both in bright and in dark field. The sample is then placed on a hotplate at 115 °C to evaporate solvents and hence obtaining better resist adhesion. After coating, it is baked for 3 minutes at 180 °C. The sample is then let to cool down to room temperature and finally mounted on the ebeam sample-holder, showed in Fig. 2.11.

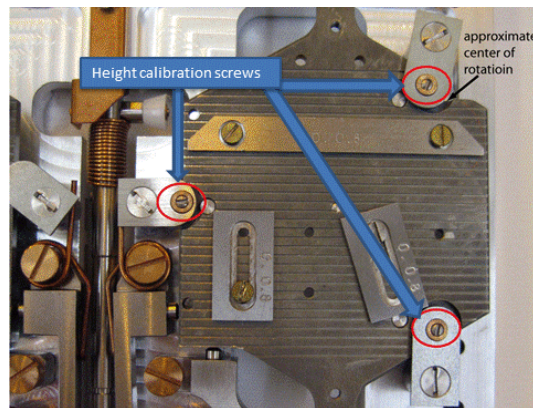


**Figure 2.11** – Ebeam sample holder used for chips.

The sample is attached with metallic clamps and copper tape and precision screws allow for height calibration that is controlled with a laser interferometer. Before exposure, the ebeam tool will automatically measure the height and focus the beam accordingly, but the resist surface has to lie in a distance of  $\pm 50 \mu\text{m}$  from the tool reference. Moreover, the surface has to be as flat as possible to avoid distortions due to the beam impinging not perpendicularly. To this aim, special attention also needs to be paid while attaching the sample, especially in the case of our substrates that are relatively large and thin (25x30 mm in size, per only 250  $\mu\text{m}$  in thickness). In fact, while attaching the sample, the central part (where the pattern will be written) cannot be touched and the sample has the tendency to bend, with the central part at a larger height with respect to the edges. This difference due to bending can go up to 40  $\mu\text{m}$ . To reduce this inconvenience, very careful manipulation is required. Another strategy consists in using a thicker sample and in thinning the substrate by mechanical polishing after the ICP etching. Additionally, the sample is aligned with respect to the crystalline axis, so that the waveguides will be perpendicular to the cleaved facets. Finally, the holder is put on a water-cooled plate in the transfer SAS between the ebeam tool chamber and the resist processing room. This brings the sample at a temperature as close as possible to the one of the

stage inside the tool, minimizing then thermal drift effects that could induce stitching errors between writing fields. Once charged into the processing chamber, the sample is also left 10 minutes to fully thermalize with the stage and prevent thermal drift.

### 2.4.4 Exposure

The last step consists in choosing a beam size per every layer of the design. Edge smoothness depends on the beam size: a beam larger than the step size has to be selected, so that flat edges are obtained from the superposition of circular profiles, as shown in Fig. 2.12. For every resolution, the largest possible beam is chosen, fulfilling the condition of a writing frequency  $< 50$  MHz as required by the tool. For 1 nm resolution the 100 pA beam is used, with a spot size of 4.2 nm, while for 20 nm resolution the 30 nA beam is selected, with a spot size of 18.8 nm. To reduce irregularities in the shape of the waveguides due to the fact that the 30 nA beam is smaller than the required pattern resolution, the resist is overexposed: a dose of  $200 \mu\text{C}/\text{cm}^2$  is used instead of  $165 \mu\text{C}/\text{cm}^2$ .

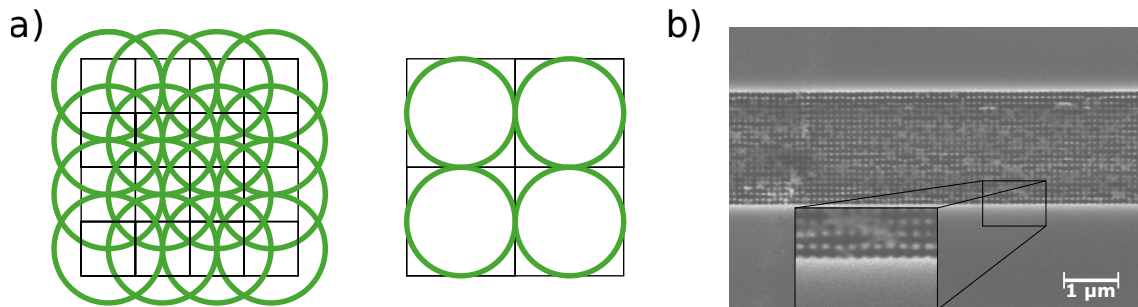


**Figure 2.12** – (a) For better edge smoothness a beam larger than the pixel size is required. (b) SEM image of a waveguide exposed with a 11.5 nm beam for a 20 nm resolution. Individual beam shots can be seen, resulting in an undesired patterning of the waveguide edges.

After exposure, the sample is developed in n-Amilacetate for 1 minute and rinsed in a 90:10 solution of methyl isobutyl ketone (MiBK) and isopropanol (IPA) for 1 minute. It is finally blow-dried and the surface is inspected with an optical microscope.

## 2.5 Pattern transfer: ICP etching

For pattern transfer[110], an Alcatel AMS 200 ICP etcher is used. ICP etchers provide a strongly directional material etching, and therefore they are suitable for photonic crystals fabrication, where a high verticality of the holes sidewalls is desired. The verticality and the smoothness of the sidewalls of the holes that ICP etchers can ensure are crucial aspects for the photonic crystals quality. First, a good verticality and smoothness of the sidewalls surface are necessary to establish the correct periodicity of the air/silicon alternation that gives rise to the photonic bandgap. Secondly, a good verticality is necessary to maintain the symmetry along the y-axis of the slab and hence avoid TE/TM mode mixing: in fact, our cavities are developed to work

in TE. Finally, it is important to develop recipes that limit as much as possible the surface roughness of the sidewalls, as it will introduce scattering losses for the confined light.

An ICP processing chamber is depicted in Fig. 2.13. Schematically, it consists in a plasma source, a diffusion chamber and a substrate holder.

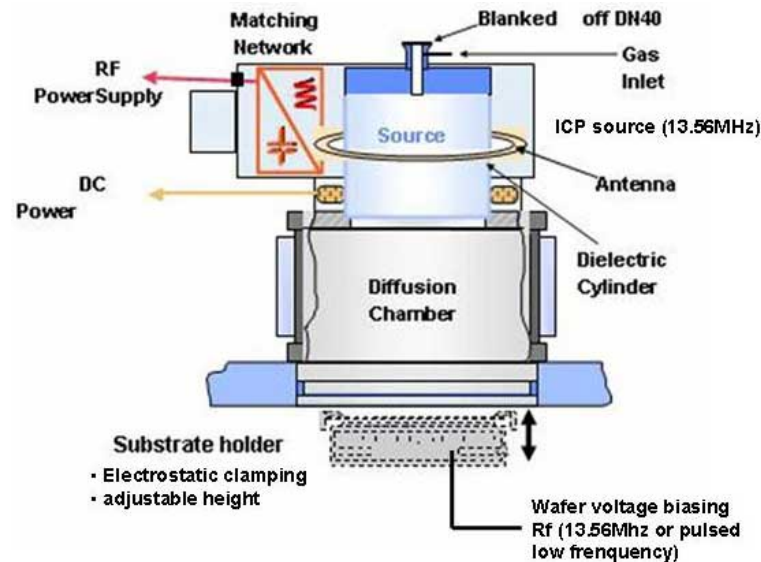


**Figure 2.13** – Schematic representation of the Alcatel AMS200 ICP etcher. Picture from Ref. [111].

The etching mechanism relies in the combination of both physical and chemical etching: reactive ions are created via the plasma ignition of the etchant gases and then accelerated towards the surface of the sample. The physical etching due to collisions between the impinging ions/radicals and the material atoms is largely enhanced by the chemical reactions that occur between the plasma species and the target, that break the material bonds and create volatile products that are subsequently evacuated. This second mechanism is strongly material selective with suitable choice of chemistry; it increases the etching rate but its chemical nature gives rise to an isotropic etching, in opposition to the desired anisotropy. During the recipe development, the verticality of the sidewalls is favoured over the etching rate.

In ICP etchers, the plasma is generated via electromagnetic induction. In the AMS 200, the ICP source is formed by an alumina cylinder ringed by an antenna connected to an RF power supply, operating at 13.56 MHz. A second RF generator provides the wafer voltage biasing necessary to accelerate the ions vertically across the chamber, where plasma uniformity is also achieved. The low pressure in the chamber (of the order of  $10^{-2}$  mbar) ensures normal incidence of the impinging ions. For good quality etching the control and stability of the substrate temperature is also important and it is ensured by helium backside cooling of the wafer. Finally, the substrate height can be controlled and usually is setted at 200 mm.

For silicon etching,  $\text{SF}_6$  and  $\text{C}_4\text{F}_8$  gases are used, with a flow of 25 sccm and 55 sccm respectively. The etching chamber pressure is  $3 \times 10^{-2}$  mbar and the RF generator power is 1500 W.

## Chapter 2. Fabrication

For this process, the selectivity with respect to ZEP520A is larger than 10:1. The substrate holder temperature is set to 20 °C .

On the etching dynamic point of view, SF<sub>6</sub> ions react with the silicon surface creating SiF<sub>4</sub>, a volatile compound that will diffuse in the chamber. To prevent horizontal etching of the silicon due to reactions with the plasma radicals, which happen isotropically, C<sub>4</sub>F<sub>8</sub> gas is used: CF<sub>2</sub> molecules are absorbed by the silicon surface and create a protective polymer layer. Vertically driven ions remove the bottom layer of the film and the etching can continue on the bottom of the hole obtaining high quality vertical sidewalls.

Finally, the desired etching time is determined using a test sample few hours before the actual etching: the etching rate of the machine is slightly varying with time and it is important to set a time long enough to fully etch the 220 nm of silicon but without overetching the silica layer. Both underetching and overetching introduce distortion in the cylindrical shape of the holes. An etching time around 2 minutes is usually used. Fig. 2.14 shows a SEM image of the cross sections of a test sample correctly etched: 10 nm of the underlying silica is also etched, to ensure complete etching of the holes.

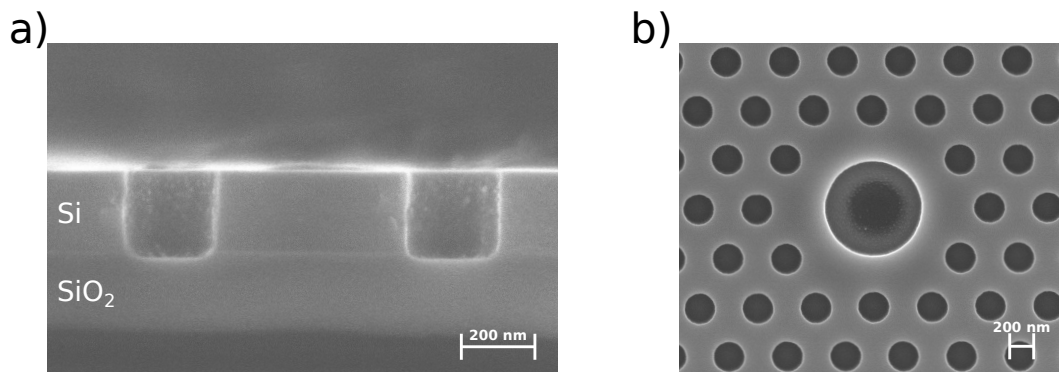


**Figure 2.14** – (a) SEM detail of the cross section of a test sample correctly etched. (b) Top view of the cavity region after ICP a etching. The slightly etched silica is visible in the larger hole.

After etching, the remaining ZEP layer is removed with acetone, rinsed with isopropanol and blow-dried with nitrogen.

One last remark on the practical side of view: the AMS200 tool works with 4 inches wafers. In our case, 25x30 mm chips are used. It is thus necessary to attach them on a silicon carrier wafer. In this operation, it is very important to ensure the thermal contact between the sample and the wafer and to avoid the creation of any tilt that would result in the ions impinging on the surface with an angle. In particular, the thermal contact is crucial for two reasons: first, the temperature at the surface of the sample strongly affects the etching process, as the chemical reactions are temperature-dependent. Secondly, a bad thermal contact between the sample and the wafer prevents its correct cooling: in the worst case, if high temperatures are reached, ZEP520A can crack and burn. If this happens, ZEP removal is impossible even with oxygen plasma.

To attach the sample to the carrier wafer 3 methods were used:

- Kapton tape: the sample is attached with 4 disks of Kapton tape on top of the corners. Kapton has very high mechanical, chemical and thermal stability and is therefore suitable to be used in an ICP chamber without the risk of contaminations. It is the easiest of the 3 solutions proposed, but for relatively large and thin samples as ours, the results obtained were negative. As reported in the section 2.4.3, concerning the mounting of the sample on the ebeam holder, a bending of the sample is observed while attaching it from the top, with the central part higher with respect to the edges. This results in an air gap between the sample and the carrier wafer that precludes proper thermal contact. The ZEP burning observed was caused by this technique.
- QuickStick™135 (QS135): it is a thermoplastic polymer widely used in processing applications for temporary mounting. Its hardness and strength give excellent mechanical stability, together with good thermal conductivity. Moreover, it dissolves very easily in acetone leaving no residues. Unfortunately this method is not adapted to samples coated with ZEP 520A. QuickStick 135 softening and melting points are 71 °C and 135 °C respectively: to attach the sample it is thus necessary to heat the wafer, carefully mount the sample and finally wait for the wafer to cool down to room temperature. When using QuickStick at 135 °C, deterioration of the pattern was observed, which was related to a softening of the ZEP. On the other hand, temperatures as low as 106 °C were used, but the not complete melting made difficult to achieve a perfectly flat layer of Quickstick between the sample and the wafer carrier, resulting in the sample surface not perpendicular to the accelerated ions.
- Fomblin®: it is an oil with excellent thermal stability. In this case, the bonding between the sample and the wafer is obtained through viscous forces. A small drop of Fomblin® is deposited on the wafer and the sample is placed on top. The corners of the sample are gently pressed to force the drop to spread, resulting in a very thin layer. To avoid ICP chamber contamination, it is important that the drop is fully covered by the sample. This technique was used in the majority of the process runs performed during this thesis.

## 2.6 Membrane suspension

To have better field confinement in the cavity region, the highest refractive index contrast between the silicon slab and the surrounding medium is pursued (Section 1.1). The photonic crystals are thus suspended, so they can be fully immersed in air or water. On the other hand, for better robustness of the waveguides (and to allow the creation of SU8 mode adaptors, as it will be discussed in section 2.8) they are left to lie on the silica layer. The etching of the sacrificial silica layer is performed via wet etching with a BHF solution and some steps are necessary before the actual etching: the sample surface needs first to be protected, except the

PhC regions, so that the etching of the silica layer will happen only under the photonic crystals. This will result in suspended PhC membranes, leaving at the same time the waveguides laying on the SiO<sub>2</sub> substrate. Secondly, the cleaving of the facets (that will enable fiber-to-waveguide coupling) is performed before the release of the membrane to avoid the breaking of the PhC that could happen due to its minute thickness (220 nm). Those steps are now discussed in details.

### 2.6.1 Sample preparation: AZ5214 coating

To protect the surface of the sample, a coating with AZ5214 positive resist is performed. Some “windows” are then open on top of the photonic crystals (Fig. 2.15) by exposing the resist to UV light with the help of a Cr mask: only the silica regions without protection will be etched, resulting in suspended PhC membranes. Before coating the AZ5214, ZEP520A is first removed

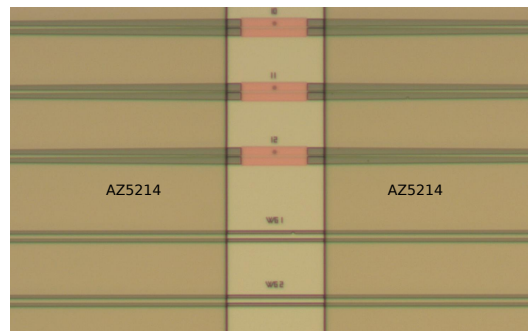


**Figure 2.15** – Sample preparation: the regions protected by photoresist will not be affected by wet etching.

by immersing the sample for 2 hours in acetone, and then in an ultrasonic bath for 3 minutes. The sample is then rinsed with IPA and finally blow-dried. Moreover, it is baked at 115 °C for 1 minute to ensure solvent evaporation and subsequently let 5 minutes to cool down to room temperature. The surface is further prepared by coating it with an adhesion promoter, hexamethyldisilazane (HDMS) for 10 s at 5000 rpm. AZ5214 is then coated for 40 s at 5000 rpm and soft-baked for 6 minutes at 90 °C. The exposure to UV is performed with a Süss MA6 mask aligner: a dose of 140 mJ/cm<sup>2</sup> is delivered to the resist by exposing it for 7 seconds to a lamp power of 20 mW. The sample is then developed in MF139 for 60 s and rinsed in DI water for 15 s. The surface is inspected with a microscope both in bright and in dark field to ensure that the resist is completely removed from the regions of interest, and if it is the case a hard-bake process is performed for 15 minutes at 115 °C to improve film adhesion. During the first fabrication runs, after resist removal with acetone, residues of AZ5214 were observed at the edges of the exposed regions that were caused by some resist stuck to the Cr mask (Fig. 2.16 (a) and (b)). As the residues were not touching the photonic crystals, they were not compromising their optical quality. However, some precautions were taken during the subsequent fabrication runs to avoid their formation (Fig. 2.16 (c)). First, a very thorough cleaning of the Cr mask was performed. In fact, the exposure is carried out after



bringing the sample in hard contact with the mask and some AZ5214 can stick to the mask, in particular close to the Cr edges, and prevent future contact. Moreover, the soft-bake time was increased with respect to previous recipe from 5 to 6 minutes, to take into account the cleanroom temperature of 19 °C. A sufficient soft-bake step is indeed necessary to completely dry the resist and prevent its sticking to the mask.

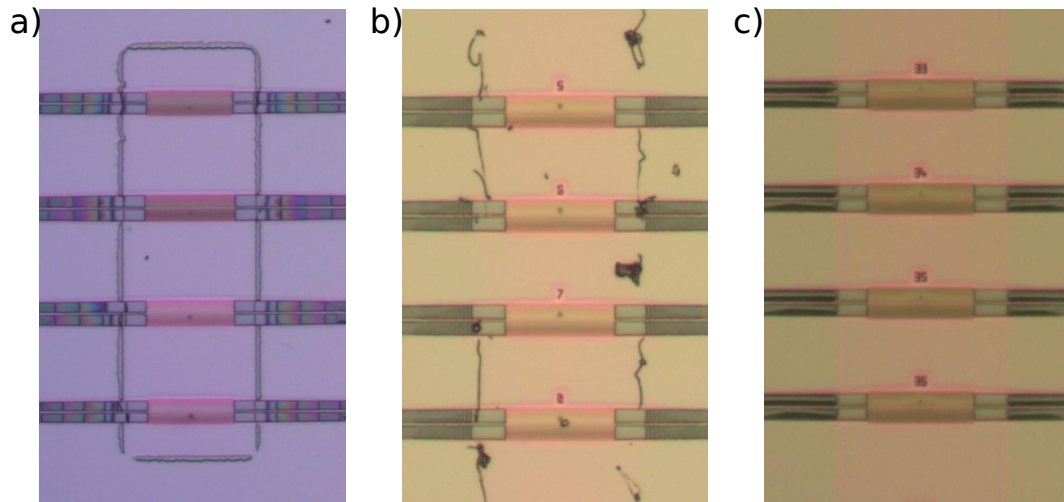


**Figure 2.16** – (a) and (b) Residues of AZ5214 observed after wet etching. (c) The formation of the residues was prevented by enhancing the soft-baking time and by carefully cleaning the Cr mask.

### 2.6.2 Cleaving and facets protection

Before suspending the PhC membrane, the sample is cleaved to allow the coupling between the lensed fibers and the waveguides (Fig. 2.1(d)). The sample is previously thinned to 250  $\mu\text{m}$  to facilitate this step, as for good optical coupling it is necessary to have facets as regular as possible. The cleaving can be performed using two techniques. A first method consists in using a manual scribe to engrave the silicon with a diamond tip. After engraving, the sample is attached to a glass coverslip with QS 135 and the cleaving marks are aligned to the edge of the glass coverslip under a long working distance microscope, as shown in Fig. 2.17. The cleaving is finally performed by applying an even pressure on the external part of the sample. If the applied pressure is not even, different cleaving lines can be created, resulting in not straight facets. In the worst case, the cleaving lines can be several hundreds of microns away from the desired position, leading to poor quality (or even impossible) coupling.

A second and more reliable method consists in using an automatic JBL cleaver. The sample is first attached on a stretched adhesive tape and mounted on the tool. The sample is then aligned and engraved with a diamond tip. The cleaving is finally automatically performed, with a blade hitting from the back the engraved lines while a plastic piece on top of the sample opposes the necessary pressure. However, this method also presents some difficulties due to the fact that the tool is optimized for larger samples, on the wafer scale.

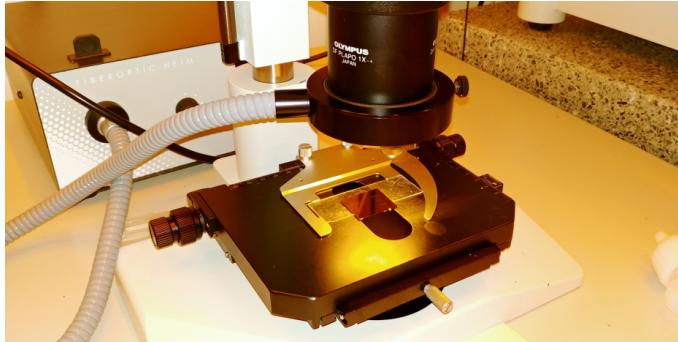


**Figure 2.17** – The sample is temporarily attached with QS135 on a glass coverslip, whose edge is aligned with respect to the cleaving marks under a long working distance binocular. The cleaving is performed by applying an even pressure on the external part of the sample

Not perfect cleaving was often observed and it can be explained by difficulties in applying an even pressure on the cleaved part but also by the presence of an angle between the crystalline axis and the cleaving marks. In fact, during ebeam writing (when the alignment marks are also written), the alignment is performed with respect to the sample edge, which is diced by CMI staff. An angle with respect to the crystalline axis in this step, added to the subsequent errors in alignment can cause a large discrepancy between the crystalline axis and the cleaving engravings. For the future, instead of diced substrates, cleaved ones will be used to reduce this error.

After cleaving, the facets of the sample need to be protected, to prevent the etching of the silica regions underlying the end of the waveguides. To this aim, QS135 is used: a thick layer of QS135 is melted on a glass coverslip and the sample facets are gently immersed in the wax. When removing the sample from the hotplate, the wax solidifies and protects the  $\text{SiO}_2$  layer from wet etching (Fig. 2.18).

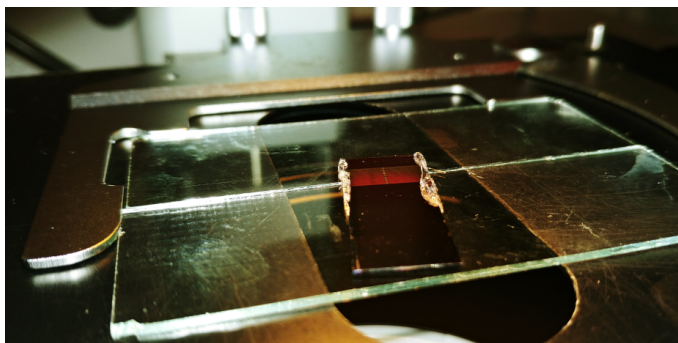


**Figure 2.18** – A layer of QS135 protects the facets from wet etching.



### 2.6.3 Membrane release

The membrane release is performed via wet etching in BHF, a technique widely used in microfabrication thanks to the high selectivity of HF in etching SiO<sub>2</sub> while not attacking Si at room temperature. However, the etching caused by HF is too fast to be properly controlled, so BHF is commonly employed: it consists in a mixture of HF and of a buffering agent, usually NH<sub>4</sub>F. In our case, Sigma-Aldrich®AF 875-125 solution is used. The sample is immersed for 30 minutes in the solution until the SiO<sub>2</sub> layer underlying the photonic crystals is fully etched. The sample is then rinsed in DI water for 10 minutes and later immersed in acetone to remove the resist and the QS135. Finally, it is rinsed with isopropanol and dried.

## 2.7 Anti-reflection coating

As mentioned before, the light is injected in the photonic crystal structures with lensed fibers in an end-fire setup. When recording the transmission spectrum, large oscillations in the signal are visible (Fig. 2.19) that are due to Fabry-Perot interferences caused by reflections at the facets. A first method used to reduce the interferences is to deposit an anti-reflection (AR) coating onto the facets (Fig. 2.1 (e)). In our case, the reflections considered are between silicon ( $n_{Si} = 3.48$  at 1550 nm) and air and the strategy is to deposit a quarter-wave layer with a refractive index of  $n_{AR} = \sqrt{n_{Si}} = 1.86$ . The target thickness is  $d = 208$  nm.

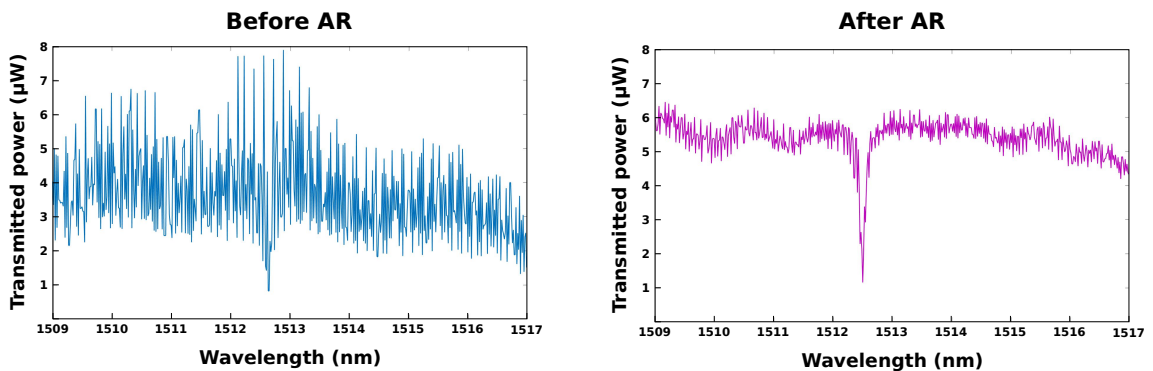


**Figure 2.19** – Transmission spectrum measured for the cavity m6\_12 before and after the deposition of an anti-reflection coating.

This step is performed by physical vapor deposition (PVD) with a Kenosistec Magnetron Sputtering system that allows for the deposition of dielectric thin films. In particular, the materials available are SiO<sub>2</sub>, TiO<sub>2</sub>, ZrO<sub>2</sub> and Ta<sub>2</sub>O<sub>5</sub> and to obtain  $n_{AR} = 1.86$  a mixture of SiO<sub>2</sub> and TiO<sub>2</sub> is used in a 58% and 42% proportion. This ratio is calculated considering  $n_{SiO_2} = 1.44$  and  $n_{TiO_2} = 2.45$  at 1550 nm.

A sputtering system, depicted in Fig. 2.20, schematically consists in a chamber under high vacuum ( $5 \cdot 10^{-3}$  mbar in our case) that includes an anode, where the substrate is placed, and a cathode, where the material to be sputtered (called “target”) is located. Argon plasma is

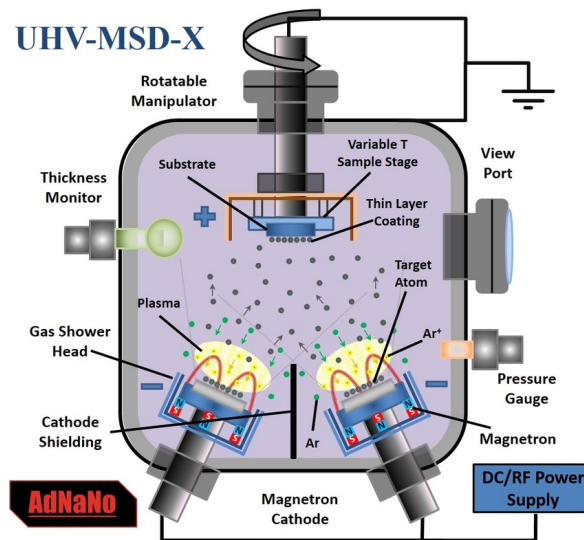


Figure 2.20 – Schematic representation of a magnetron sputtering system. Reprinted from [112].

created and the  $Ar^+$  ions are accelerated towards the target. Ion bombardment causes the ejection of some target atoms that subsequently deposit on the substrate surface forming a uniform film.

Plasma is ignited by applying a high voltage between the cathode and the anode, in RF configuration for insulating target materials. Plasma is initiated when some electrons with energy sufficient to ionize the Ar atoms (i.e. with  $E > 15.7$  eV) produce inelastic collisions resulting in the creation of a second electron and a positive ion. Both primary and secondary electrons are accelerated and can collide again with other Ar atoms in a cascade system resulting in the plasma creation. Moreover, for magnetron sputtering systems, strong magnets are present just behind the cathode: electrons are confined close to the target surface and this leads to a higher plasma density and hence to a larger sputtering rate. Furthermore, this configuration prevents substrate heating due to electronic collisions. To deposit the anti-reflection coating the procedure is as follows: the deposition rate of  $SiO_2$  and  $TiO_2$  is first determined individually. Secondly, the deposition rates have to be adapted in order to obtain the mixture of  $SiO_2$  and  $TiO_2$  in the 58%-42% proportion. As the deposition rate depends linearly on the power applied to the target [113], this is the parameter that is modified: the maximum power (200 W) is applied to the material with the lower deposition rate, usually  $TiO_2$ , and the other one is adjusted accordingly. Finally, the total deposition rate and the time necessary to obtain a 208 nm film thickness are calculated. Optical control of the deposited film is also possible with the Intellemetrics FilmDirector software available on the tool: the reflection of a beam with a wavelength of 1550 nm is monitored and it allows detecting when the  $\frac{\lambda}{4n}$  thickness is reached. The deposition rate of  $SiO_2$  and of  $TiO_2$  are determined by applying 200 W on the cathode for a fixed time, usually 10.000 seconds, and by measuring the thickness of the layer deposited on a silicon substrate. To obtain an accurate thickness measurement, the film is characterized optically with a Varian Cary 500 spectrophotometer. Absolute reflection

is measured from 200 to 2000 nm and the minima on the spectrum correspond to  $\frac{\lambda}{4n}$ ,  $\frac{3\lambda}{4n}$ ,  $\frac{5\lambda}{4n}$ , ... The spectra showed in Fig. 2.21 allowed to calculate film thicknesses of 360 nm for SiO<sub>2</sub> and of 180 nm for TiO<sub>2</sub>. Those thicknesses were confirmed also by ellipsometric measurements.

The reflection spectrum of the AR coating deposited after this calibration is also shown in Fig. 2.21. A minimum in the desired spectral region (around 1550 nm) is visible.

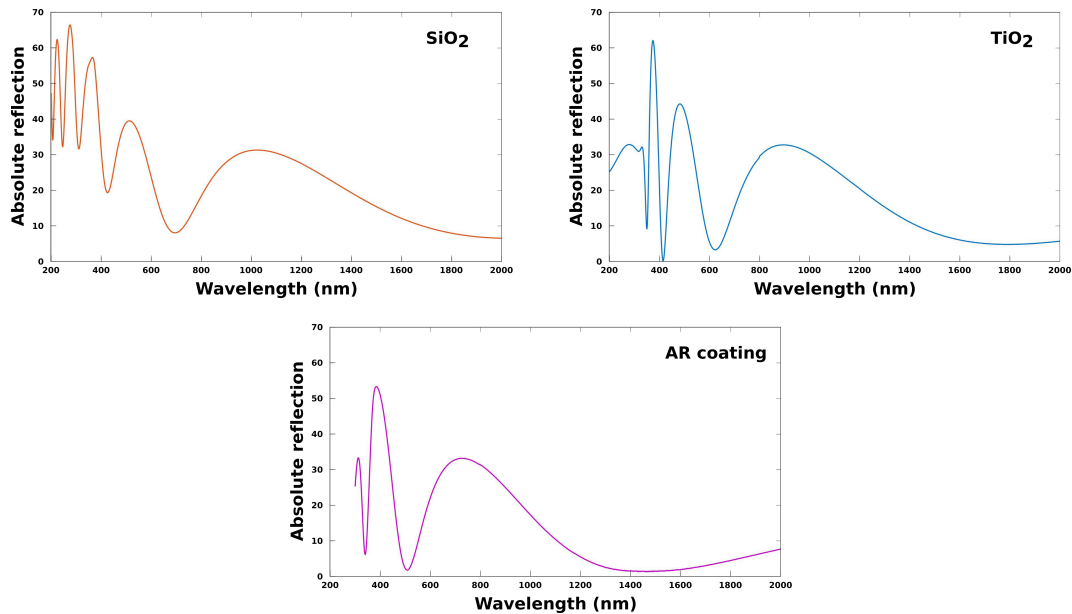


**Figure 2.21** – Absolute reflection spectra measured for 10000 s of SiO<sub>2</sub> and TiO<sub>2</sub> deposition and for the anti-reflection film consisting in a mixture of SiO<sub>2</sub> and TiO<sub>2</sub>. In this latter case, a minimum in the zone of interest, around 1550 nm, is observed.

## 2.8 SU8 mode adaptors

Another strategy to avoid the reflections at the interfaces and to increase the coupling efficiency is to use inverse tapers instead of cleaved waveguides terminations. This approach consists in tapering the waveguide close to the facet and embedding it either in SU8 or in SiO<sub>2</sub>, as showed in Fig. 2.22.

SU8 is an epoxy-based negative resist. It is sensitive to the i-line (365 nm) and it is commonly used for high aspect-ratio permanent structures because when it is cross-linked it is very difficult to remove it. On the optical properties, SU8 has a refractive index of 1.58 at 1550 nm and it is thus suitable to fabricate waveguides in the spectral region of interest, that can act as mode adaptors between the tapered waveguides and the input and output fibers in the end-fire configuration: in fact,  $n_{\text{SU8}}$  is comprised between the  $n_{\text{SiO}_2}$  and  $n_{\text{Si}}$ . Moreover, the possibility to create layers going from few microns to tenths (and even hundreds) of microns permits to create waveguides with dimensions adapted to the spot sizes of the optical fibers used for light injection and collection. Two types of waveguides were fabricated, featuring a

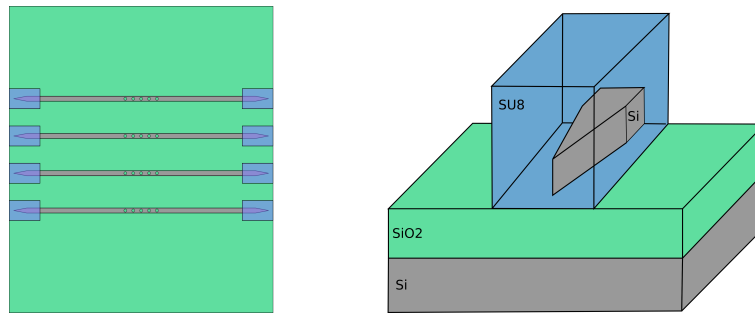


**Figure 2.22** – Schematic drawing of the top and side view of tapered waveguides terminations embedded in SU8 mode adaptors.

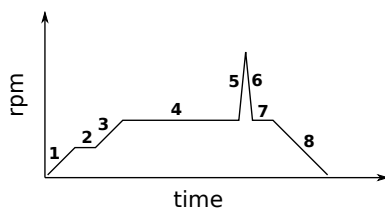


**Figure 2.23** – Schematic representation of the SU8 spin steps.

Step	4 $\mu\text{m}$		10 $\mu\text{m}$	
	Time (s)	rpm	Time (s)	rpm
1	5	500	5	500
2	5	500	5	500
3	54	5942	17	2187
4	40	5942	40	2187
5	1	6000	1	3187
6	1	5942	1	2187
7	5	5942	5	2187
8	60	0	22	0

**Table 2.2** – SU8 spin steps parameters.

cross section of  $4\ \mu\text{m} \times 4\ \mu\text{m}$  and  $10\ \mu\text{m} \times 10\ \mu\text{m}$ , to adapt respectively to lensed fibers and to cleaved single mode fibers.

The fabrication of SU8 mode adaptors is performed between the ICP etching and the membrane release. After cleaning the sample surface with acetone and isopropanol, the sample is put for 1 minute at  $115\ ^\circ\text{C}$  to evaporate solvents and ensure better resist adhesion. SU8 (Gersteltec GM1060) is then spin-coated with a Sawatec coater following the spin steps showed in Fig. 2.23, to obtain either  $4$  or  $10\ \mu\text{m}$  thick layers. The sample is then let to rest on a flat surface for 10 minutes and subsequently it undergoes a softbake process. This step is the most crucial to obtain good quality waveguides: in fact, especially for thick layers, a too fast evaporation of solvents can lead to the formation of stress and subsequent cracks in the film. To ensure a gentle solvent evaporation, the softbake is performed with a programmable Sawatec hotplate: the temperature is increased from room temperature to  $95\ ^\circ\text{C}$  in 30 minutes, then the sample is let for 5 minutes at  $95\ ^\circ\text{C}$  and finally the temperature is decreased to room temperature in 30 minutes. Exposure to UV is performed with the Suss MA6 mask aligner. The exposure times are  $6.2\ \text{s}$  for the  $4\ \mu\text{m}$  layer (to deliver a dose of  $128\ \mu\text{C}/\text{cm}^2$ ) and  $8.3\ \text{s}$  for the  $10\ \mu\text{m}$  layer (to deliver a dose of  $166\ \mu\text{C}/\text{cm}^2$ ). After exposure, the sample is let to room temperature for 30 minutes and finally hard-baked for 15 minutes at  $95\ ^\circ\text{C}$ . The same temperature ramps as for the soft bake are used. Finally, the resist is developed in PGMEA (propylene glycol monomethyl ether

acetate) for 2 minutes, rinsed in de-ionized water and blow-dried. Fig. 2.24 shows SU8 mode adaptors on top of silicon tapered waveguides.

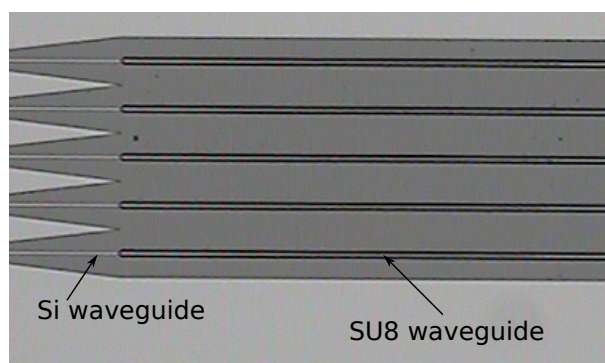


**Figure 2.24** – 4  $\mu\text{m}$  SU8 mode adaptors on top of tapered waveguides.

## 2.9 Microfluidic layers

As mentioned in the introduction, the platform discussed in this thesis belongs to the group of optofluidics systems: the photonic chip is integrated with microfluidic layers that allow for performing experiments in aqueous environment, with particles or bacteria suspended in liquid.

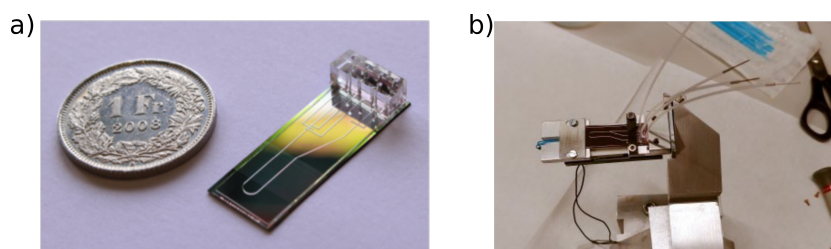


**Figure 2.25** – (a) Picture of one of the optofluidic chips used during this thesis (From Ref. [105]). (b) The same chip connected to injection tubes and mounted on the sample holder.

The microfluidic layers consist in a PDMS layer covered by a glass coverslip (Fig. 2.26). Moreover, a 3 mm thick PDMS block allows for the connection with tubes, as shown in Fig. 2.25. This connection permits the injection of liquids for particles and bacteria transport and of compressed air for flux control.

The PDMS layer is fabricated with soft-lithography techniques, introduced by Whitesides' group in 1998 [102]: a master mold is first created using a photoresist (AZ9260 in our case) on a silicon wafer, liquid PDMS is then spin-coated onto the surface and after curing it is peeled off and the membrane containing the desired channels is obtained. The glass layer, on the other hand, is obtained by directly etching channels with an excimer laser in a borosilicate coverslip. Finally, the layers are aligned with the help of a mask aligner and bonded together to obtain the final chip. More details on the fabrication steps will be given in next sections.

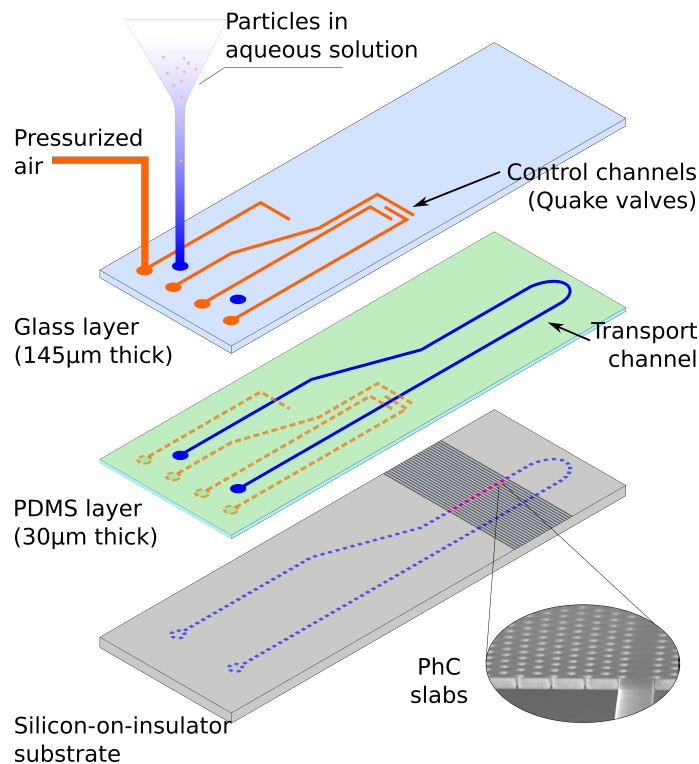


**Figure 2.26** – Exploded vision of the microfluidic layers. A PDMS layer placed directly on top of the photonic chip allows for particles and bacteria transport in aqueous solution, while channels etched in the glass coverslip allow for flux control.

During the thesis, three configurations were used. They are illustrated in Fig. 2.27 and consist in two microfluidic systems, featuring one and two injection channels respectively, and in a "swimming pool" configuration obtained by simply placing a PDMS frame onto the photonic structures.

### Single channel

At first, a single channel system was used [114, 115]: a 200 μm wide and 10 μm thick channel is created in a 30 μm PDMS membrane. The photonic crystal structures lie under the channel and the particles passing nearby the cavity region can interact with the confined electromagnetic field. In addition, a 145 μm thick borosilicate coverslip (Schott D263) is placed on top of the PDMS layer to allow for flux control: channels are etched in it and by injecting compressed air Quake valves [99] are created (Fig. 2.28).

The main advantage in using glass as the outer layer resides in the fact that it guarantees at the same time strong mechanical stability and very good optical properties: as the sample is fabricated to be used with an oil-immersion microscope objective. Such types of objectives are designed to be used with a glass coverslip, usually 170 μm thick, between the specimen to inspect and the objective: aberrations given by the immersion oil and by the glass coverslip

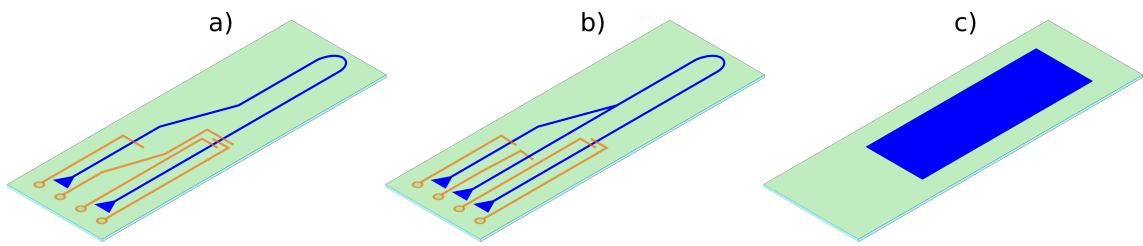


**Figure 2.27** – The three microfluidic configurations used: (a) a single transport channel for particles or bacteria, (b) two injection channels and (c) the "swimming-pool" configuration.

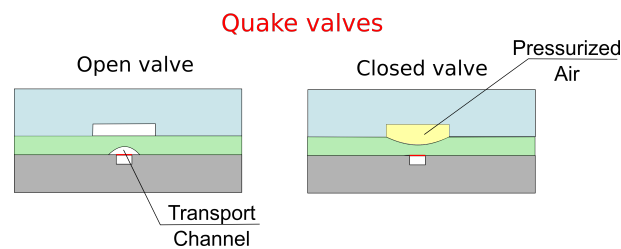


**Figure 2.28** – Illustration of the working principle of a Quake valve: compressed air injected on top of a channel deforms the PDMS, hence closing the channel.

are considered and corrected in the design. In our case, the sum of the PDMS and of the glass layers thicknesses mimicks regular glass coverslips and gives excellent optical properties [85, 105]. Moreover, a peristaltic pump formed by three glass channels is also present.

### Double injection channel

During the thesis, two main modifications to the microfluidics were performed:

- The transport channel thickness was increased from  $10\ \mu\text{m}$  to  $20\ \mu\text{m}$  to take into account the larger size of bacteria ( $1 \times 2\text{-}6\ \mu\text{m}$  typically) with respect to nanoparticles (max  $500\ \text{nm}$  in diameter) previously used. In particular, this variation was implemented to reduce the risk of having bacteria stuck into the channels. The membrane thickness was also augmented by  $10\ \mu\text{m}$  to keep the same amount of PDMS on top of the channel. Unfortunately, this configuration showed to be more fragile than the previous one and the PDMS often broke under the compressed air, resulting in the creation of air bubbles into the channels. Moreover, bacteria showed to stuck onto the silicon substrate and in the metallic tubes used to connect teflon ones. This caused the necessity to use larger pressures to activate the Quake valves, that eventually lead to the PDMS membrane breaking. A solution will consist in depositing a BSA (Bovine Serum Albumine) layer in the channels to prevent bacterial adhesion.
- An injection channel was also added, to allow the rapid switch between liquids, on the order of few seconds. The flux in each of the two channels is controlled independently and a switch without mixing of the two liquids is obtained thanks to the laminar nature



## Chapter 2. Fabrication

---

of the microfluidic flux. In Fig. 2.29 the switch between red and blue liquids is shown. For better clarity, a glass substrate was used instead of a silicon one. This solution was implemented with the purpose of trapping a bacterium and subsequently sending an antibiotic on it to study its effects in real time.

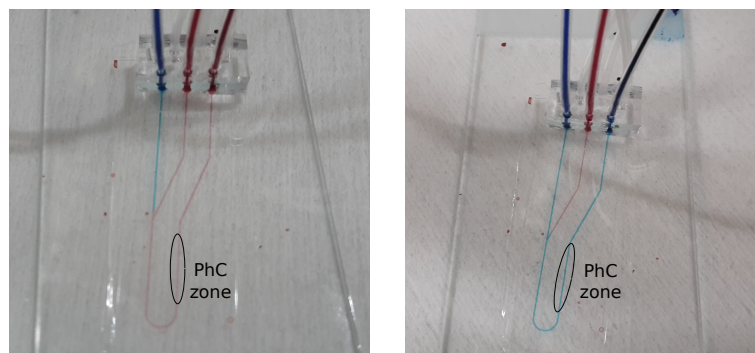


**Figure 2.29** – Microfluidic layers allowing the switch between red and blue liquids. The laminar nature of the microfluidic flux allows for a switch without mixing.

### ”Swimming pool“

Finally, a static system was used, consisting simply in a 100  $\mu\text{m}$  PDMS frame containing a drop of liquid and covered by a glass coverslip to avoid evaporation. This configuration was first used during experiments in CEA Grenoble, because their setup does not allow for flux control. Subsequently, it was used here at EPFL as well, in the case of breaking of the microfluidic layers.

## 2.10 PDMS mold

The first step is the fabrication of the master mold on a 4 inches silicon wafer (Fig. 2.30). The wafer surface is prepared by cleaning it with acetone and isopropanol, followed by an oxygen plasma treatment performed for 1 minute at 60 W and 60 Torr. After applying a HDMS adhesion promoter layer as for the AZ5214 resist, a 10  $\mu\text{m}$  layer of AZ9260 is spin-coated on the wafer, for 60 seconds at 1800 rpm. The wafer is then baked for 200 seconds at 115  $^{\circ}\text{C}$ . AZ9260 is a positive resist with a photoinitiator based on DNQ-sulphonates, that require a minimum concentration of water of a few per thousand for the photoreaction: the sample is thus let 30 minutes to rehydrate before the exposure. This is performed with a MJB3 mask aligner for 80 seconds (to deliver a dose of 2100  $\text{mJ}/\text{cm}^2$ ). The resist is then developed in AZ400K diluted with de-ionized water in a 1:4 ratio for 6 minutes to remove the resist regions degraded by UV exposure and finally it is rinsed with water and blow-dried.

A very final step consists in baking the mold for 90 minutes at 115  $^{\circ}\text{C}$ . This step is referred to as “reflow” and consists in rounding of the photoresist structures (Fig. 2.31). This phenomenon is desirable for microfluidic channels fabrication for two reasons: first, the absence of sharp



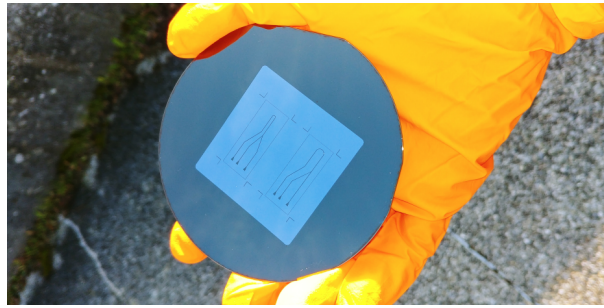


**Figure 2.30** – A mold used for the fabrication of two PDMS membranes.

edges leads to a smaller chance for particles and bacteria to stuck onto the PDMS surface. Secondly, the force applied by the compressed air of Quake valves is better distributed for rounded surfaces than for squared ones, resulting in a larger robustness of rounded channels.

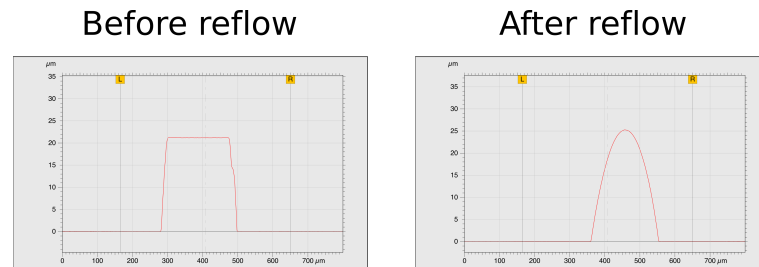


**Figure 2.31** – Channel profile measured before and after resist reflow.

To obtain 20  $\mu\text{m}$  thick channels, two layers were deposited. The soft-baking time was increased to 400 seconds and the exposure time was augmented to 150 seconds. The reflow was performed in the same way, but temperature ramps were used during the heating from room temperature to 150  $^{\circ}\text{C}$  and during the cooling down to prevent cracks that can easily happen in such a thick resist.

## 2.11 PDMS membrane

The PDMS membrane is created in the dedicated CMi PDMS line. The first step is the silanization of the surface, to reduce the PDMS adhesion to the substrate and hence to facilitate the final de-molding. This can be achieved by exposing the mold to Trimethylchlorosilane (TMCS) vapours for 15 minutes.

In the meantime, a mixture of 10 g of PDMS base and 1 g of curing agent is prepared and inserted in a Thinky Mixer. Mixing is performed for 1 minute at 2000 rpm and defoaming for 2 minutes at 2200 rpm. Subsequently, PDMS is spin-coated onto the wafer for 40 seconds. 2000 rpm are used to obtain a 30  $\mu\text{m}$  layer (in the case of molds featuring 10  $\mu\text{m}$  thick channels), while 1551 rpm are used to obtain 40  $\mu\text{m}$  layers (in the case of 20  $\mu\text{m}$  thick channels). After coating, the wafer is let 5 minutes on a flat surface to obtain a better thickness uniformity,

## Chapter 2. Fabrication

---

especially at the edges, and finally it is set for 80 minutes at 80 °C to accelerate the cross-linking reaction. Once the PDMS is cured, it is stable and can be stored for months.

Finally, a thick PDMS block is fabricated. It is used to connect the tubes necessary to inject liquids in the transport channels, as well as the compressed air in the control channels. In this case, a silicon wafer is used as a base. A frame is created with aluminum foil and the PDMS is simply poured into the frame to obtain a 3 mm thick layer. In this step, bubbles often appear, that can be eliminated by letting the wafer for 2 hours in a vacuum dessicator. Large bubbles can also be removed using a pipette. When the PDMS layer is completely defoamed, it is cured for 80 minutes at 80 °C, as for the membrane.

### 2.12 Glass layer

The starting material to create the glass microfluidic layer is a borosilicate 4" wafer that is diced in 1x3 cm rectangles. Microfluidic channels are then created by direct etching with an OPTEC LSV3 excimer laser. Excimer lasers exploit the UV radiation that is created by the decaying of an excimer formed by a noble gas and a halogen (in our case ArF), both added in a neon buffer gas.

Excimer lasers have a broad spatial profile, so most of the processing is performed using projection optics: the beam illuminates a mask, whose demagnified image is focused onto the substrate to be etched. The masks used are listed in Tab. 2.3.

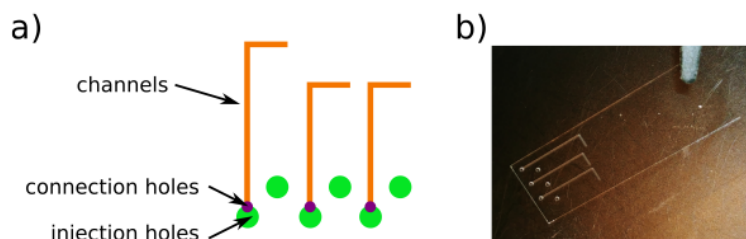


**Figure 2.32** – (a) Glass channels layout. (b) A glass layer ready to be placed on top of the optofluidic chip.

The pattern is created with a CAD software (Autodesk AutoCAD) and it is represented in Fig. 2.32. Three elements are present: channels, holes to allow the injection of air and water in the corresponding channels and “connection holes” to create a smooth connection between the injection holes and the channels. The depths of those elements, together with the writing parameters (frequency, power, number of shots, mask) are listed in table 2.3.

One aspect to take into account is the fact that, while etching, the high power of the excimer laser also causes melting of the glass. This results in undesired melted material residues at the edges of the channels and of the holes that could lead to a decrease of the adhesion of the PDMS layer to the glass one. To minimize this inconvenience an energy of 2.5mJ was selected and the structures were written in the following order: injection holes-connection holes-

Structure	Depth	Mask	Frequency	Number of shots
Channels	10 $\mu\text{m}$	Square 200 $\mu\text{m}$	200 Hz	500
Connection holes	20 $\mu\text{m}$	Square 100 $\mu\text{m}$	200 Hz	800
Injection holes	145 $\mu\text{m}$	Circle 100 $\mu\text{m}$	200 Hz	3000

**Table 2.3** – Optec LSV3 parameters used during this thesis.

channels to avoid the filling of the channels with melted material. Moreover, the melted glass can be removed by mechanical polishing using a cleanroom paper wetted with isopropanol. In Fig. 2.33 the cross sections of the channels are measured with the Alpha Stepper profilometer before and after polishing. After polishing, the glass structures present at the edges of the channels are completely removed.

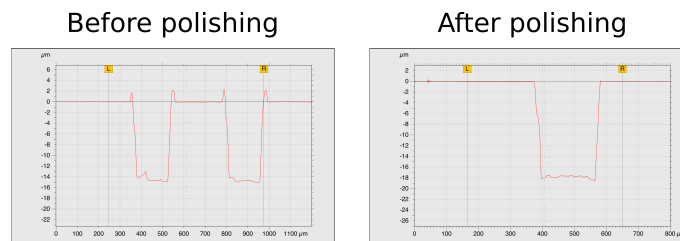


**Figure 2.33** – Channels profiles before and after polishing. Before polishing, a glass structure, more than 2  $\mu\text{m}$  thick, is present at the edge of the channels.

## 2.13 Microfluidic layers assembly

Once all the layers are fabricated, they need to be placed one on top of the other and on top of the photonic chip.

At first, the glass coverslip is cleaned in acetone and isopropanol, blow-dried and attached to a glass mask suitable to be used with a mask aligner, with the channels facing upwards. In our case, an old Cr mask used for previous PDMS mold fabrication is employed. The PDMS membrane is then demolded: it is cut with a scalpel, gently lifted from the mold and transferred onto a metallic support. Holes (750  $\mu\text{m}$  in diameter) are drilled in correspondence to the injection circles with the help of a puncher and the membrane is finally moved on top of the glass layer. In this operation, particular attention needs to be paid in centering the PDMS and the glass holes, to ensure a good liquid transfer. It is then necessary to stretch out the PDMS membrane so that no bubbles are created between it and the glass layer: a perfect adhesion between the two layers is indeed crucial for the functioning of the device. If a conformal contact between the PDMS/glass and the PDMS/silicon interfaces is obtained, Van der Waals forces permit the injection of liquids with a pressure up to 0.35 bar. This pressure is much larger than the ones usually used for optical trapping experiments and this bonding technique has the advantage of being reversible. The microfluidic layers can be removed in the case of breaking of the PDMS membrane and the photonic chip can be used in the "swimming

pool“ configuration.

Finally, a MJB3 mask aligner is used to align the injection channel with respect to the photonic crystals. A MJB3 mask aligner is used because of the fact that it is a manual mask aligner: it permits to manually move the silicon chip close to the microfluidics layer until they get in contact. Most of the more recent mask aligners, on the contrary, at the very beginning perform a WEC (Wedge Error Compensation) procedure, that requires the substrate to be put in contact with the mask. In this case, this is undesirable because as soon as the PDMS gets in contact with the silicon surface the Van der Waals bonding is created and no alignment is possible.

Once the three thin layers are assembled, the last step consists in bonding the thick PDMS block that allows for the connection with tubes. The block is first cut with a scalpel and injection holes are drilled utilizing a puncher with the help of a plexiglass mask. In this case, Van der Waals forces are not sufficient to ensure the sealing of the connection, so a plasma activation of the PDMS and of the glass surfaces is performed [116]. The block is then simply put onto the glass layer under a long working distance binocular and permanent bonding is obtained.

## 3 Experimental setup and characterisation

The basic experimental setup consists in an optical setup for samples characterization and for particles optical trapping, together with a system to control the flux in the optofluidic chip. This setup, together with the modifications implemented during this thesis, will be detailed.

Mainly, the modifications consisted in adapting the experimental setup for bacteria trapping: a station to culture and store bacteria was created and the sample holder was integrated with a Peltier module to allow for working at different temperatures (from room temperature to the pasteurization ones, passing by 37 °C, the optimal temperature for bacterial growth). Moreover, the sample holder mechanical stability was increased, allowing for longer coupling times between lensed fibers and optical waveguides.

In addition, the optical setup used for experiments in Grenoble will also be presented.

Finally, the experimental procedure will be discussed, together with the optical characterisation of the fabricated samples.

### 3.1 Preexisting setup

#### 3.1.1 Optical setup

The optical setup, schematically depicted in Fig. 3.1, can be divided in several parts. The core one consists in an end-fire arrangement, with the optofluidic chip mounted vertically on an adapted sample holder and lensed fibers to inject and to collect light (Fig. 3.2). On top of the sample, a microscope objective provides access to the surface for three optical lines: an illumination line, a visible imaging one and an IR one. More details on the conception and implementation of the setup can be found in Ref. [114] and [85].

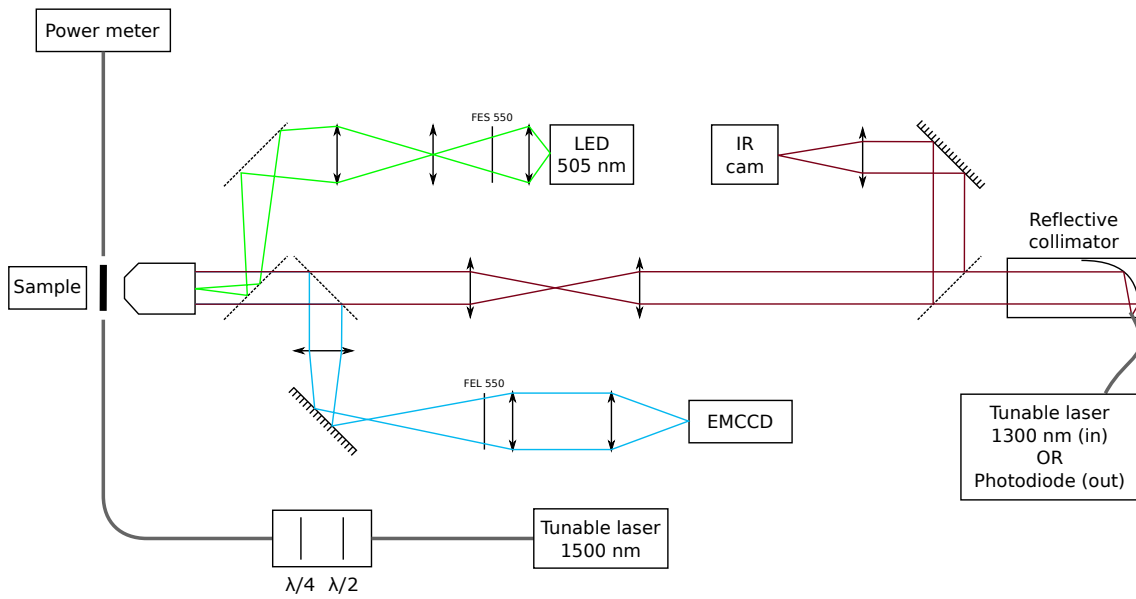


Figure 3.1 – Schematic representation on the preexisting experimental optical setup.

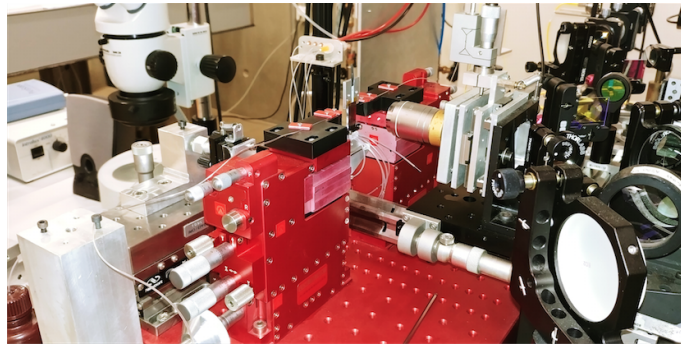


Figure 3.2 – Detail of the sample region in an end-fire arrangement. Light is injected and collected with lensed fibers and a microscope objective provides access to the sample surface.

### End-fire arrangement

In the end-fire arrangement, a custom made sample holder is used for the optofluidic chip: it allows for precise x,y and z translation as well as for tilt and rotation control, to ensure that the facets of the sample are perpendicular to the optical fibers and hence to permit maximum coupling.

Light from a tunable laser (Yenista Tunics Plus) is injected into the sample waveguides through a lensed fiber (Nanonics). The laser can provide beams with wavelengths comprised between 1470 and 1620 nm and with powers comprised between 0.2 and 10 mW. The lensed fibers feature a spot size of  $2\mu\text{m}$  and a working distance of  $6\mu\text{m}$ . Precise polarization control is ensured by the use of polarisation maintaining fibers and by a unit consisting in a  $\lambda/2$ - $\lambda/4$  waveplate configuration.

After being transmitted through the sample waveguides, the light is also collected by a lensed fiber and the intensity is monitored with a power meter (Newport 842A). Moreover, a digital acquisition card (National Instruments USB 6009) and a dedicated LabVIEW program allow for automated wavelength scan and transmission recording.

#### **Illumination line**

Illumination over the sample surface is provided by a 505 nm LED (Thorlabs M505L3) and a Köhler configuration is used to ensure illumination homogeneity.

The optical setup was first built with the objective of trapping nanoparticles. In particular, fluorescent polystyrene nanospheres (100 to 500 nm in diameter) absorbing in the green part of the spectrum were used and the LED wavelength was selected to allow, at the same time, for illumination and for fluorescence excitation.

#### **Visible imaging line**

Sample imaging is performed with a EMCCD (Hamamatsu ImagEM 512), which is suspended on the optical bench to reduce vibrations. To enhance the visibility of fluorescent nanospheres, a couple of filters is used. A short pass filter at 550 nm is used on the illumination line, while a long pass one at 550 nm is used on the imaging line. In this way, most of the excitation light is filtered and the particles brightness is enhanced. A large contrast and a detector with high sensitivity are important especially in the case of smaller nanoparticles: indeed, the concentration of fluorophores scales with the volume of the nanoparticles and it results in the 100 nm particles being 125 times less bright than the 500 nm ones.

#### **IR line**

The IR line, coloured in dark red in Fig. 3.1, has multiple functions.

First, an IR camera (Sensors Unlimited) allows for the imaging of the light scattered from the sample surface. In particular, the surface emission of the cavity mode is monitored and it permits to easily identify the resonance wavelength.

Secondly, a quantitative analysis of the surface emission of this mode can be performed thanks to a reflective collimator (Thorlabs RC08APC-P01): the collimated beam collected by the microscope objective is focused at the entrance of an optical fiber and its intensity is measured by a photodiode.

Finally, the same collimator can be used in the reverse direction and allows for the creation of auxiliary optical tweezers. A beam from a tunable laser around 1300 nm (Tunics Plus) is expanded and collimated. It is then focused onto the sample surface by a high numerical aperture objective (Leica HCX PL APO, oil immersion, NA=1.4) and acts as standard optical

### Chapter 3. Experimental setup and characterisation

tweezers. This configuration is mainly used to accelerate experiments: in fact, submicron nanoparticles suspended in water undergo Brownian motion and a long time can be necessary before a particle is found in the vicinity of the optical cavity region (on the order of tenths of minutes). Moreover, low particle concentrations are often used to prevent multiple trapping events and to study the response of singularly trapped nanospheres, hence increasing even more the waiting time. Auxiliary optical tweezers permit to collect particles in a  $30 \mu\text{m}^2$  area around the cavity and to subsequently move them to the cavity. This arrangement reduces the time necessary to trap a new particle to few seconds.

#### Additional equipment

Besides the basic optical setup, that allows for performing optical trapping experiments and optical characterization of the photonic crystal cavities, for certain applications some additional equipment is required.

As we will see in section 4.2, the main effect of a trapped object onto the cavity mode is a redshift of the resonance frequency, due to a variation in the refractive index surrounding the optical cavity. To quantify this shift, two lasers can be used in the following configuration, depicted in Fig. 3.3: one laser is set at the resonance frequency and it is responsible for the optical trapping, while the other one is used to perform a wavelength scan around the resonance frequency and it allows for recording the transmission spectrum of the device, in presence or in absence of a trapped object.

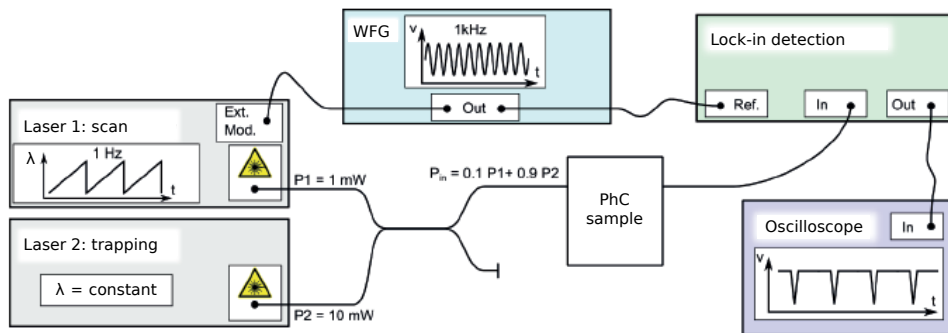


**Figure 3.3** – Schematic representation of the setup used for simultaneous particle trapping and  $\lambda$  scanning. Two lasers are injected in the sample waveguides with a 90:10 coupler. The one responsible for scanning is modulated with a waveform generator and its corresponding signal is detected with a lock-in. Picture adapted from Ref. [85].

Both lasers are injected in the access waveguide at the same time through a 90:10 fiber coupler. The first one, connected to the port allowing for 90% of transmission, is fixed at the cavity resonance frequency and its output power is set at a value sufficient for optically trap nanoparticles (usually in the 8-10 mW range). The other one, on the contrary, is used as a probe and it is set to periodically scan a 10 nm spectral range around the resonance frequency. To ensure that it does not alter the cavity response, it is connected to the port providing 10%



of transmission and a low output power (1 mW) is used.

To detect such a small signal with respect to the trapping one, a lock-in amplifier is used (Stanford SR510). The laser signal is modulated at a frequency of 10 KHz with an external waveform generator (WFG on the figure), that also provides the reference for the lock-in detection, and the signal is finally recorded with an oscilloscope.

### 3.1.2 Microfluidics control

The sample is equipped with a 3 mm thick PDMS block to allow for connection with tubes for fluids injection and for flux control. It features six ports (Fig. 3.4 (a)): two for fluids (input and output), connected to the channel created in the PDMS membrane, and four ports connected to glass channels for flux control by means of the Quake valves described in Fig. 2.28.

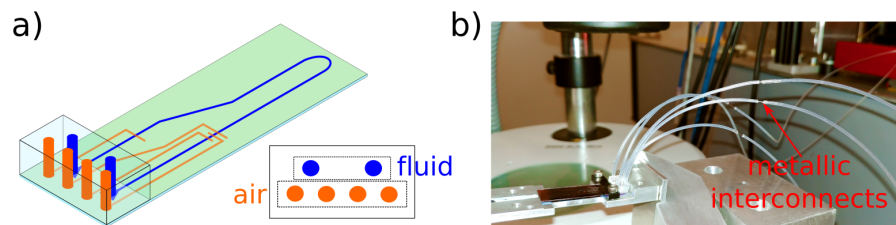


**Figure 3.4** – a) Schematic representation of the connection ports. (b) Sample connected to the microfluidic tubes.

A pressure source derived from the nitrogen evaporation circuit of the Physics department is used for both liquid and control systems and it is distributed over three pressure regulators (Bellofram, Type 10), as shown in Fig. 3.5: the first one regulates the flux speed, and it can be actuated with the manual valve highlighted in red in Fig. 3.5. Contrarily, the other regulators set the pressure injected in the control channels, that are actuated by solenoids. The compressed air is input in a set of solenoid valves (Telemecanique PS1E23) and an in-house electronic board with a DAQ (National Instruments USB 6009) allows for controlling the opening and closing of the valves with a LABVIEW routine.

The sample mounted on the sample holder and connected to the tubes is showed in Fig. 3.4 (b). Polyethylene Tubes (Intramedic, no. 427406) with inner diameter of  $380\mu\text{m}$  and outer diameter of  $1090\mu\text{m}$  are used. The total tube length is 60 cm but, to facilitate the connection with the sample, stainless steel interconnects are used (Unimed 200.010-A). In fact, it is necessary to note that the holes in the PDMS block have a diameter of  $750\mu\text{m}$  and that to insert the tubes it is thus necessary to deform them slightly. This is an easy operation when the sample is horizontally mounted on its support, but it gets difficult when the sample is vertically placed and possibly coupled with waveguides. The interconnects provide the advantage of permitting an easy and fast connection of the tubes, for instance when it is necessary to change fluid during an experiment.

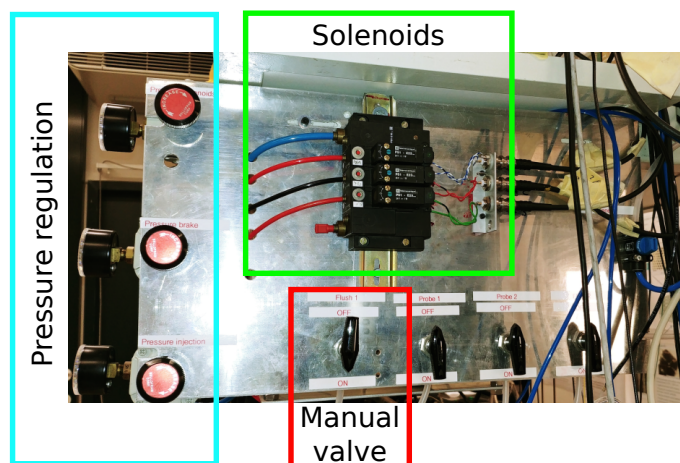


Figure 3.5 – Control panel for the microfluidic channels.

### 3.2 Modified setup

During this thesis, some modifications to the experimental setup were implemented to make use of the developed “two-channels microfluidics” and to permit bacteria manipulation. In particular, the main objective of those modifications was enabling experiments involving bacteria and antibiotic agents (high temperatures, antibiotics, UV radiation). The final purpose was to trap a single bacterium and to study its response to antibiotics but unfortunately the available time was not sufficient to achieve this objective. In this section, the details of the modified experimental setup are presented.

#### 3.2.1 Optical setup

The main modifications to the optical setup are as follows and they will be subsequently detailed:

- A 420 nm illumination line was added (Fig. 3.7), to allow for the use of two different fluorescent nanoparticles at the same time (absorbing in the green and in the violet respectively).
- The sample holder was modified to obtain larger mechanical stability and hence longer coupling times with the lensed fibers. Moreover a Peltier module was added to control the temperature during trapping experiments.

#### Second illumination line

The two injection channels created in the PDMS membrane allow for a rapid switch between liquids. Experiments with two kind of particles can thus be carried out at the same time. To this aim, we selected nanoparticles (Fischer Scientific) featuring different sizes, 100 to 500 nm,

and different fluorophores, green and red.

Particles close in size were chosen with different fluorophores to easily recognize them. The absorption and emission spectra are shown in Fig. 3.6 (a). To excite the red particles, the already present 505 nm LED was used, while to excite the green ones a second illumination line was added. A 420 nm LED was chosen (Thorlabs M420L3), which spectrum is showed in Fig. 3.6 (b) and the same Köhler configuration was implemented. The final optical setup is represented in Fig. 3.7.

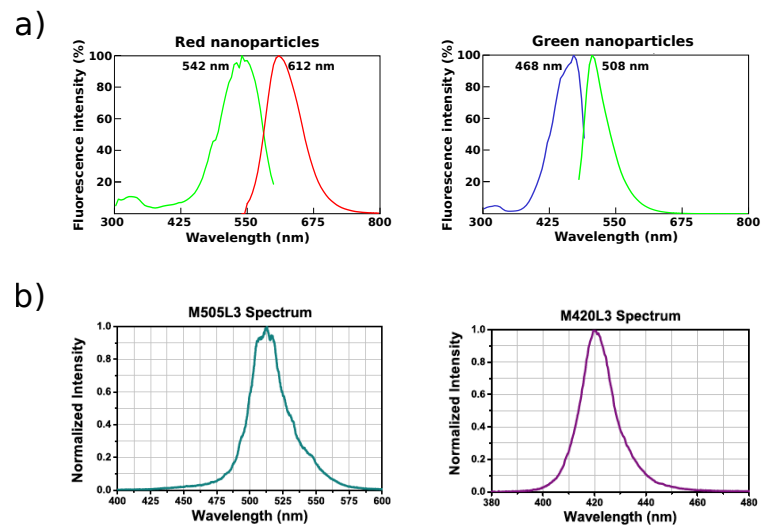


**Figure 3.6** – (a) Absorption and emission spectra of the two kind of fluorescent particles used. (b) Emission spectra of the 505 nm and of the 420 nm LED.

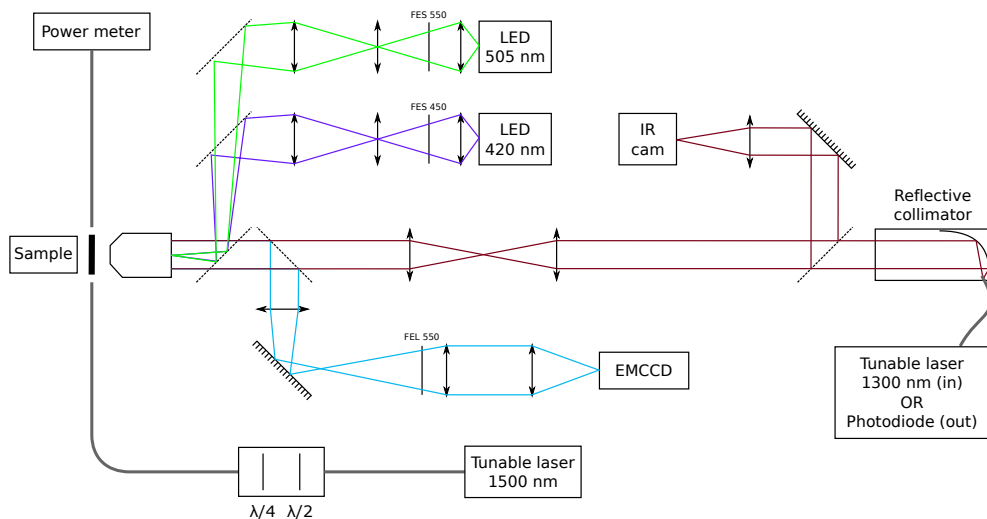


**Figure 3.7** – Modified optical setup.

### Sample holder

For optical trapping experiments it is important to have a stable coupling between the lensed fibers and the waveguides. On previous setup, good coupling was obtained for a maximum of 10 minutes, which was sufficient for particles trapping. Indeed, for optical trapping experiments assisted by auxiliary optical tweezers, few minutes are sufficient and few seconds of trapping already contain all the information on the trapped object.

Nevertheless, if auxiliary optical tweezers are not used, and depending on the concentration of the objects under study, a longer time (up to few tenths of minutes) can be necessary before particles or bacteria that undergo Brownian motion can reach the cavity region. A long coupling time between fibers and waveguides is thus desirable to ensure the correct cavity excitation.

The main difficulties in obtaining a long mechanical stability reside in the fact that the sample is mounted vertically and that the attached tubes have the tendency to pull and detach it from the sample holder, as schematically represented in Fig. 3.8 (a). To increase the sample stability, the sample holder was modified as shown in Fig. 3.8 (b). A groove, 250  $\mu\text{m}$  deep, was created as the lying surface for the sample. A Delrin<sup>®</sup> (Polyoxymethylene) strip keeps the sample in place, rigidly but not too much, to avoid breaking of the thin glass coverslip. On the other side, a metallic clamp placed on top of the sample ensures that the sample will not detach from the surface.

Finally, a more rigid connection between the sample holder and its support was provided with the help of the staff of the mechanical workshop. Those modifications allowed to obtain stable coupling for more than 40 minutes.

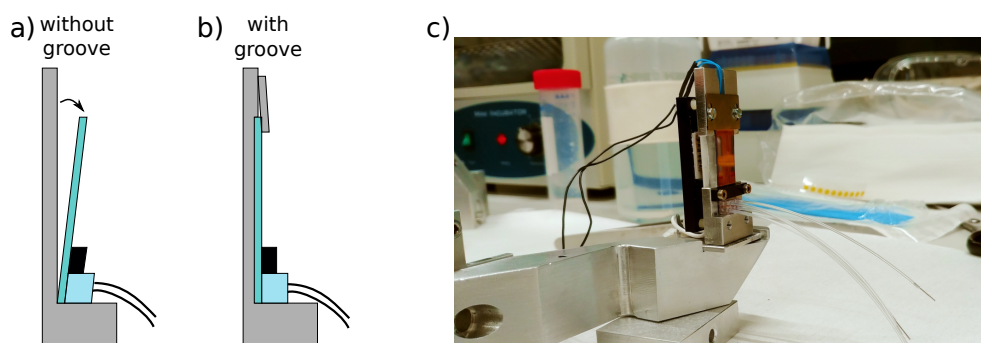


**Figure 3.8** – (a) Schematic drawing of the previous sample holder. (b) Sample holder modified with a groove. (c) Picture of a sample mounted on the sample holder.

Besides improving the sample mechanical stability, we considered the possibility of controlling the sample temperature important for optical trapping experiments involving living bacteria. In particular, the possibility of studying bacteria at 37  $^{\circ}\text{C}$  is meaningful to compare the results obtained by optical trapping with the ones obtained with standard techniques, especially for medical applications. For instance, tests performed to verify the susceptibility of bacteria to

antibiotics are usually carried out at 37 °C.

To this aim, a Peltier module was integrated to the sample holder, as showed in Fig. 3.9. A Thorlabs TEC2.5-3 Thermoelectric Cooler (TEC) is sandwiched between the sample holder and a heat dissipator and it is driven by a T-Cube TEC controller (Thorlabs). Thermal conduction is ensured by a layer of thermal paste, while the TEC controller feedback is given by a thermistor (Thorlabs TH10K) embodied in the sample holder: to attach it, a groove was drilled in the sample holder and the thermocouple was immersed in TBS (Thermal Bonding System, Electrolube), a two part epoxy that after curing provides excellent thermal conductivity while being electrically insulating [117].

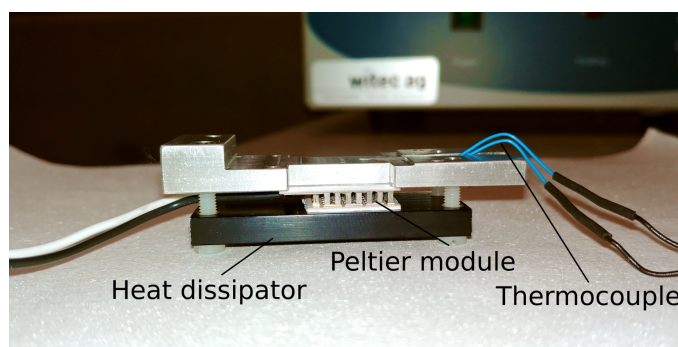


**Figure 3.9** – Peltier module integrated to the sample holder. A heat dissipator allows for creating the “cold” side and a thermistor embedded in the sample holder provides the feedback for the TEC driver.

#### 3.2.2 Manipulation and storage of bacteria

Our photonic crystal cavity is a promising tool for biological analysis and optical trapping experiments involving living bacteria were carried out. The bacteria studied belong to risk group 1, that includes biological agents “that are most unlikely to cause human disease” [118] and their characteristics will be detailed in section 5.1. As they are not pathogen, it is possible to store and manipulate them in a regular optics laboratory, wearing gloves and protective goggles but without any special safety procedure. Bacteria were provided by Pierre Marcoux in the context of the collaboration with the groups in Grenoble and most of the measurements included in this thesis were performed at CEA Grenoble.

Nevertheless, a working station for bacteria was implemented also here at EPFL, especially to take advantage of the microfluidic control possible on our setup. The core equipment, showed in Fig. 3.10 (a), consists in a fridge to store bacteria (a regular compact refrigerator from Kibernetik) and in an incubator to perform bacterial cultures (Witeg AG). Those latter are carried out on prepared Petri dishes because of their ease of use. Two types of prepared Petri dishes 3.10 (b) were used, both purchased from VWR chemicals and containing Trypticase Soy Agar (TSA) and Columbia Blood Agar (CBA). They are both based on Trypticase soy agar, a standard growing medium in gel state that contains enzymatic digests of casein and soybean meal. The CBA type also contains 5% of sheep blood and it is thus richer in nutrient elements.

### Chapter 3. Experimental setup and characterisation

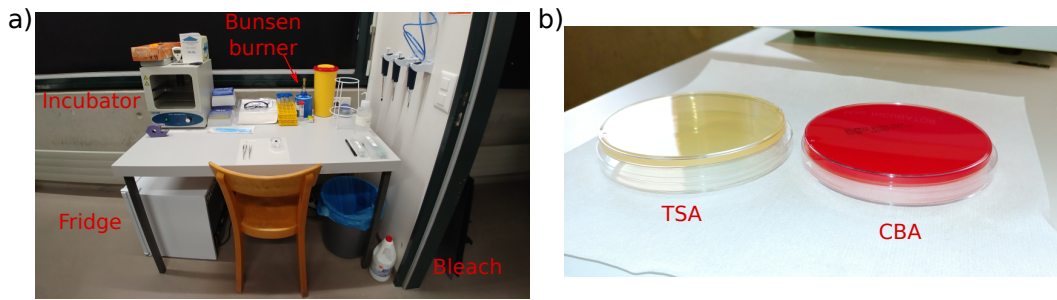


**Figure 3.10** – The bacteria working station. The basic elements are a fridge to store bacteria, an incubator to grow them and a Bunsen burner to ensure the sterility of the environment.

The first step to carry out experiments involving bacteria is to perform bacterial monocultures. For this purpose, an aseptic environment is required. A laminar flow hood is the tool of choice in biological laboratories, but it was not available in our optics lab. To ensure the sterility of the environment, a Bunsen burner was used: it is a technique commonly used when a hood is not available and the working principle resides in the fact that the heated air around a lit Bunsen burner creates an updraft that sends contaminants away from the specimen [119]. Working close enough to the flame (in a 15-20 cm range) allows to avoid plate contamination.

Secondly, the grown bacteria need to be suspended in water, so that they can be inserted in the microfluidic channels and transported in the vicinity of the photonic crystal cavity. Deionized water from the cleanroom was used and inserted into sterile tubes (15 mL cellstar<sup>®</sup> tubes, Grenier bio-one).

Finally, at the end of the day, the tubes and the Petri dishes containing bacteria that need to be trashed are filled with bleach to avoid any kind of contamination.

### 3.3 Experimental setup in CEA Grenoble

The setup used during the experiments performed in Grenoble is depicted in Fig. 3.11 and more details can be found in Ref. [120].

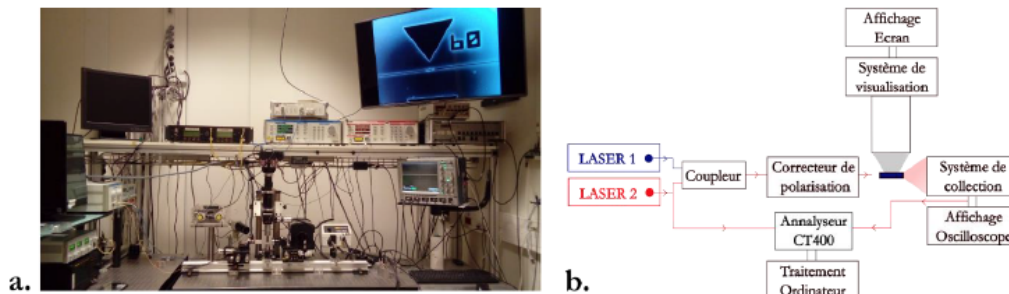


**Figure 3.11** – Experimental setup in Grenoble: picture (a) and schematic representation (b). From Ref. [120].



The working principle is the same as the one that we have here at EPFL: light from a tunable laser (Yenista Tunics) is injected in the waveguides with a lensed fiber, while on the other side of the sample the transmitted light is collected with a microscope objective and its intensity is monitored and saved with a digital oscilloscope. Polarisation is controlled with a paddle polarisation controller and a commercial camera (Sony  $\alpha 7S$ ) on top of the sample provides the visible range imaging of the surface. Moreover, the sample holder has a Peltier module that allows for varying temperature measurements. In addition, a setup involving two laser sources was also implemented and the light was injected in a 50:50 optical fiber coupler. In this case, the detection was simply performed with the oscilloscope.

### 3.4 Experimental procedure

Generally, two experimental procedures are carried out: one to characterise the photonic crystal structures and one to perform optical trapping experiments.

In the first case (Fig. 3.12), the transmission and surface emission spectra are collected. Light from a tuneable laser is injected and the transmission through the sample is recorded with a power meter. A microscope objective collects the near field profile of the cavity mode and its intensity is measured with a photodiode. A wavelength scan is performed for a spectral range of 8 nm around the resonance frequency with a wavelength increment of 0.015 nm and the two spectra are plotted. The cavity mode is excited by evanescent coupling from the W1 waveguide: the cavity resonance corresponds to a minimum in transmission and a maximum in surface emission. In Fig. 3.12 (c) an example of the two spectra is shown.

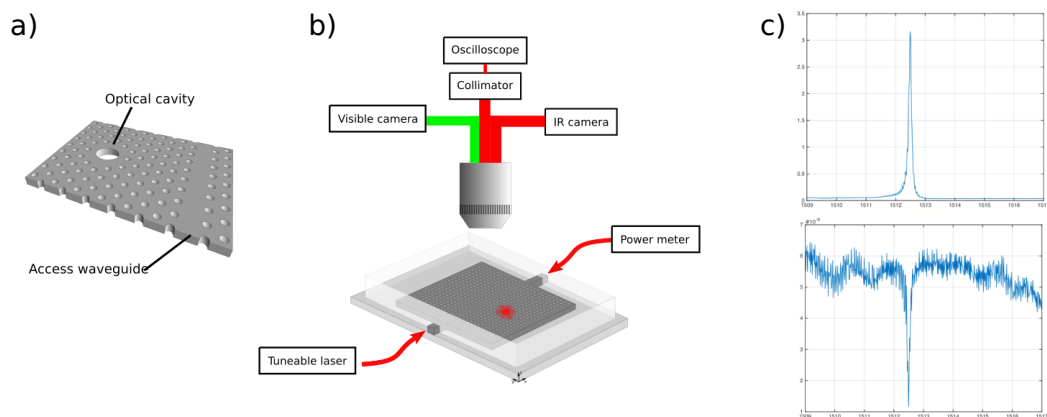


**Figure 3.12** – (a) Representation of the optical cavity and of the W1 waveguide. The cavity mode is excited by evanescent coupling with the W1 propagating modes. (b) Experimental setup used for sample characterisation. (c) Typical surface emission and transmission spectra.

While performing optical trapping experiments, on the other hand, the temporal behaviour of the transmission is monitored, in presence or in absence of the trapped object (Fig. 3.13). Light is injected at the resonance frequency and the transmission is recorded. In this case, the

## Chapter 3. Experimental setup and characterisation

photodiode is used instead of the power meter because of its better sensitivity. In Fig. 3.13 (b), a typical curve is showed, where the three regions correspond to different moments: first, the laser is off, second, the laser is turned on and third, an object is optically trapped.

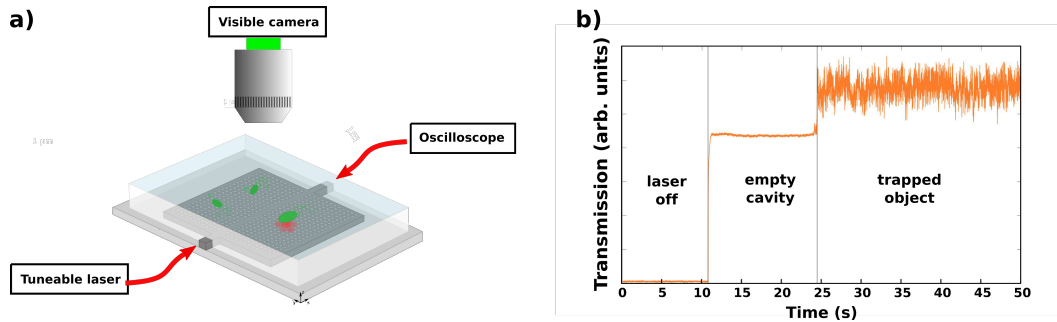


**Figure 3.13** – (a) Basic experimental setup used for optical trapping experiments. (b) Example of a transmission record in function of time.

### 3.5 Device characterisation

Before performing optical trapping experiments, a characterisation of the sample is carried out. The optical properties of the photonic crystal structures are assessed by recording the transmission and the surface emission spectra for all the PhC cavities present on the chip and the correct operation of the microfluidic elements is also verified.

This section provides the details of those characterisations.

#### 3.5.1 Optical characterisation

The optical characterisation of the photonic chip is a necessary step that permits to assess the overall quality of the sample and hence to obtain information on the quality of the fabrication process. Secondly, it allows for choosing the photonic crystal cavities more suitable for the desired application.

As a matter of fact, many photonic crystal structures are present on the same chip (up to 96) and some variations are introduced, such as varying the radius of the holes, changing the distance between the cavity and the W1 waveguide, modifying the ebeam writing resolution, etc. Moreover, some defects can be present, limiting the performance of the structures: defects in the lattice or in the access waveguides, errors in the facets cleaving, resist residues or dust particles on the sample surface, and a careful characterisation is the starting point for further usage of the chip.

By recording the transmission and the surface emission spectra, the resonance frequency and the quality factor of the optical mode are determined, together with the transmitted intensity through the sample waveguides and the surface emission intensity. A large number of cavities permits to have many options and to choose the cavity most adapted for the object to be



trapped.

### Resonance frequency and quality factor

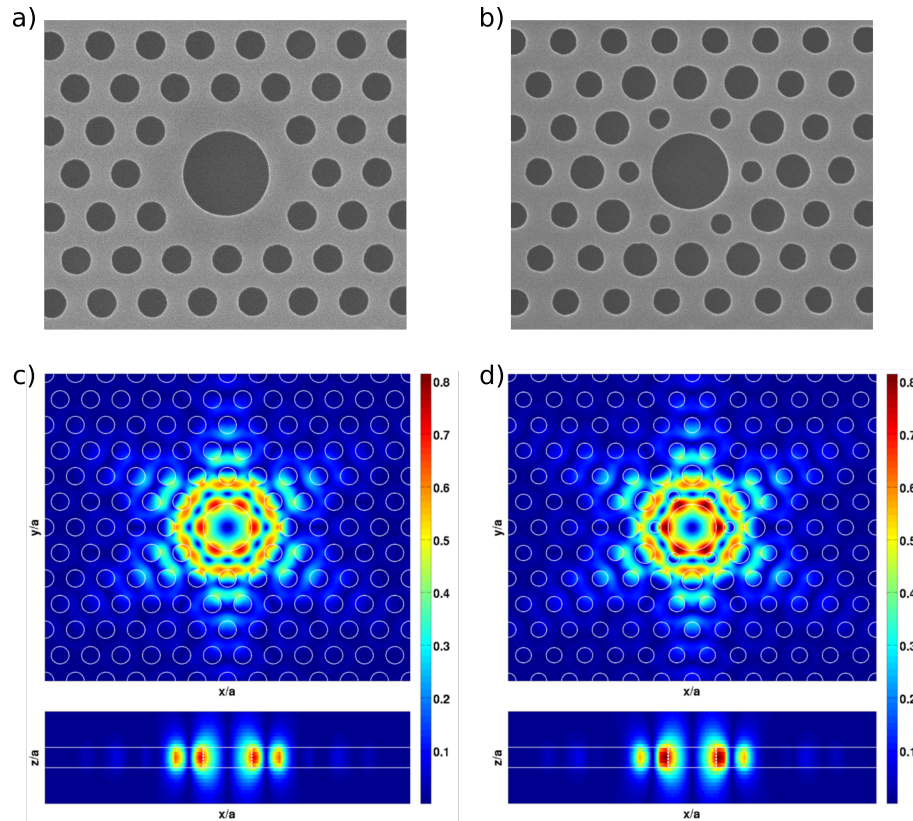


**Figure 3.14** – SEM images of an unoptimised (a) and of an optimised (b) optical cavity. (c) and (d) Simulations of the confined fields for the two types of cavity. The optimised one features a larger overlap between the hollow volume and the confined field. The optimisation and simulations were performed by M. Minkov.

Two types of hollow photonic crystal cavities were fabricated (Fig. 3.14): the first one, introduced in Chapter 1, consists in a defect created by enlarging one of the lattice holes (a). The second one is an optimisation of the cavity (a), obtained by modifying the radius and the position of the two closest rings of holes (b). The optimisation was computed by Momchil Minkov and the design parameters of the two types of cavities are listed in Tab. 3.1. Both cavities are designed to have a resonance wavelength around 1550 nm and the cavity of type (b) was optimised to obtain a larger overlap between the confined mode and the hollow volume, as shown in the field simulations in Fig. 3.14. This aspect is of large interest in particular for sensing applications, as a larger overlap with the hollow volume also results in a larger overlap with the trapped objects.

In Tab. 3.1 the fabrication parameters (used for the ebeam writing) are listed together with the design parameters: as mentioned in Section 2.4, an enlargement of the holes appears during the

### Chapter 3. Experimental setup and characterisation

fabrication process. This enlargement depends on the size of the holes (intra shape proximity effects) and it is around 25 nm for the lattice holes. As a test, several variations in the holes size were performed and the best parameters found are listed in Tab. 3.1. For the cavity of type *b*, the design parameters were initially used, but the resonance wavelength resulted to be close to 1600 nm, a value not suitable for optical trapping experiments. In fact, these experiments are carried out in aqueous environment and as we will see this causes a shift of  $\sim 35$  nm in the resonance wavelength, resulting in the trapping mode lying out of our laser wavelength range (1470 to 1620 nm). To avoid this inconvenience, the lattice constant was reduced to 420 nm and the hole sizes were scaled accordingly and resonance wavelengths around 1520 nm were obtained.

	First general cavity (a)		Optimised cavity (b)	
	Goal value	Fabrication value	Goal value	Fabrication value
Lattice constant (nm)	420	420	430	420
Lattice holes radius (nm)	125	100	110	85
Cavity hole radius (nm)	350	335	324	300
First ring holes radius (nm)	-	-	89	65
First ring holes displacement (nm)	-	-	86	86
Second ring holes radius (nm)	-	-	145	127
Second ring holes displacement (nm)	-	-	14	14

**Table 3.1** – Design parameters and parameters used during the fabrication process for the unoptimised and the optimised cavities.

Besides the geometrical parameters of the cavity, the distance from the W1 waveguide was also varied, from 3 to 5 lattice rows. In this way it is possible to obtain different overlaps between the W1 and the cavity modes, resulting in different quality factors [121] for the same modal volume. As the distance increases, the quality factor also increases, because of the reduction of the coupling losses. Conversely, assuming a weak evanescent coupling mechanism [122], as the coupling distance increases, the amount of energy coupled to the cavity mode is expected to exponentially decrease.

To determine the quality factor of the cavity mode, the collected transmission and surface emission spectra are observed or, for automatized Q determination over a large number of cavities, their spectra is fitted with a Lorentzian-type envelope, as showed in Fig. 3.15. The transmission curve shows larger Fabry-Perot modulations due to the reflections at the interfaces, so the surface emission curve is usually considered.

Typical quality factors values for the unoptimised cavity are of the order of 3-4000 for 3 rows of distance, 8-10000 for 4 rows and more than 15000 for 5 rows. In particular, the largest measured quality factors were as high as 12000 for 4 rows and 16000 for 5 rows.

For the optimised cavity, on the other hand, the measured quality factors are much smaller, as expected due to the fact that the objective of the optimisation was to obtain a large overlap

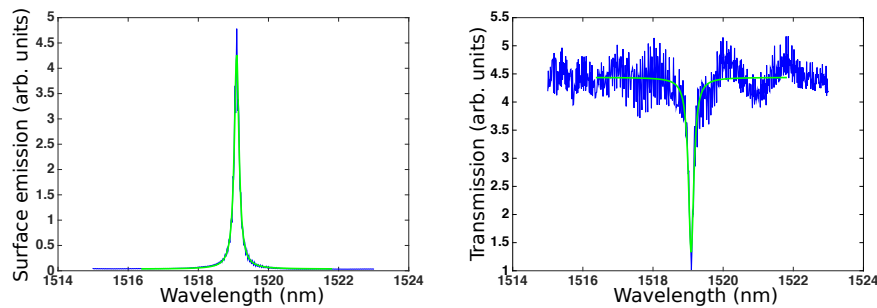


**Figure 3.15** – Lorentzian fit for the transmission and surface emission spectra of the cavity m6\_10. A quality factor of more than 10000 is calculated.

with the hollow volume and not to increase the Q. Typical values are  $\sim 500$  for 3 rows,  $\sim 1000$  for 4 rows and up to 2000 for 5 rows.

**Dependence on the surrounding medium** The band structure, and hence resonance frequency and the quality factor of the cavity mode, strongly depends on the medium surrounding the photonic crystal structures: in our case, the two considered media are air and water.

Even though the optical trapping experiments are performed in water, the first characterisation is carried out in air. This is easier from an experimental point of view and it permits to obtain clearer information on the device performances.

On the optical point of view, the field confinement is stronger when the photonic crystal is surrounded by air and hence both the quality factor and the transmitted intensity are larger: it is thus easier to determine the resonance frequency and the spectral shape of the resonance and consequently to choose the cavities more suitable for the desired application. Moreover, a characterisation in air is particularly important in the case of using the anti-reflection coating as a strategy to reduce the Fabry-Perot interference pattern: in this case, a characterisation before and after depositing the oxide film onto the facets is performed and the quality of the film is verified.

On the other hand, on the practical point of view, characterising the sample in air is advantageous because it is possible to do it either before or after integrating the chip with the microfluidic layers. Moreover, the system of microfluidic tubing can be avoided, that as it was shown in Sec. 3.2.1 can induce mechanical tensions in the sample. In addition, as we will see in the next section, the microfluidics showed to be fragile over a large number of opening/closing cycles of the valves and reducing those actuations to the minimum when not performing optical trapping experiments ensures a longer sample lifetime.

The immersion of the photonic crystal devices affects both the quality factor and the spectral position of the resonance frequency, due to the decrease of refractive index contrast. When a PhC structure is fully immersed in water, the eigenmode undergoes a redshift of  $\sim 35$  nm and

### Chapter 3. Experimental setup and characterisation

the quality factor is reduced, as shown in Fig. 3.16. For an unoptimised cavity, with 4 rows of distance to the w1 waveguide, typical quality factor values in water are of the order of 3-4000. Moreover, due to the smaller field confinement and to the increased losses, the transmission intensity is also smaller.

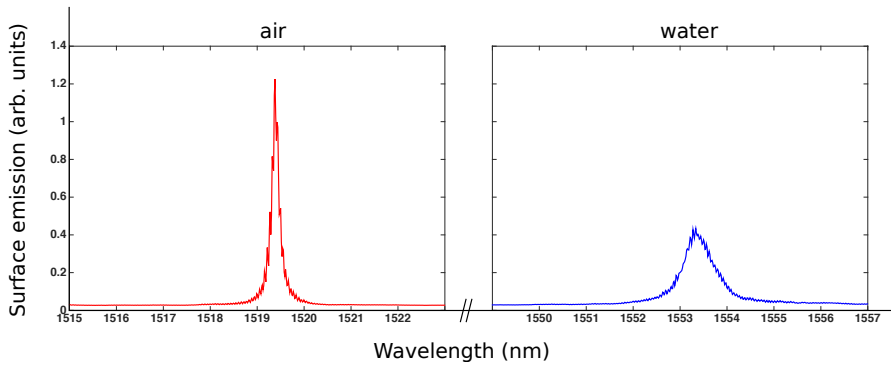


**Figure 3.16** – Water induced resonance shift. When immersing a PhC in water, the resonance frequency undergoes a redshift of  $\sim 35$  nm, 34 in this case. A decrease in the surface emission intensity and a degradation of the quality factor are also visible.

The cavity resonant frequency shift is very robust with respect to fabrication imperfections and to design variations: while for different designs the resonance frequency can change of tenths of nanometers, when immersing a PhC in water it always gives a shift of  $35 \pm 1$  nm. In this way, it is also possible to verify the photonic crystal filling. As an example the case of the “swimming pool” configuration can be considered: in the “channel microfluidics” the small pressure introduced in the transport channel allows for overcoming the silicon hydrophobicity and to fully fill the channel. On the contrary, in the “swimming pool” configuration the hydrophobicity of the silicon surface is not overcome and the observed shift is of only 12.5 nm, corresponding to just a layer of water on the top surface of the PhC.

Some optical trapping experiments were performed in this configuration, but when increasing the power of the beam injected some air bubbles were created. To avoid this undesired phenomenon, the sample can be immersed for 1 minute in a suspension of BSA (Bovine Serum Albumine), a protein widely used in the biophotonic community. It creates a thin layer on the sample surface and its primary use is to avoid bacterial adhesion to the surfaces, but it also hugely increases the hydrophilicity of silicon, as shown in Fig. 3.17. The BSA film can be created either by immersing the sample in a BSA solution before integrating the microfluidics, or a posteriori, by injecting the solution into the channels. The photonic crystal cavities were characterised before and after the creation of the BSA film and a small shift of 0.2 nm was observed, with no relevant impact on the quality factors.

One last consideration on the photonic crystal filling: for optical trapping experiments involving polystyrene nanoparticles, a 1% solution of Triton X-100 is used instead of simple de-ionized water to promote the full channel filling. It helps in reducing the surface tension and as a plus also prevents polystyrene nanoparticles to attach one to the other. On the optical

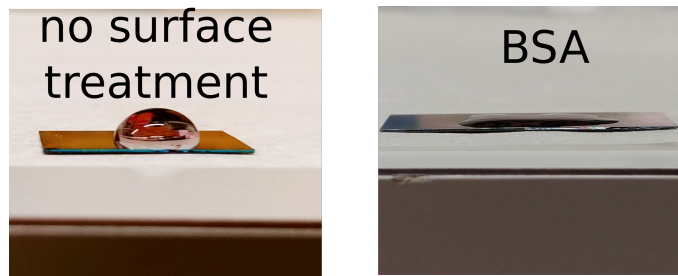


**Figure 3.17** – Silicon is naturally hydrophobic. After BSA treatment, the surface becomes strongly hydrophilic.

point of view, the resonance frequency is redshifted of less 1 nm and the quality factor remains unchanged. However, this method cannot be used with bacteria because Triton X-100 modifies the cell membrane: in fact, the permeabilization of cell membranes is one of its many uses.

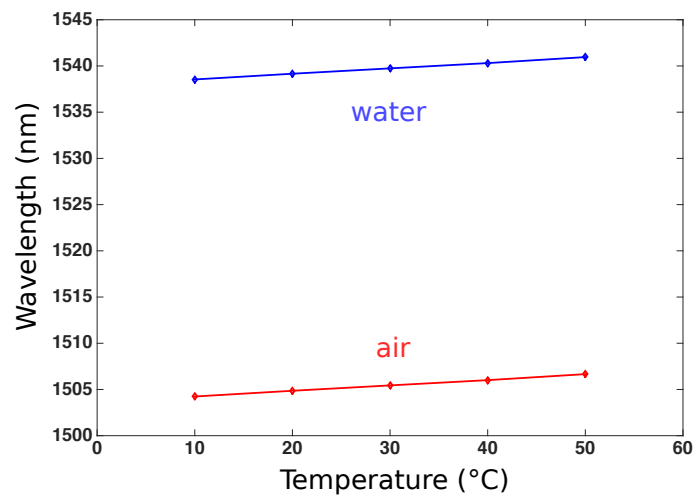


**Figure 3.18** – Temperature dependence of the resonance wavelength for the cavity n4\_4 in air and in water.

**Dependence on the temperature** Besides the dependence on the refractive index of the surrounding medium, the resonance frequency of the optical cavity also depends on the temperature, due to lattice deformation. A redshift of  $0.06 \text{ nm } ^\circ\text{C}^{-1}$  is observed and needs to be taken into account while performing experiments at different temperatures (Fig. 3.18).

Moreover, temperature effects are shown after several minutes of cavity excitation with high power (10 mW out of the laser source). Resonance shifts of the order of 0.02-0.05 nm were observed and they can be explained by an induced temperature increase in the cavity region. The initial resonance frequency is restored by flushing the system, but it is a variable that needs to be considered in optical trapping experiments, where the resonance shift is a quantity that gives important information on the trapped object.

### Coupling to optical fibers

Besides a sample featuring good optical properties in terms of quality factor and of transmitted intensity, an efficient coupling with the optical fibers is also crucial to obtain good performances while carrying out optical trapping experiments. In particular, the strategies implemented to improve the coupling between the sample waveguides and the optical fibers have two main objectives.

First, the reduction of the Fabry-Perot interference pattern due to reflections at the facets is of crucial interest. Those fast modulations, corresponding to a 1 cm long cavity (the width of the sample), create a huge noise that can even prevent the correct resonance frequency determination (Fig. 3.19).

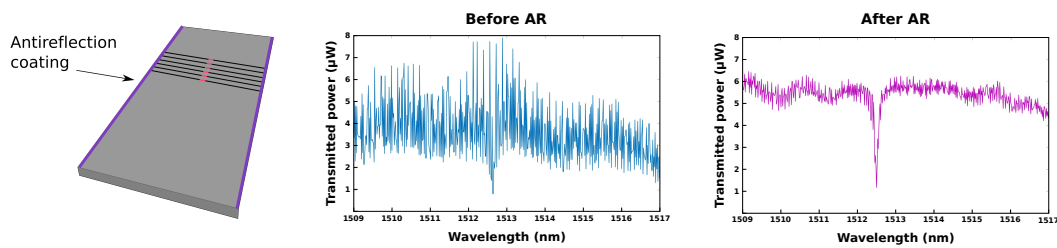


**Figure 3.19** – The deposition of an anti-reflection coating onto the sample facets strongly reduces the Fabry-Perot interference pattern due to reflections at the facets.

A second objective, on the other hand, is to increase the amount of light coupling in order to deliver more optical power into the cavity when considering the same power from the laser source.

During this thesis, two strategies were used, as introduced in Chapter 2: firstly, the deposition of an anti-reflection coating and secondly, the use of SU8 mode adaptors. In Fig. 3.19, the transmission spectrum of the same cavity is shown before and after the anti-reflection coating. The Fabry-Perot fringes are largely reduced and the cavity resonance is clearly visible in the second spectrum. On the transmitted power level, on the other hand, only a slight improvement is shown.

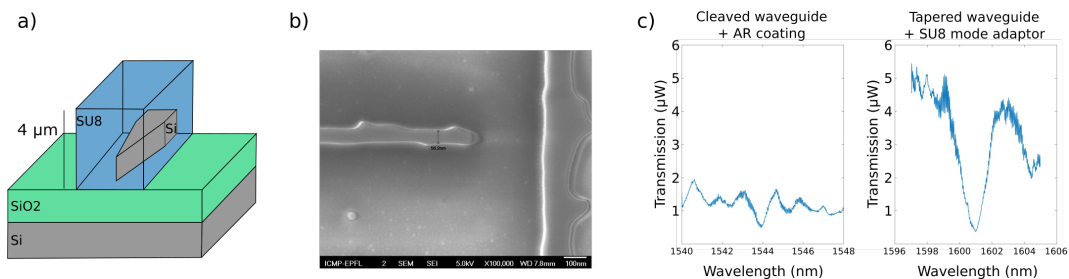


**Figure 3.20** – (a) Drawing of the tapered silicon waveguide surrounded by a  $4\ \mu\text{m} \times 4\ \mu\text{m}$  SU8 mode adaptor. (b) SEM image of a tapered waveguide termination. The poor quality of the tapered structure is to be attributed to a slight underexposure of the ebeam resist. (c) Typical transmission spectra in the case of AR coating or SU8 mode adaptors.

In Fig. 3.20, on the contrary, the contribution of a SU8 mode adaptor [123, 124] is presented. A SU8 waveguide, 1 mm long and  $4\ \mu\text{m} \times 4\ \mu\text{m}$  in section, is placed onto a tapered waveguide. The reflection at the facets are reduced thanks to the tapers in the silicon waveguide and to the refractive index of SU8 (1.58 at 1550 nm). Moreover, with respect to a cleaved waveguide (whose section measures  $220\ \text{nm} \times 3\ \mu\text{m}$ ), the mode size of the lensed fiber is matched and hence a larger coupling is expected. Fig. 3.20 (c) shows two typical transmission spectra. Despite the poor quality of the fabricated taper, an increase by a factor of five in the transmitted intensity can be observed. A better quality fabrication is expected to increase the coupling efficiency between the optical fibers and the sample waveguides.

Tapered silicon waveguides terminations, together with SU8 mode adaptors appear as a good solution in both reducing the reflections at the facets and in ensuring a better coupling with the optical fibers. However, they have some drawbacks. First, the coupling between the modes guided in the SU8 waveguide and in the silicon respectively is only obtained thanks to the overlap between the two modes, and scattering at the end of the SU8 waveguide is still present. Moreover, on the practical point of view, SU8 deposition requires surface preparation with oxygen plasma, that limits one of the advantages of our microfluidics, i.e. the possibility to remove it easily.

For the future, a strategy consisting in using a 3D printed polymer adaptor [125, 126] will be implemented. Besides the possibility to create a structure tapered in 3D, it will also permit to couple regular tapered single mode fibers, instead of using more expensive and fragile lensed fibers.





## 4 Self-Induced Back-Action and “cage” trapping

The mutual interaction between a trapped object and the cavity eigenmode, i.e. the Self-Induced Back-Action (SIBA) effect, is the central mechanism of the trapping dynamics, as mentioned in Chapter 1. It allows for the trapping of particles but also for the simultaneous acquisition of information on the trapped specimen. This mechanism, together with the low powers necessary to trap specimen, make this kind of optical tweezers excellent candidates for applications in single-particle or bacteria identification.

In this chapter, the trapping capabilities of our cavity will be presented. Depending on the trapping mechanism and on the associated potential, two regimes can be identified and labelled as “classical regime” and “cage regime”. In particular, the advantages of the cage regime will be shown, especially when considering the trapping of biological entities.

Finally, the trapping of polystyrene nanoparticles with different diameters will be discussed and the analysis method presented.

For the sake of clarity and completeness, some results previously obtained in the group will be reported. This is the case of sections 4.1.3, 4.2 and 4.3. More details on those results can be found in Ref. [114], [25] and [85].

### 4.1 Resonant optical trapping in hollow 2D PhC cavity

Self-Induced Back-Action effects are based on the mutual interaction between a resonant structure and an external object. In this section, we consider the trapping capabilities of our cavity, i.e. the effect of the confined field onto objects suspended in the surrounding medium, while in next section the effect of a trapped object onto the confined mode will be analysed.

The presence of large field gradients is imperative to obtain systems that can act as optical tweezers: in fact, the gradient forces are responsible for trapping (Section 1.2) and in our case field gradients are provided by a sufficiently high quality factor of the cavity and by a sufficiently small volume of the confined mode. For the unoptimised cavity, quality factors

of 3-4000 are usually measured in water, while a modal volume of  $2.3 (\lambda/n)^3$  was computed [114].

Cavities featuring larger quality factors have been reported [28, 29, 30], but it is not the most crucial aspect to be considered when investigating the trapping capabilities of a device. In fact, a large interaction between the confined field and the object to be trapped is a pivotal requirement for optical trapping and the hollow nature of our optical cavity maximises this aspect. This represents a clear advantage for sensing and trapping applications, especially for objects with sizes in the few hundreds of nanometers range, like nanospheres or viruses, that can fit inside the cavity hole. Nevertheless, objects larger than the central hole size can still be trapped, as it will be shown in Chapter 5 for bacteria, which size is on the few microns scale.

Moreover, it will be shown that a smaller quality factor could even be more adapted for the trapping of specific objects (section 4.3).

In this chapter, we will focus on the trapping of polystyrene nanoparticles, to introduce the experimental procedure and the trapping mechanism.

### 4.1.1 Experimental procedure

An optical trapping experiment is performed as follows. To begin, a suspension of nanoparticles in water and 1 % v/v of Triton is prepared. Particles from Fisher Scientific are used: they come in a suspension with a concentration of 1 % in volume and are diluted 1000 times. This dilution, found empirically, is a good compromise between too small and too large concentrations: a too large concentration could prevent single-particle experiments, as several particles could be trapped at the same time. On the other side, a too small particle concentration would result in an increase of the experiment time, needing to wait a long time to find a particle in the vicinity of the cavity region.

After preparing the suspension, 1 mL is taken with a syringe, inserted in the input tube and the liquid is let free to flow. In case of need, a small pressure can be applied to facilitate the channel filling, but usually the difference in height between the input and the output extremities is sufficient to create a flow. The sample is then mounted on the sample holder and carefully aligned. Before starting an optical trapping experiment, Quake valves are actuated: the channels close and the particles undergo Brownian motion (Sec. 4.1.2) without any external drift.

Light around 1550 nm is injected with a tuneable laser into the sample waveguides and the transmitted intensity as well as the surface emission are recorded (Fig. 4.1). The resonance frequency is determined by the maximum of the surface emission and by the minimum of the transmission intensities. The TE polarisation of the incoming beam is also assessed: the  $\lambda/2$  and the  $\lambda/4$  plates are rotated to maximise both the transmission and the surface emission, as only TE-like modes are supported by the photonic crystal defects.

#### 4.1. Resonant optical trapping in hollow 2D PhC cavity

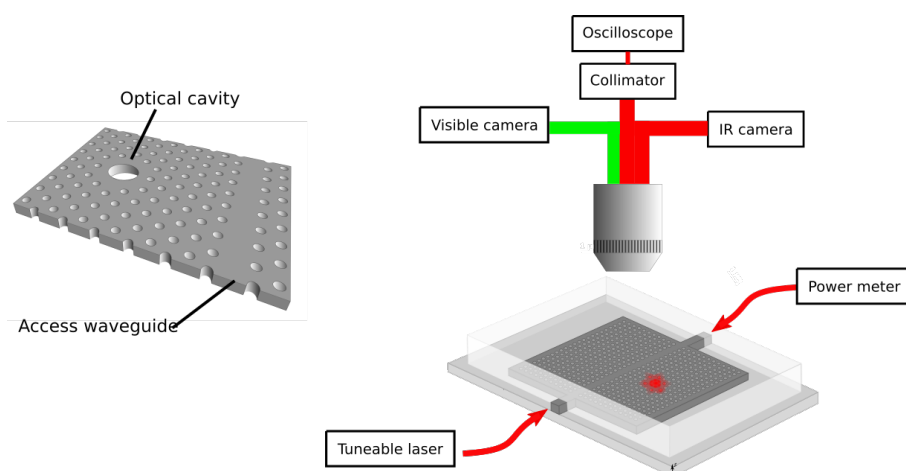


**Figure 4.1** – Schematic representation of the experimental setup used for optical trapping experiments.

A visible camera, focalised onto the photonic crystal surface with a 100x oil immersion objective, allows for monitoring the occurring of trapping events (Fig. 4.2). The illumination line, that is also responsible for the excitation of the particle fluorophores, is focalized onto the sample surface with the same microscope objective and permits visual control of the particles position. Nanoparticles that undergo Brownian motion are free to move in 3D into the entire volume of the channel, which is up to 20  $\mu\text{m}$  thick, and the intensity of the emitted light depends on the distance from the focal plane. When a particle is trapped inside the hollow cavity it appears very bright as it is confined on the PhC surface (Fig. 4.2).

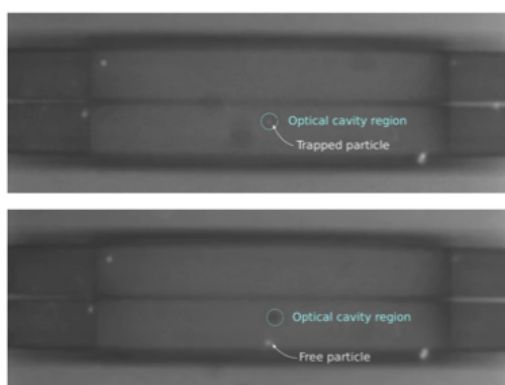


**Figure 4.2** – 500 nm fluorescent particle optically trapped in the hollow photonic crystal cavity.

The same intense brightness is observed for sedimented particles, so one could wonder that the nanospheres are attached on the edges of the cavity and not optically trapped. Nevertheless, this possibility is excluded by the fact that as soon as the cavity excitation is turned off, the particles immediately resume their Brownian motion and move away from the cavity region.

### 4.1.2 Brownian motion

In the previous section, we mentioned Brownian motion to describe the behaviour of the suspended nanoparticles. Polystyrene nanospheres immersed in water can be considered as a colloidal suspension: their size (few hundreds of nanometers in diameter) is much larger than the one of water molecules but they are also small enough to neglect sedimentation phenomena. In fact, to ensure the absence of sedimentation, the thermal kinetic energy has to overcome the sedimentation energy. This results in a constraint on the colloid radius. For polystyrene, whose density is of  $1050 \text{ kg m}^{-3}$ , it has been calculated that at room temperature it has to be  $r < 15.4 \mu\text{m}$  [120].

Moreover, the thickness of the microfluidic channel is either 10 or 20  $\mu\text{m}$ , in both cases much larger than the particle size, and thus it doesn't affect the diffusion dynamics of the particles inside the fluid.

It is thus possible to affirm that, in absence of external forces, particles undergo Brownian motion. The diffusion coefficient can be expressed by the Einstein relation [65]

$$D = \frac{k_B T}{6\pi r \eta} \quad (4.1)$$

where  $\eta$  is the viscosity of the liquid.

We can note that for smaller particles the diffusion coefficient is larger: they move faster and in an optical trapping context it means that stronger forces will be necessary to trap them.

### 4.1.3 Trapping capabilities

This cavity was successfully used for the optical trapping of polystyrene nanospheres, but also of bacteria, as it will be discussed in the next chapter.

In particular, optical trapping of 500 nm nanoparticles was reported with estimated powers in the vicinity of the centre of the W1 waveguide as low as 37  $\mu\text{W}$ , as shown in Fig. 4.3 [127]. In Fig. 4.3, the escape power threshold is plotted with respect to the excitation wavelength, considered as a detuning from the empty cavity resonance. The cavity was excited at a fixed wavelength and with the maximum power (10 mW from the laser), that was later decreased until the particle escaped, meaning that the forces acting on the nanosphere were too low to confine it in the cavity volume. The coloured area corresponds to the region where optical trapping is possible.

Few considerations can be done on Fig. 4.3: first, the resonant nature of the trapping mechanism is clearly revealed, as optical trapping is possible only for a limited range of wavelengths around the empty cavity resonance.

## 4.2. Particle-dependent resonance frequency shift

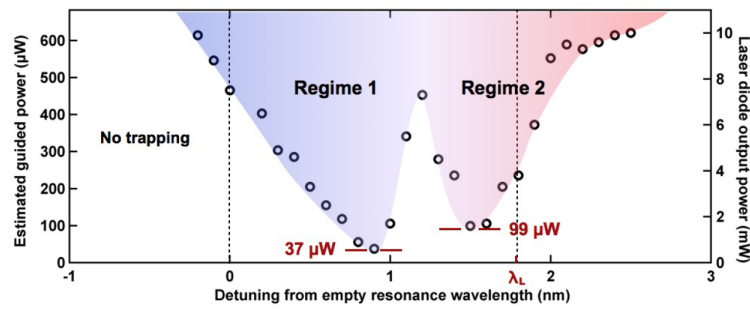


**Figure 4.3** – Escape thresholds for an optically trapped 500 nm nanoparticle as a function of the detuning, i.e. the difference between the excitation wavelength and the empty cavity resonance one. The coloured area corresponds to the region where optical trapping is possible. Reprinted from [127].

Secondly, two minima in the escape threshold appear. They reveal the presence of two regimes, associated with two distinct trapping mechanisms and potentials that will be discussed in section 4.3.

Finally, the estimated power in the cavity necessary to trap 500 nm polystyrene nanospheres is around  $100\ \mu\text{W}$ , which is two order of magnitude smaller than the necessary one to trap submicron particles with classical optical tweezers [128]. The value of  $37\ \mu\text{W}$  corresponds to an injected power of less than 1 mW, while  $100\ \mu\text{W}$  corresponds to 2 mW from the laser. In the following, for simplicity, the power ejected by the tunable laser will be mentioned, knowing that the orders of magnitude of the estimated powers in the cavity are around the hundred of microwatts. It is important to note that the estimation of the power is done considering the center of the W1 waveguide, and that the coupling to the cavity mode and the field enhancement in the cavity are not considered. Fluorescent nanoparticles were trapped for over 30 minutes without any photobleaching effect, suggesting that our cavity is suitable for the trapping of objects that could be damaged by high powers, such as biological entities.

When considering 250 nm particles, on the other hand, they were also successfully trapped, but with a larger estimated power of  $360\ \mu\text{W}$ . This necessity to increase the power is due to the fact that the gradient forces scale with the third power of the radius (Eq. 1.14) and to the fact that Brownian motion, on the contrary, increases with size reduction (Eq. 4.1.2).

## 4.2 Particle-dependent resonance frequency shift

Differently from classical optical tweezers, where the trapped object does not have any impact on the trapping beam, in SIBA systems the particle also plays a fundamental role in the trapping mechanism and modifies the system by its presence. In particular, for resonant structures like our PhC cavity, the main effect is the redshift that it induces in the resonance frequency, caused by the higher refractive index overlapping with the confined field. This resonance shift is strongly particle-dependent and the effect of different parameters was investigated in previous work with FEM simulations [129]. The parameters considered were

the size, the refractive index and the shape, as illustrated in Fig. 4.4.

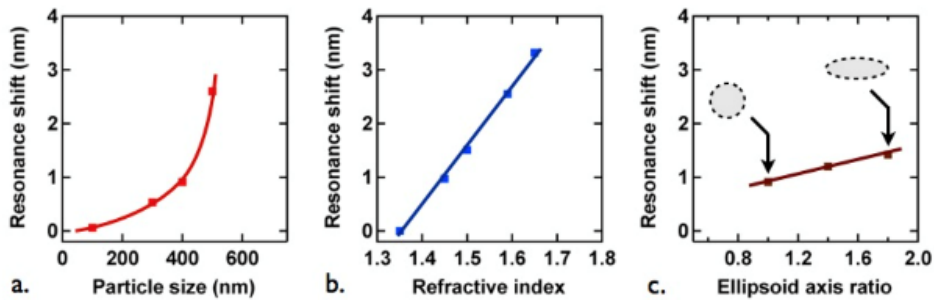


**Figure 4.4** – FEM simulations of the shift induced in the cavity resonance by varying parameters: (a) the diameter of a spherical nanoparticle, (b) the refractive index of a 500 nm nanosphere and (c) the aspect ratio for ellipsoidal particles with the same volume and refractive index. Reprinted from [129].

In Fig. 4.4 (a) polystyrene nanospheres are considered: the refractive index is fixed at 1.59 and the radius is increased from 100 nm to 500 nm. The cubic-shaped fitting of the four points is in agreement with the dependence on the volume of the polarisability of small dielectric particles given by the Clausius-Mossotti relation and it suggests that this kind of cavity is particularly adapted to distinguish small size variations in particles with sizes around the dimensions of central hole, that in this case is 700 nm. This can be explained by the fact that the overlap with the confined field into the hollow volume is maximum and so it is the induced shift.

In Fig. 4.4 (b) a 500 nm particle is considered and the refractive index is varied from the 1.33 (the one of water) to 1.68: a linear dependence of the resonance shift is observed and a shift of few nanometers is expected when increasing the refractive index.

Finally, in Fig. 4.4 (c) the resonance shift as a function of varying shapes is plotted. In this case, the shift shows to linearly increase with the shape modification from a sphere to an ellipsoid with the same volume, but the effect appears to be less important than the one induced by variations in size or in refractive index.

### 4.3 “Classical” and “cage” trapping regimes

As anticipated, when considering the excitation wavelengths that can be used for optical trapping two regimes appear (4.3). This behaviour is a signature of the SIBA effects that are present in our systems, as in both regimes the particle actively participate to the trapping mechanism.

To simplify, the two regimes can be described as follows:

- In the first regime, the cavity is excited at the resonance frequency of the empty cavity in water. We refer to it as “cage regime”.
- In the second regime, the cavity is excited at the resonance frequency supported by the

cavity when a particle is inside and we label it “classical regime”.

### Classical regime

The easier regime to describe is the “classical regime” (4.5). It corresponds to the same mechanism that happens in classical optical tweezers: the particle is trapped close to the maximum confined field, where the gradient forces are stronger. In this case, the excitation wavelength matches the eigenmode supported by the cavity when the particle is located inside hole.

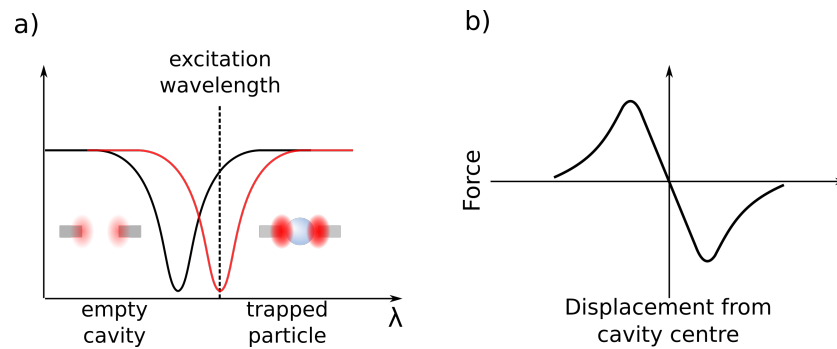


**Figure 4.5** – (a) The cavity is excited at its resonance wavelength when a particle is trapped. (b) Force profile experienced by the particle: it corresponds to a harmonic potential and a trap stiffness can be calculated.

The particle, by its presence, increases the trapping strength of the device. In fact, when the particle is located away from the central hole, a very weak coupling with the excitation laser is obtained, while the maximum is achieved when the nanosphere is inside. The force profile that is experienced by a trapped object is represented in Fig. 4.5 (b) and it is the same as the one of classical tweezers. In this case, it is possible to calculate the stiffness of the trap by using the theory of harmonic potentials. The experimental trap stiffness found by M. Tonin in Ref. [130] was  $k_{exp} = 300 \text{ pN } \mu\text{m}^{-1} \text{ mW}^{-1}$ , which is one order of magnitude larger than the one of classical tweezers for similar objects [131, 132, 133, 134].

### Cage regime

In this regime, the excitation wavelength is the one of the empty cavity: the confined field is maximum when the particle is far from the cavity and as soon as the nanosphere is trapped inside the cavity, the eigenmode is decoupled from the excitation mode (Fig. 4.6 (a)).

The interesting property of this trapping regime is the fact that when a particle is located inside the cavity hole, it does not experience any gradient force: it can be considered as a free particle. Brownian motion is recovered, but as soon as it moves away from the cavity region the gradient forces are restored and the particle is pulled back to the center of the cavity. In this sense, the particle can be described as a “free particle in a cage”. The force profile that is

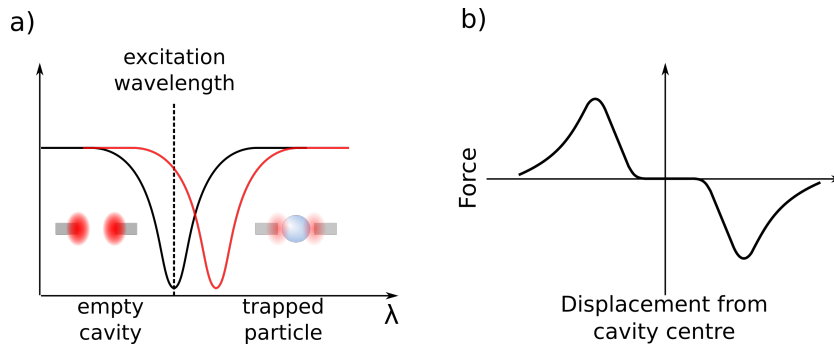


**Figure 4.6** – (a) The cavity is excited at resonance wavelength when the cavity is empty. (b) Force profile experienced by the particle.

experienced by the nanosphere is represented in Fig. 4.6 (b). In this case, as the potential is not harmonic, it is not possible to define a trap stiffness.

However, this trapping regime is particularly interesting for photosensitive objects as biological entities, because the exposure to the trapping field is strongly limited. Indeed, the particle is not continuously exposed to the confined field, but only when it moves far enough from the cavity center to restore the coupling with the empty cavity eigenmode.

### Choice of the cavity

A fundamental requirement for the existence of the cage regime is the fact that the shift induced by the trapped object has to be smaller than the mode linewidth (Fig. 4.7), otherwise the cavity eigenmode will not couple with the excitation wavelength.

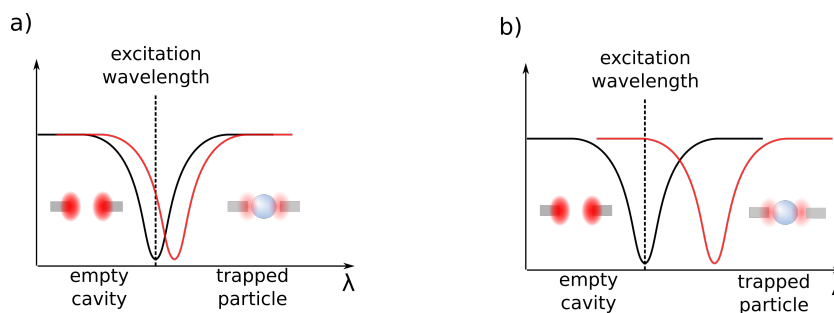


**Figure 4.7** – The necessary condition for the existence of the cage regime is that the shift induced by the trapped particle is smaller than the eigenmode linewidth.

This behaviour is particularly visible with the analysis of the cutoff frequency of the Power Spectrum Density (PSD). In Ref. [85] the PSD of a 500 nm nanoparticle trapped in three different cavities was considered. The cavity hole was at a distance of 3, 4 or 5 hole rows from the W1 waveguide and the three cavities were labelled cavity A, B and C respectively. As mentioned in Chapter 3.5, these different distances result in different couplings with the modes guided in the W1 waveguide, and hence in different quality factors and linewidths. The



### 4.3. “Classical” and “cage” trapping regimes

characteristics of the cavities used are summarised in Tab. 4.1.

	Coupling distance (hole lines from w1)	Resonance wavelength (nm)	Quality factor	Linewidth (nm)	Maximum induced shift (nm)
Cavity A	3	1583	1300	1.2	0.7
Cavity B	4	1600	1600	1	0.9
Cavity C	5	1580	3000	0.5	0.6

**Table 4.1** – Parameters of the cavities used for the PSD analysis. Table taken from Ref. [85].

In this case, the shift induced by a 500 nm nanosphere was around 1 nm. In Fig. 4.8 the cutoff frequencies are plotted with respect to the detuning from the empty cavity resonance. Different curves correspond to different injected powers. These images are specular to the curve representing the escape threshold of a trapping particle (Fig. 4.3) and the two trapping regimes appear for the cavities A and B, while the cavity C only supports the “classical” trapping regime, due to the fact that the induced shift is larger than the cavity eigenmode linewidth.

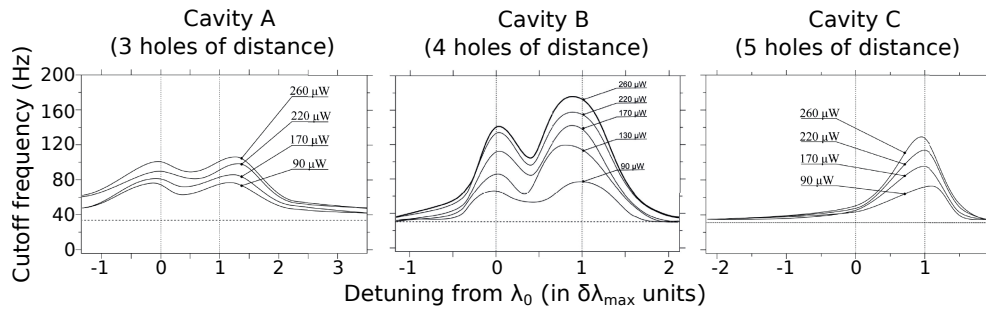


**Figure 4.8** – Cutoff frequencies for a 500 nm polystyrene nanosphere trapped in three types of cavity. The different estimated powers correspond to the power calculated in the vicinity of the centre of the w1 waveguide. Images adapted from Ref. [85].

A second remark on this figure is that the peaks obtained for cavity B are sharper than the ones of cavity A. For cavity A, the induced shift is only half than the cavity resonance linewidth and hence only small variations in the power of the confined field can be observed. On the other hand, for cavity B the induced shift is of the order of the eigenmode linewidth: in this case, when the particle is trapped inside the cavity, a very small power couples from the W1 waveguide.

These remarks lead to an important criterion in choosing the cavity most adapted for optical trapping, depending on the object and on the regime that is wanted to exploit. In particular, the use of the cage regime appears particularly interesting for biological applications and more in general for the study of photosensitive objects, or when the interest is on the dynamics of a nearly-free particle. For the optical trapping of 500 nm polystyrene nanospheres, quality factors of the order of 1600 in water showed to be the most suitable. On the other hand, to trap objects that induce smaller shifts (for instance smaller particles, or bacteria and viruses

that have lower refractive indexes) cavities with larger quality factors could be more adapted.

### 4.4 Particle differentiation: the case of 250 and 500 nm nanospheres

Besides the possibility of trapping specimen with very low powers, the SIBA effects supported by our system present another interesting advantage with respect to classical optical tweezers: the object is not only trapped, but it is also possible to acquire information on it. In particular, as the induced resonance shift is strongly particle-dependent, it can be used for particle differentiation.

As an example, the differentiation of 250 and 500 nm polystyrene nanosphere is presented in this section. The same principle was used for bacteria differentiation [87] and in Chapter 5 its application to bacterial Gram-type determination will be shown.

The basic idea of differentiation experiments is as follows (Fig. 4.9): the cavity is excited at the empty cavity resonance wavelength. This corresponds to a maximum of field confined in the cavity and conversely in a minimum in the transmitted intensity. When a particle is trapped, the induced shift can be detected by a transmission increment, that is particle-dependent and that can be used for differentiation.

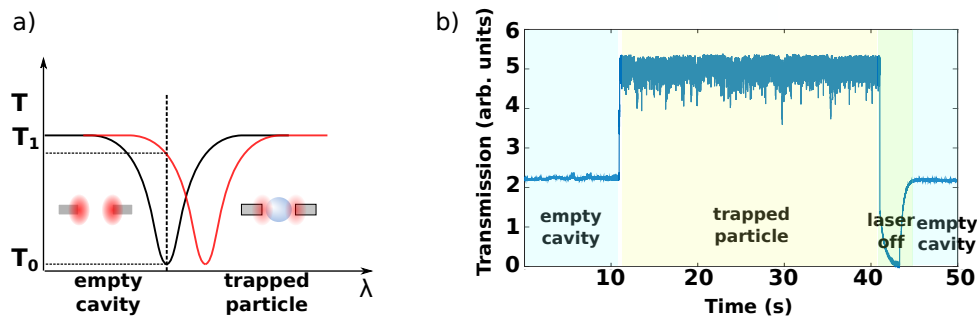


**Figure 4.9** – The particle-dependent shift induced in the cavity mode (a) causes a particle-dependent transmission increase (b).

The experiment consisted in trapping the two types of particles with the same injected power and in detecting the transmitted intensity over time with a photodiode. The transmission was recorded for one minute of trapping with a dedicated LabVIEW routine. To ensure the trapping of 250 nm nanospheres, the largest available power was injected into the sample waveguide, i.e. 10 mW from the laser source. Experiments with 100 nm nanoparticles were carried out as well, but the trapping was very unstable and possible for times of the order of 1-2 seconds. For this reason, these measurements are not included in the following analysis.

The trapping of nanoparticles in some cases was spontaneous: for the particles floating on the vicinity of the cavity, we simply waited for them to be trapped. However, as the particle concentration was low to prevent multiple trapping, in most cases auxiliary tweezers were used to accelerate the experiment: a 1300 nm beam, with a power of 10 mW, was focalised on

#### 4.4. Particle differentiation: the case of 250 and 500 nm nanospheres

the sample surface through a high NA objective connected to piezoelectric translators. The translators permitted to move the classical tweezers in the vicinity of a polystyrene sphere, and once it was trapped, to transfer it into the center of the cavity. The auxiliary tweezers were then turned off and the particle was trapped only by the field confined in the optical cavity.

##### Qualitative differentiation

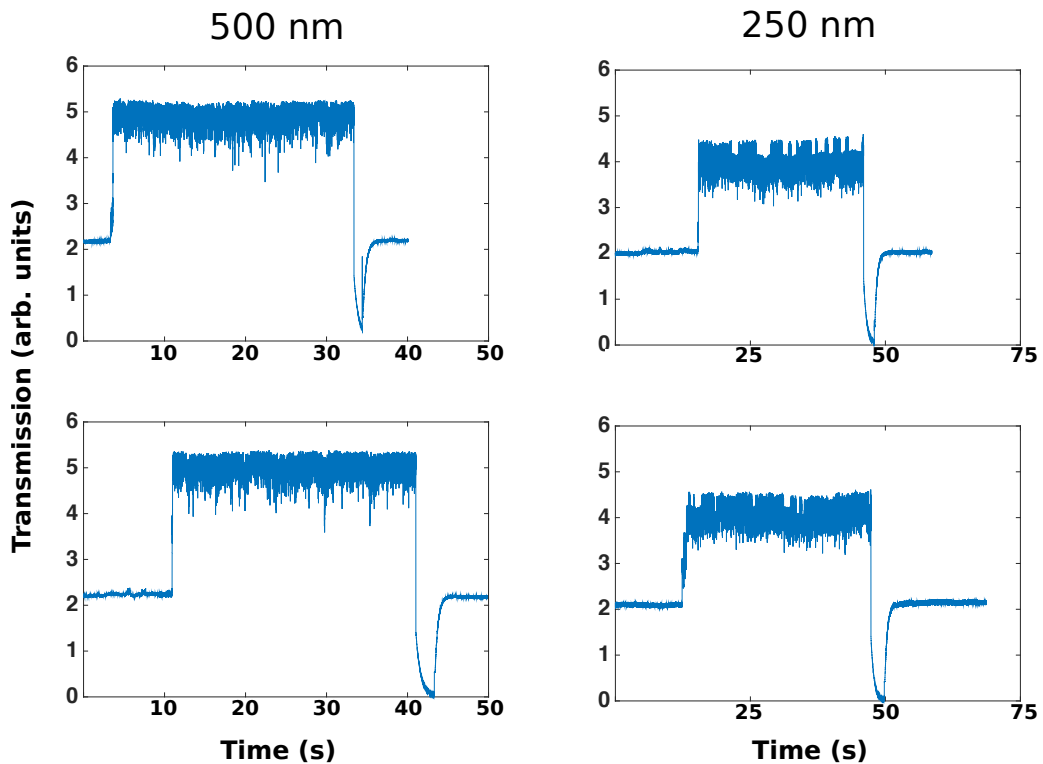


**Figure 4.10** – Two typical transmissions for 500 nm and for 250 nm PS nanospheres. The transmitted intensity is recorded for one minute of trapping.

For each particle size at least ten measurements, corresponding to ten different particles, were performed and a qualitative particle distinction can be carried out by direct inspection of the transmission records (Fig. 4.10). In Fig. 4.10, raw measurements for 250 and 500 nm nanoparticles are shown. As an example, two typical transmission recordings are plotted for each particle size. Particle differentiation appears possible by the simple observation of the plots, due to differences both in the mean value of the transmitted intensity and in the shape of the transmission curve.

Some preliminary remarks can be done before analysing the example cases:

- The more the particle is overlapping with the confined mode, the more the transmission is increased.
- The mean value of the transmission is linked with the mean shift induced in the cavity

resonance wavelength.

- When the transmission is maximum, a minimum of power is coupled to the cavity and the trapped particle is a “free particle” that undergoes Brownian motion.
- The amplitude of the transmission fluctuations is linked to the movement of the particle inside the optical cavity.

If we consider the mean of the transmitted intensities in Fig. 4.10, it is seen that it is larger for the 500 nm beads with respect to the 250 nm ones, in agreement with the fact that they induce a larger resonance shift.

In addition, also the shapes of the transmission records show large differences between 500 and 250 nm nanospheres.

For 500 nm particles, we observe that the top of the curves is relatively flat, while several dips are present in the bottom part of the plots. This behaviour can be explained by the SIBA effects previously described for the cage regime. A particle measuring 500 nm is pulled from the gradient forces in the center of the cavity hole, where it overlaps with several mode lobes (Fig. 4.11 (a)) and causes a large resonance shift. The flat top of the curves is explained by the particle size, comparable to the cavity one: the nanosphere is always pulled towards the centre of the cavity, hence overlapping with the same portion of confined field. On the other hand, the dips correspond to moments where the particle is moved away from the cavity region, as represented in Fig. 4.11 (c).

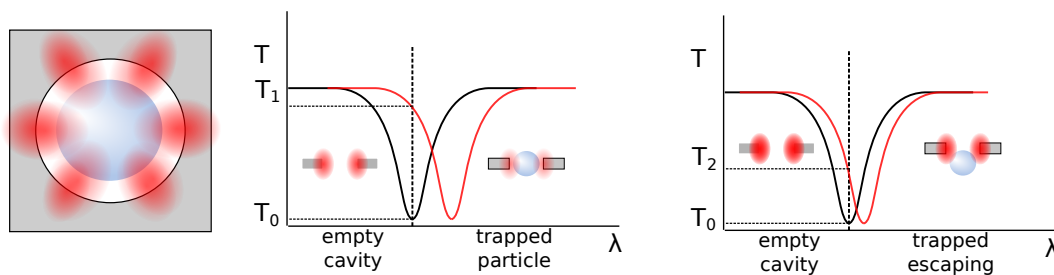


**Figure 4.11** – Qualitative analysis of the trapping of a 500 nm nanosphere. (a) The particle-size, comparable with the cavity one, results in an overlap with all the mode lobes. (b) When the particle is in the centre of the cavity the transmitted intensity is maximum. (c) While the particle moves away from the cavity region, on the contrary, the transmitted intensity decreases.

The curves recorded for the 250 nm particles, on the other hand, present a different trend. The transmission does not appear uniform during the entire trapping time; instead, there are zones with a larger transmission increase alternated to zone with a smaller one. At the same time, a difference in the fluctuations amplitude is also observed.

This behaviour can be explained by considering the size of a 250 nm nanosphere with respect to the central hole. As it is three times smaller than the cavity, only one lobe at a time is responsible for trapping, and the lobes are not equivalent. As a matter of fact, the cavity is

#### 4.4. Particle differentiation: the case of 250 and 500 nm nanospheres

excited from the side by evanescent coupling with the W1 waveguide and hence the field is not symmetric. In the cage regime, particles are re-trapped all the time, and in between “re-trappings” they move by Brownian motion. For 250 nm, it can bring them in the vicinity of a different lobe, resulting in a different resonance shift.

##### Histogram analysis

A more quantitative analysis and particle differentiation can be performed with the help of histograms. For better comparison, the transmission curves are normalized with respect to the empty cavity level and subsequently the histograms of the transmitted intensity are generated. For clarity, the relative transmission augmentation  $\Delta T_{\text{rel}}$  is considered in the following.

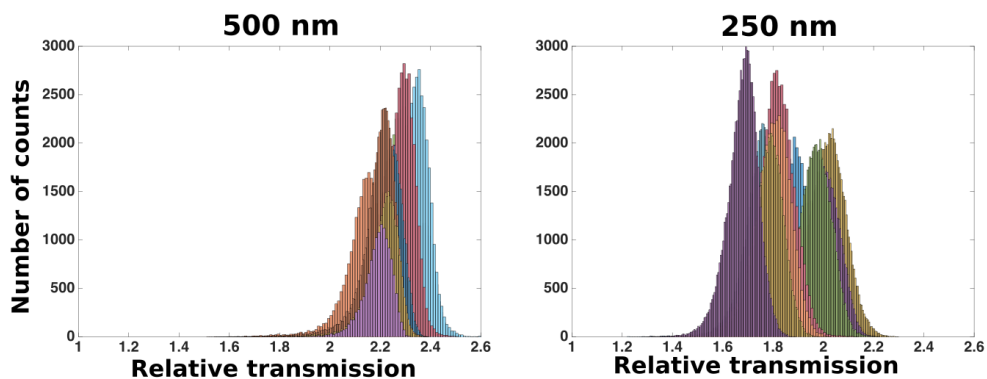


**Figure 4.12** – Histograms for the entire set of transmission measurements for polystyrene nanoparticles.

A first remark can be done while plotting together the histograms of the entire set of measurements as shown in Fig. 4.12. The different histograms for the 500 nm nanoparticles superpose almost completely, while for the 250 nm the dispersion is much larger. This behaviour is in agreement with the fact that our cavity is a more stable trap for particles that have a size comparable with the central hole: in this case, the particles are geometrically confined in a smaller volume in the PhC plane. For smaller particles, on the contrary, there is a possibility of trapping them in different positions into the cavity, leading to different induced shifts.

As expected from the observation of the plots, the average transmission increase is larger for 500 nm nanospheres than for 250 nm ones. In Fig. 4.13, only two histograms are shown for better clarity, one for each particle size. In both cases, the “mean histogram” was chosen, i.e. the histogram with the mean variance and the mean average value. With this choice, the mean shift induced by the particle is identified, as well as the average movement of the particle inside the trap. The mean relative  $\Delta T_{\text{rel}}$  for 250 nm nanoparticles is 0.86, while for 500 nm nanospheres is 1.24.

Moreover, from Fig. 4.13 it is also possible to observe that the variance of the transmission distribution appears larger for 250 nm nanoparticles. The variance of the relative transmission is linked to the motion of the particle inside the cavity and for 250 nm particles the average

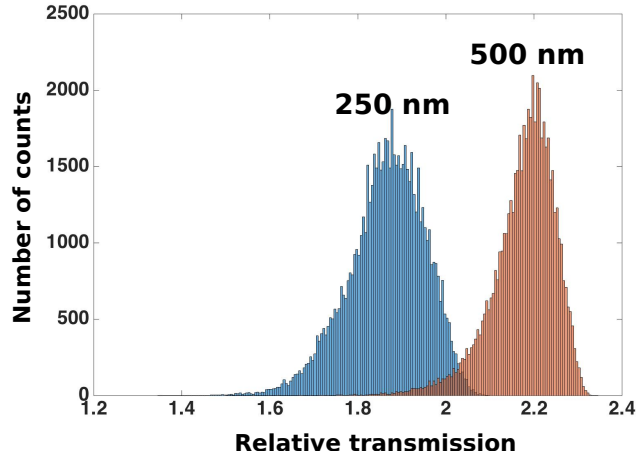


**Figure 4.13** – Average histograms for 250 and 500 nm nanoparticles. In both cases, they correspond to a transmission with the average mean value and with the average variance.

variance is 0.0053, while for 500 nm spheres it is 0.0049. This confirms that the 500 nm spheres are trapped more stably. This larger trapping stability can be observed also in Fig. 4.14 (a), where the variance of each measurement is plotted as a function of the mean  $\Delta T_{\text{rel}}$ . In a similar way to what observed in Fig. 4.12, in this case as well the 500 nm particles give results closer one to each other, revealing again a larger trapping stability.

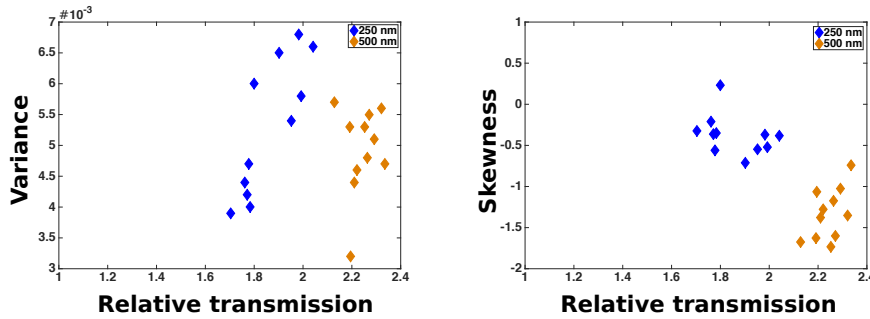


**Figure 4.14** – Variances and skewnesses plotted as a function of the mean relative transmission increment.

A last interesting remark can be done on the shape of the histograms shown in Fig. 4.13, that reflects the raw measurement plots: the histogram corresponding to 250 nm particles appears more symmetric than the one corresponding to 500 nm ones. This difference in symmetry can be evaluated by calculating the skewness of the distribution, defined as

$$s = \frac{(x - \mu)^3}{\sigma^3} \quad (4.2)$$

where  $\mu$  is the mean of  $x$  and  $\sigma$  is its standard deviation, and plotted in Fig. 4.14 (b).

A negative skew corresponds to a distribution with longer left tail, while for positive skew the

right tail is longer. In both cases, the larger the absolute value, the larger the asymmetry of the distribution. In our case, 500 nm particles present a mean skewness of -1.33, while the skewness 250 nm ones is only -0.37. This result reflects the consideration of the shape of the raw measurements, with the 500 nm exhibiting a relatively flat top and many dips in the bottom part.

Those results on the mean transmission augmentation, on its variation and on its skewness confirm the qualitative discussion carried out by the observation of the raw measurements plotted in Fig. 4.10 and allow for a quantitative support to the particle differentiation.

## 4.5 Conclusions

In this chapter, the trapping mechanisms were introduced and an application in particle differentiation was shown.

Two trapping regimes are supported by our cavity, depending on the excitation wavelength, and both can be described in terms of Self-Induced Back-Action effects: a trapped particle is an active player in the trapping dynamics, as by its presence it strongly affects the confined field. Moreover, the hollow nature of the cavity allows for a maximum interaction with the trapped objects.

In particular, the advantages of the “cage trapping” regime were shown. It corresponds to the case where the excitation wavelength is the resonance of the empty cavity and it presents two main advantages. First, the field is not acting continuously on the specimen: trapped particle causes a decoupling of the field. During the trapping it is thus a free particle in a cage, where the cage is created by the particle itself when it moves away from the cavity. Secondly, information on the trapped object can be retrieved at the same time, as the induced resonance shift depends on the properties of the particle.

As an example, the case of 250 and 500 nm polystyrene nanospheres was analysed. Particle differentiation can be achieved by simple observation of the transmission spectra, but a quantitative analysis can be carried out with the help of histograms and of the first three statistical moments: the mean, the variance and the skewness.





## 5 Bacterial Gram-type differentiation

In this chapter, results on the trapping of living bacteria and on their Gram-type differentiation are presented. The capacity to probe the cell wall of bacteria at the single-cell scale, in a label-free and non-destructive way shows the potential use of this hollow photonic crystal cavity in biological and biomedical applications.

Bacteria are unicellular prokaryotic microorganisms that are present in most of the Earth's habitats, comprised very harsh environments, like acidic hot springs [135, 136], radioactive waste underground storages [137, 138] and deep portions of the Earth's crust [139, 140], as deep as 11000 meters in the Mariana Trench [141].

They can also live in symbiotic and parasitic relationships with plants and animals. It is estimate that a 70 kg human body inhabitate  $3.8 \cdot 10^{13}$  bacterial cells, to be compared with its  $3 \cdot 10^{13}$  human cells [142]. Most of them are present in the gut flora and on the skin and are beneficial for the host [143]. However, several species of bacteria are pathogen and can cause fatal diseases: few examples are cholera (caused by some strains of the bacterium *Vibrio cholera*), tuberculosis (*Mycobacterium tuberculosis*) and bubonic plague (*Yersinia pestis*). Many others diseases more common in developed countries are caused by bacteria, going from pneumonia (*Streptococcus* and *Pseudomonas*) to foodborne illnesses (*Shigella*, *Salmonella*) and often they are treated with antibiotics, also in farming. This massive use of antibiotics, not always necessary, made the antibiotic resistance a growing problem and a challenge for the future [144, 118].

This chapter reports on the results that we obtained in the framework of a collaboration with the groups of Emmanuel Hadji, David Peyrade and Pierre Marcoux in CEA Grenoble. Its scope is the investigation of the potential use of SOI photonic crystal cavities for bacterial analysis. As a matter of fact, bacteria have a size (in the micron range) that can allow for their optical trapping with our resonant nanostructures. Moreover, a large number of non-pathogen strains are commercially available and they are simple to store and grow, permitting their use outside from biological laboratories and without special safety procedures. The experiments presented here were performed at CEA with Manon Tardif.

The main bacterial properties are first resumed. Secondly, a description of the bacteria studied is provided and the trapping capabilities of our 2D hollow photonic crystal cavity is shown. Finally, the Gram-type distinction of the seven types of living bacteria optically trapped is reported.

### 5.1 Bacterial properties

#### 5.1.1 Morphology

Bacteria can exist in several morphologies and arrangements, as shown in Fig. 5.1. The principal shapes are spheres (*cocci*) and round-ended cylinders (*bacilli*) [145], but other geometries are also possible, in particular spirals (*spirilla* and *spirochetes*). Their size is on the micron order, with typical cell volumes comprised between  $0.4$  and  $3 \mu\text{m}^3$  [146].

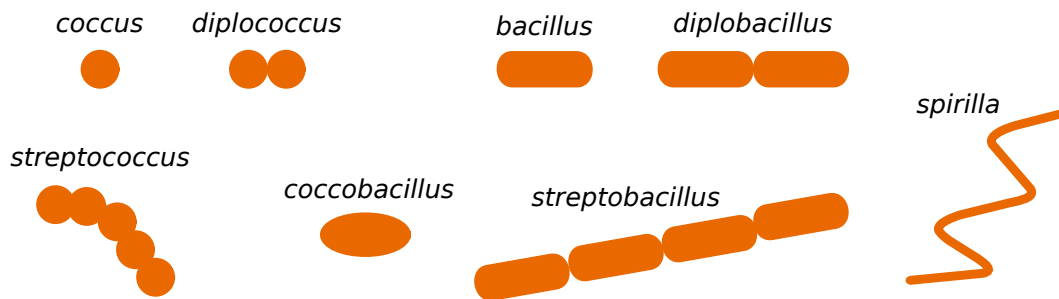


Figure 5.1 – Most common bacterial morphologies.

Moreover, the bacteria can be found free-living or attached in chains or clusters. For spherical bacteria, for instance, the arrangement in *diplococci* is common.

#### 5.1.2 Motility

Some bacteria present structures that allow them to actively move in liquid media or onto surfaces. The most important of them, especially to move in fluid environments, are flagella.

Bacterial flagella are helical filaments that run in a rotary movement, either clockwise or anticlockwise [147]. This helical motion is fundamental for propulsion of microorganisms in water: for bacteria, the Reynolds number (that correlates the inertia forces to the viscous forces) is very small, of the order of  $10^{-6}$ . This means that they live in laminar flow conditions. A consequence of that is the fact that any reciprocal motion does not result in forward displacement, due to the reversibility of Stokes flow [148]. A rotatory movement is thus necessary for bacterial swimming and allows typical speeds of 20 to  $50 \mu\text{m/s}$  [149].

Flagellated bacteria can present one or several flagella and they can be arranged in different positions, as shown in Fig. 5.2. Monotrichous bacteria have a single flagellum. Lophotrichous ones have several flagella, all connected at the same spot. Amphitrichous bacteria have two

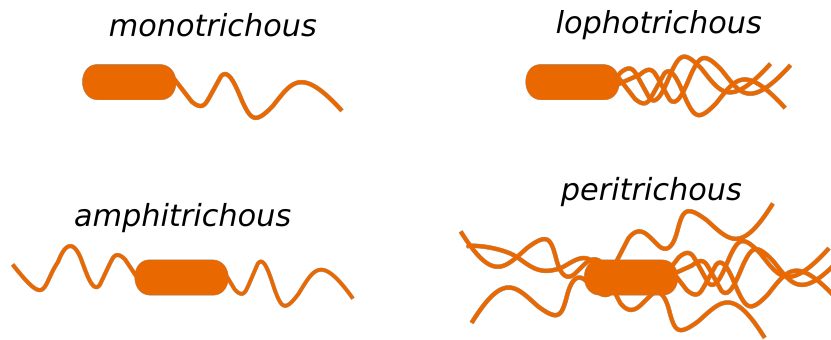


Figure 5.2 – Possible flagella arrangements.

flagella, attached to opposite extremities. Finally, peritrichous bacteria have many flagella, projecting in all directions.

### 5.1.3 Cellular membrane

Besides morphology and motility, another major parameter used to classify bacteria is the cellular membrane. Depending on the composition of their cellular membrane, bacteria can be divided in two groups, named after the technique traditionally used to differentiate them: Gram positive and Gram negative. Gram staining technique is almost always the first step in the identification of bacteria in both clinical and research environments. In particular, it has an importance in tentative diagnosis processes, as bacteria with different cell walls are also susceptible to different antibiotic treatments.

#### Gram positive and Gram negative cellular membrane

The distinction between Gram + and Gram - bacteria is based on the structural differences of their cell wall, as depicted in Fig. 5.3. A Gram negative bacterium has a much complex cell envelope [150]: two membranes are present, an inner (1 on the figure) and an outer one (4), separated by a liquid periplasmic space. The external leaflet of the outer membrane (OM) is principally composed by lipopolysaccharides, large molecules that play a critical role in the barrier function of the OM. In the periplasmic space, a thin (5 to 10 nm) layer of peptidoglycan is found. It is composed by crosslinked polymers that create a large and rigid structure and it determines the cell shape.

Gram positive bacteria, on the other hand, show a simpler structure. The outer membrane is absent but a much thicker peptidoglycan layer is present, that is composed by several layers and measures 30 to 100 nm in thickness. It protects the cell and also gives more rigidity to the cell wall.

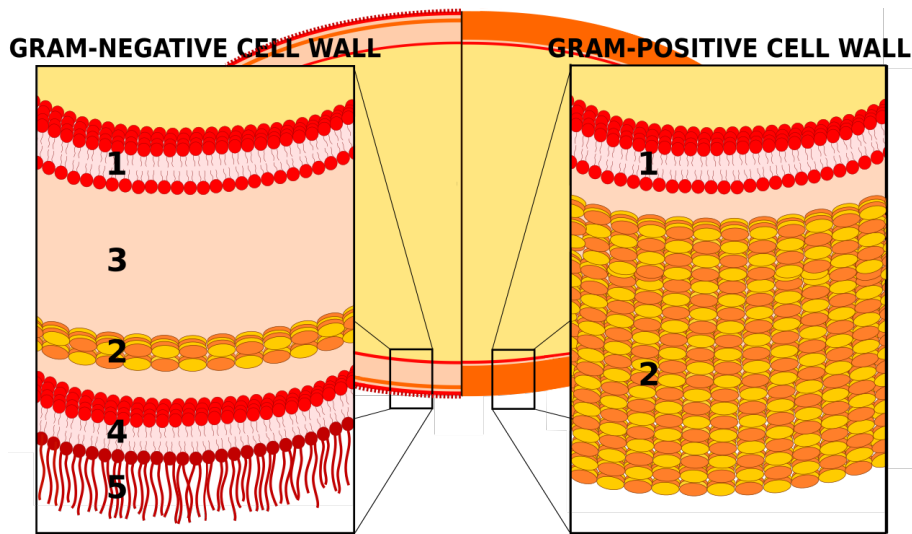


**Figure 5.3** – Schematic representation of the Gram positive and Gram negative cellular membranes. Gram - bacteria have two membranes (plasma 1 and outer 4) separated by a liquid periplasmic space (3) and a thin (5-10 nm) peptidoglycan layer (2). Moreover, lipopolysaccharides (5) project from the outer membrane. Gram + bacteria, in the contrary, exhibit a single membrane (plasma 1) surrounded by a thick (30-100 nm) peptidoglycan cell envelope. Image from Ref. [86].

### Gram staining technique

To distinguish Gram + and Gram - bacteria, the most commonly test performed in biological and clinical laboratories is the staining technique introduced by Gram in 1884 [151]. It consists in a sequence of staining and decolorisation steps [152, 153] and it basically detects the presence of the peptidoglycan layer.

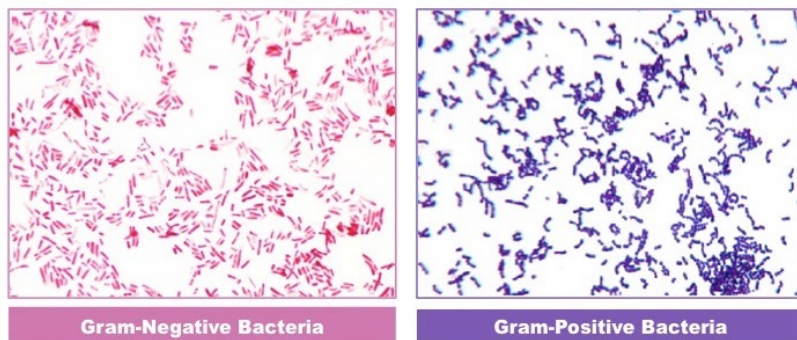


**Figure 5.4** – After the Gram staining method, Gram positive bacteria appear violet, while Gram negative ones appear pink. Image taken from Ref. [154].

Gram staining is performed as follows. Cells are first heat-fixed on a glass slide, to avoid detachment during subsequent rinsing. The first staining is applied: it consists in a water-soluble dye, crystal violet, that penetrates the cell wall of both types of bacteria. Iodine, a mordant agent, is then used. It binds with the crystal violet and traps it in the cell. At this

stage, all bacteria appear purple. A rinsing with ethanol or acetone is then performed and it affects only Gram-negative bacteria: as a matter of fact, solvents interact with the lipids of the cell membrane and destroy the outer membrane. The thin peptidoglycan layer is then left exposed and rinsed away with the outer membrane. After this step, Gram + bacteria appear purple while Gram - are colorless. Finally, a counterstaining with safranin is performed: Gram positive bacteria are still purple while Gram negatives ones are pink.

This technique is relatively simple and widely used as a first bacterial determination, useful for instance for a tentative diagnostics. However, it has some limitations: first, some bacteria cannot be identified, as there exist species that are Gram-indeterminate or Gram-variable [155]. Secondly, its use in environmental biology is limited, as it requires a biological laboratory and a large number of steps. Moreover, the test is destructive and the bacteria analysed cannot be used in subsequent studies. Finally, some of the materials used, such as crystal violet, are carcinogenic [156] and thus dangerous for the operators.

## 5.2 Bacteria studied

As all the experiments were carried out in regular optics laboratories the bacteria used belong to the biohazard Level 1, that includes organisms that are not pathogenic for humans. They were provided by P. Marcoux and consisted in reference strains (ATCC, American Type Culture Collection) purchased in lyophilised state (KwikStik, Microbiologics, St.Cloud, MN).

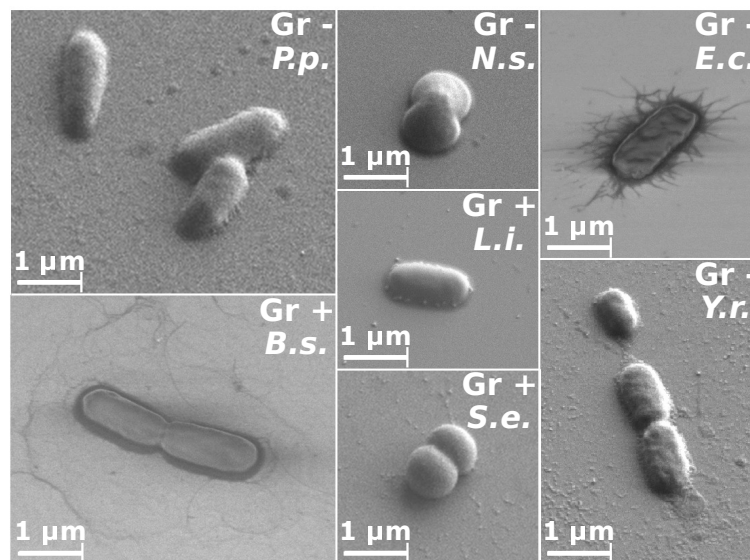


Figure 5.5 – SEM image of the bacteria studied. Reprinted from [86].

Fig. 5.5 shows SEM micrographs of the bacteria studied. Those bacteria were selected for their differences in shape (cocci or bacilli) and in motility (presence of absence of flagella, number of flagella). Moreover, for every bacterial shape at least one Gram-positive and one Gram-negative strain were chosen. In this way, the four principal categories of bacteria are

## Chapter 5. Bacterial Gram-type differentiation

represented: Gram + cocci (*Staphylococcus epidermidis*, *S.e.* on the figure), Gram - cocci (*Neisseria sicca*, *N.s.*), Gram + bacilli (*Bacillus subtilis*, *B.s.* and *Listeria innocua*, *L.i.* on the figure) and Gram - bacilli (*Escherichia coli*, *E.c.*, *Yersinia ruckeri*, *Y.r.* and *Pseudomonas putida*, *P.p.*). In addition, the biological vicinity to pathogen bacteria makes some of these bacterial species interesting for potential biomedical applications: this is the case, for instance, of *Listeria innocua*, that is close to *Listeria monocytogenes* (which is responsible for listeriosis, particularly dangerous for pregnant women) or of *Yersinia ruckeri*, close to *Yersinia enterocolitica* (that can contaminate raw pork and cause yersiniosis).

For clarity, the bacterial species used, together with their properties, are listed in Tab. 5.1.

Genus	Species	Strain	Name	Shape	Size (µm)	Gram	Flagella
<i>Neisseria</i>	<i>N. sicca</i>	ATCC 29193	NS139	Coccus	1	-	—
<i>Pseudomonas</i>	<i>P. putida</i>	ATCC 12633 ATCC 31483	PP6 PP46	Bacillus	1 x 2	-	Mono-trichous
<i>Yersinia</i>	<i>Y. ruckeri</i>	ATCC 29473	YR137	Bacillus	1 x 2	-	—
<i>Escherichia</i>	<i>E. coli</i>	ATCC 11775 ATCC 25922	EC28 EC10	Bacillus	1 x 2	-	Peri-trichous
<i>Bacillus</i>	<i>B. subtilis</i>	ATCC 11774	BS134	Bacillus	1 x 3	+	Peri-trichous
<i>Listeria</i>	<i>L. innocua</i>	ATCC 33090	LI142	Bacillus	1 x 2	+	Amphi-trichous
<i>Staphylococcus</i>	<i>S. epidermidis</i>	ATCC 14990 ATCC 12228	SE9 SE26	Coccus	1	+	—

**Table 5.1** – List of the bacteria studied and of their properties. Genus, species and strain are reported, together with the name that we use to identify them. The morphological parameters, the Gram-type and the their classification with respect to the motility is also presented.

### 5.3 Trapping capabilities

In this section, we will investigate the capabilities of our 2D hollow PhC cavity in optical trapping of living bacteria. The measurements were performed at CEA Grenoble and the experimental procedure is very similar to the one described in Sec. 4.4 for the polystyrene nanospheres. The two major differences consist in the bacteria sample preparation and in the use of the “swimming pool” configuration instead of the microfluidic channels.

#### 5.3.1 Bacterial preparation

To perform optical trapping experiments with living bacteria, three requirements have to be fulfilled: first, the viability of the specimen has to be ensured. Secondly, the purity of the microorganisms culture has to be maintained. Third, to allow for a meaningful comparison, the bacteria studied have to be used in a phase where small variations between the different cells are present.

### 5.3. Trapping capabilities

As mentioned in the introduction to section 5.2, the reference strains that we use are purchased in lyophilised state. Lyophilisation, or freeze-drying, is a process where water is removed from a frozen specimen by sublimation [157, 158] and it is the technique most frequently used by culture collection centres. Under these conditions, bacteria go into a dormant state and their viability is maintained for several years, up to 50 [159, 160]. After unfreezing, bacterial strains are maintained by periodic transfer to fresh media: a culture is performed on a nutrient agar medium (in our case on the prepared Petri dishes described in section 3.2.2, as shown Fig. 5.6) and it can be stored in a refrigerator at 0-4 °C for 3 weeks. During this time, the metabolic activities of the bacteria are slowed down but not stopped and they slowly continue to grow, using the nutrients and producing waste products. Naturally, to maintain the monoculture it is mandatory that the environment where the culture steps are performed is sterile.



**Figure 5.6** – *Escherichia coli* culture on a Columbia Blood Agar prepared Petri dish.

The transfer method is a simple and cheap way to conserve bacterial strains in a *almost* ready-to-use state. However, the transfer method does not maintain the purity of the culture over long times, as with subsequent duplications variants and mutants develop. To consider the bacteria used identical to the reference strain, a maximum of 8 culture steps are allowed. After that, it is necessary to restart from the lyophilised ones.

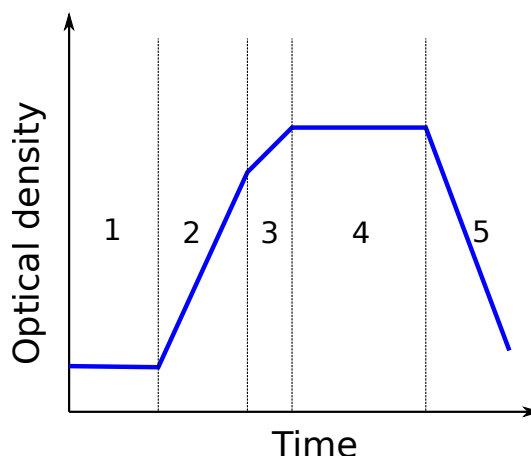


**Figure 5.7** – Bacterial growth curve.

Finally, during their growth process the bacteria undergo different phases. As it is desirable

## Chapter 5. Bacterial Gram-type differentiation

---

to operate on cells in a similar state, the growth curve of a bacterium has to be introduced. Bacteria duplicate by cell division and when measuring the optical density (or counting the colony forming units) as a function of time, several regions can be observed. They are schematically represented in Fig. 5.7 and can be described as follows:

- When transferred onto a fresh culture media, bacteria adapt to the growth conditions. During this phase, called lag phase, enzymes and products [161] necessary the subsequent cell division are prepared. Cells are metabolically active and grow in size but they do not duplicate.
- In the second phase, called exponential phase, the bacteria duplication occurs and their population exponentially increases.
- The third phase corresponds to a situation where the growth speed is reduced, due to arising limiting growth factors such as the nutritive elements depletion and the accumulation of waste products.
- During the stationary phase, an equilibrium between duplicating bacteria and bacteria that undergo cell lysis is reached. Bacteria lysis is caused by enzymes produced by the cells themselves (autolysins) which hydrolyse the mucopeptide polymers in the bacterial cell wall [162, 163].
- Finally, during the death phase, most of the bacteria lose their viability, dead bacteria cells undergo autolysis and the bacterial population decreases exponentially.

Bacteria in the exponential phase are the healthiest and most uniform. Therefore, most of the experiments in microbiology are carried out during this phase, that has a duration of the order of 12 hours. Usually, the bacteria transfer onto a nutritive medium is done in the late afternoon, just before leaving the laboratory. They are then let to incubate overnight at 37 °C and the morning after they are ready to use. To ensure the use of bacteria in the same conditions, cultures are repeated every day, always starting from the same culture.

After growing on a solid nutritive medium, the cells are organised in colonies and form a biofilm. Bacteria are embedded in a adherent extracellular matrix composed typically by polymeric conglomeration of polysaccharides, proteins, lipids and DNA [164]. To perform optical trapping experiments, a small quantity of those bacteria is collected from the Petri dish and suspended in 5 mL of de-ionised water filtered at 2 µm to avoid any contamination by larger objects. An intense mixing (at least one minute in a shaker) is required to separate the bacteria and obtain suspended single cells. As the experiments were carried out in the laboratories of CEA, the “swimming pool” configuration was used and the bacteria concentration that we selected was high: 3 McF (McFarland Standard)<sup>1</sup>, corresponding to a cell density of 10<sup>9</sup> cfu/mL.

---

<sup>1</sup>McFarland Standards are used as a reference to adjust the turbidity of a bacterial suspension. [McFarland standards page on wikipedia: [https://en.wikipedia.org/wiki/McFarland\\_standards](https://en.wikipedia.org/wiki/McFarland_standards)]



### 5.3.2 Experimental procedure

The experimental procedure is very similar to the one described for optical trapping of polystyrene nanospheres in section 4.4 and the experimental setup is illustrated in Fig. 5.8.

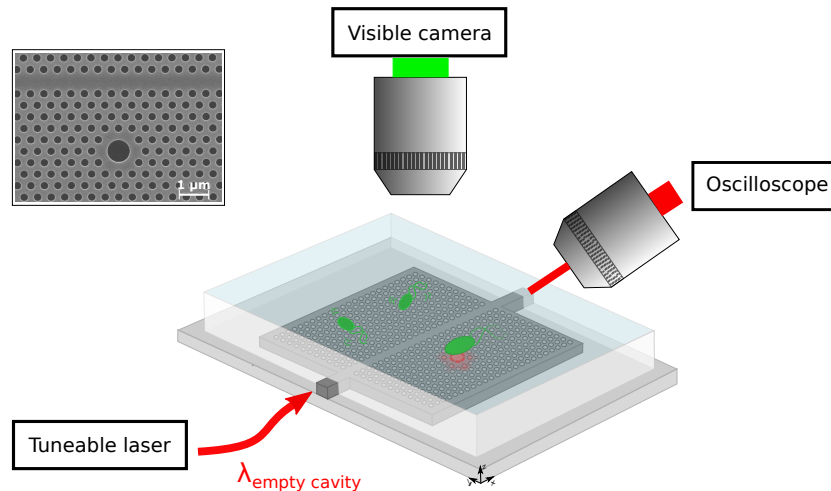


**Figure 5.8** – Experimental setup used for bacterial optical trapping and differentiation in Grenoble.

For these experiments, the “swimming pool” configuration was used. In this configuration, the sample is first prepared by creating a 100 μm thick PDMS frame and by filling it with a drop of bacterial suspension (5 μL). The chip is then covered with a glass coverslip and mounted on the sample holder. After use, the “swimming pool” can simply be removed from the chip and the sample is rinsed with de-ionised water and dried with compressed nitrogen. The operation takes a few minutes and another suspension can be immediately used.

Light from a tuneable laser (Tunics, Yenista Optics) is injected with a lensed fiber and its polarisation is controlled with a paddle polarisation controller. The intensity transmitted through the sample is collected with a microscope objective and a digital oscilloscope (CT400 Yenista Optics) records the transmission. A Sony *a7S* camera is used for imaging and the resonance frequency is determined by detecting the minimum in transmission, corresponding to the cavity excitation.

Before starting the trapping operations, a characterisation of the cavities was performed. The same cavity was used for the entire set of experiments, to ensure response uniformity. It had a quality factor of 4500 and a resonance wavelength of 1526.7 nm in water. The shift in the eigenmode with respect to the one in air was of only 12.5 nm, to be compared with the usual 35 nm. This value suggested that in the “swimming pool” configuration the photonic crystal membrane was not surrounded by water but only covered on the top. This can be explained by the fact that the silicon surface is naturally hydrophobic. Without an external overpressure as the one that we induce with our channels, the liquid does not fill the holes. Nevertheless, optical trapping of bacteria was still possible on top of the cavity, as it will be detailed in the following sections.

## Chapter 5. Bacterial Gram-type differentiation

In addition, a second tuneable laser was used for some of the strains studied, to detect the shift induced in the resonance frequency by trapped bacteria. One laser, at a power of 10 mW, was injected with a 50:50 fiber coupler at the empty cavity resonance wavelength and was responsible for optical trapping. The second one, injected in the other input port of the coupler and with a power of 1 mW, scanned a few nanometers range of wavelengths around the eigenmode.

### 5.3.3 Minimum trapping power

For every bacterial strain studied, the first question was if it was possible to trap them with our cavity, and if so, with which power. This question was pertinent also to compare the trapping capabilities of our device with respect to the optical cavity used by the groups in Grenoble, with the chance to test two different devices on the same optical setup. As a matter of fact, in the last ten years a 1D silicon photonic crystal cavity was developed (Fig. 5.9 (a)) that allowed for optical trapping and differentiation of three bacterial species, i.e. *E. coli*, *B. subtilis* and *S. epidermidis* [87] (Fig. 5.9 (b)). However, the trapping of some other species, such as *N. sicca* or *L. innocua* was impossible.

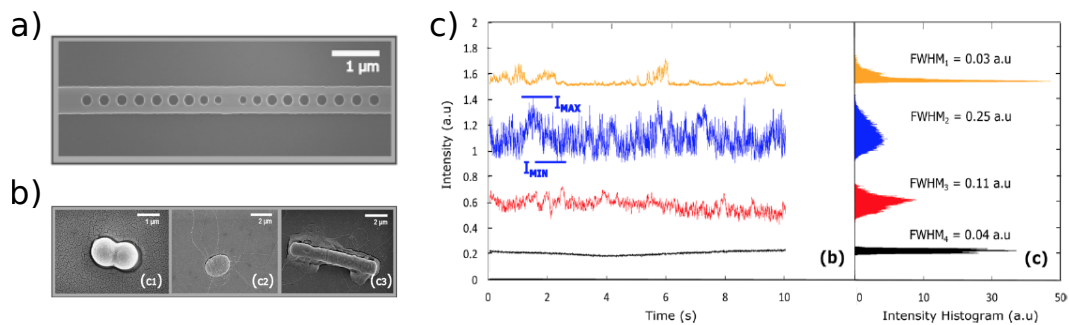


**Figure 5.9** – (a) SEM image of a 1D photonic crystal cavity used by the group at CEA. (b) SEM picture of the bacteria studied: *E.coli*, *S. epidermidis* and *B. subtilis*. (c) Identification of the three bacteria was achieved by transmission analysis. Image adapted from Ref. [87].

On our sample, we tested all the bacteria listed in Tab. 5.1 and it was possible to trap all the seven types, including all the different strains.

For every bacterial strain, we started optical trapping experiments injecting the maximum available power, 10 mW, at the empty cavity resonance wavelength and by recording the corresponding transmission. The power was then decreased by 2 mW steps until optical trapping was not possible anymore. Moreover, for every power tested, we checked if the cavity was able to trap autonomously, by turning off and on the laser again in a sequence that we called trapping/untrapping/retrapping.

A typical transmission curve, showing the transmission increment caused by the resonance shift, is plotted in Fig. 5.10. This curve was measured for *Yersinia ruckeri* trapped with an injected power of 8 mW. We can observe that optical trapping occurred immediately after

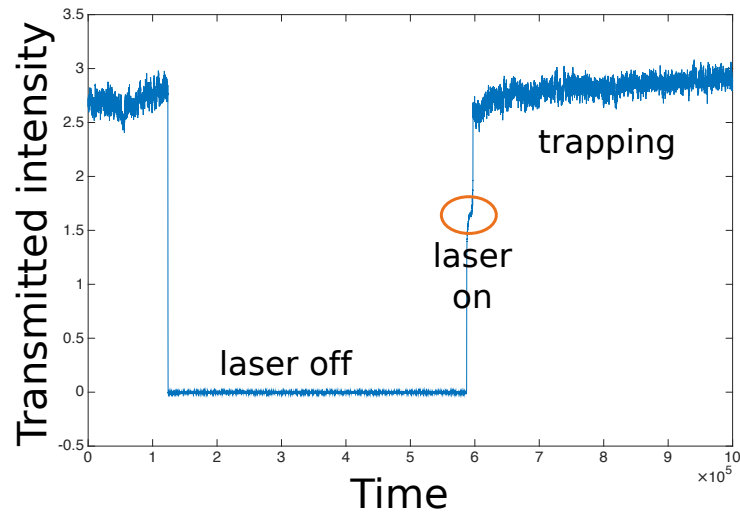


**Figure 5.10** – Transmission curve for the trapping of *Yersinia ruckeri* with an injected power of 8 mW. Bacteria are first trapped, corresponding to a high transmitted intensity. The laser is then turned off and on again and optical trapping immediately occurs.

turning on the laser again: the bacteria concentration was high, resulting in many bacteria close to the cavity region and exposed to the gradient forces of the confined field. An injected power of 8 mW was largely sufficiently to allow for the trapping of all the bacterial species.

Indeed, injected powers down to 4 mW showed to be sufficient for stable trapping, as shown in Fig. 5.11.

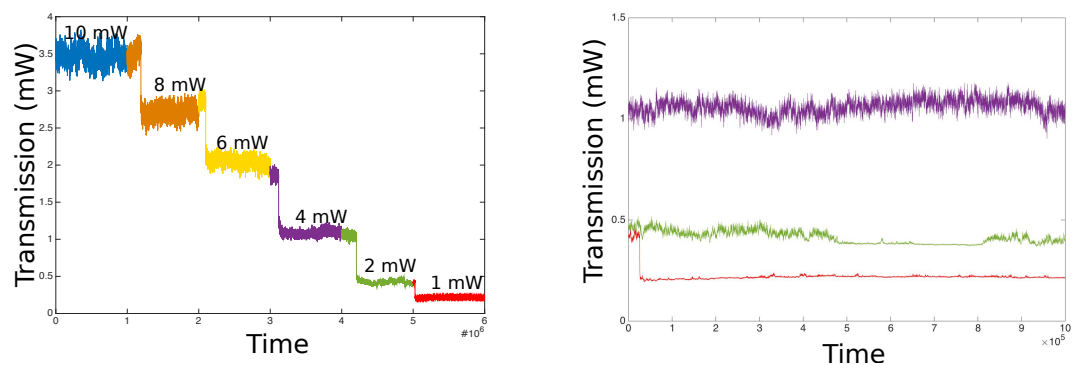


**Figure 5.11** – (a) Transmitted intensity for the trapping of *Yersinia ruckeri* as a function of time for several injected powers, going from 10 mW to 1 mW. Trapping is stable down to 4 mW. (b) The curves for 4, 2 and 1 mW are plotted together. Trapping is stable for 4 mW, not stable for 2 mW and only few interactions between the bacteria and the confined field occur for 1 mW of injected power.

In Fig. 5.11 (a) the curves corresponding to the trapping at different powers are plotted in sequence, while in Fig. 5.11 (b) the transmissions recorded for trapping at 4 mW, 2 mW and 1 mW are plotted together for better comparison of the trapping signatures.

## Chapter 5. Bacterial Gram-type differentiation

In Fig. 5.11 (a) different colours correspond to different measurements, each 50 s long. The laser was first turned on at 10 mW and, as soon as bacteria were trapped, the transmission was recorded. After this first record, a cycle of trapping/untrapping/retrapping was done, to assess the autonomous trapping at this power. After that, while still having bacteria trapped in the cavity with 10 mW, a new transmission record was performed and the power was decreased to 8 mW. And so on down to 1 mW. For the same injected power, the two colours correspond to measurements performed at a distance of few minutes and trapping different bacteria; it is interesting to observe that the transmitted intensity for the same power is very similar, showing a good stability of the system.

As it was shown for nanoparticles in Chap. 4, besides the transmission increase, stable trapping can be detected by amplitude fluctuations due to particle movement that are large with respect to the empty cavity level. In this case, those variations are present and with a uniform amplitude for the curves down to 4 mW, confirming stable trapping. In the example of 2 mW, on the contrary, bacteria were trapped only from 0 to 25 seconds and again from 35 to 50 s. Finally, for 1 mW of injected power only few interactions with the confined field were observed, but trapping was not possible.

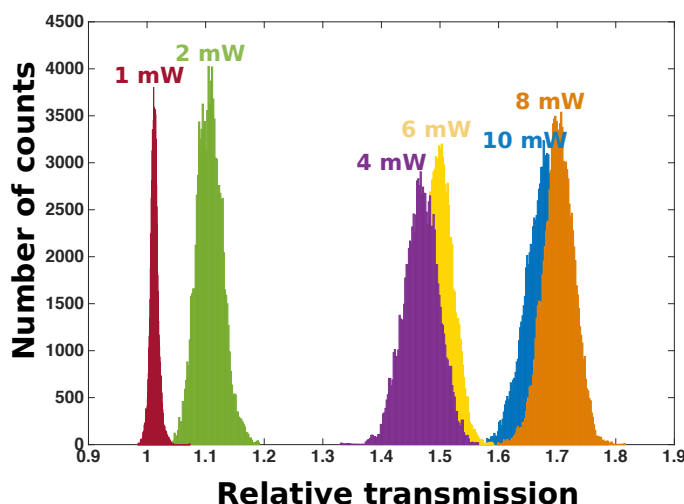


**Figure 5.12** – Histograms of relative transmission increment for the same bacterial species, *Yersinia ruckeri*, and different injected powers.

This behaviour can be retrieved also in the histogram analysis, showed in Fig. 5.12. After normalisation with respect to the empty cavity transmission level, the histograms of the transmitted intensities are plotted. Histograms corresponding to powers comprised between 4 and 10 mW exhibit a mean relative transmission augmentation larger than 0.4, and as it will be shown in Section 5.4 it is consistent with the shift induced by a Gram negative bacterium like *Yersinia ruckeri*. The large variability between the measurements will also be explained in next section.

On the other side, the histograms for 1 and 2 mW confirm the conclusions drawn from trans-

## 5.4. Bacterial Gram-type distinction

mission curves observation: the histogram corresponding to 1 mW only slightly differs from the histogram corresponding to an empty cavity transmission. In particular, the mean value of the transmission augmentation is only 0.01 and the variance is  $0.05 \cdot 10^{-3}$ , to be compared with the average  $0.1 \cdot 10^{-3}$  of the histograms for larger powers.

Optical trapping of all the bacteria tested was possible and the lowest trapping powers for every bacteria type are collected in Tab. 5.2. By referring to Fig. 4.3, the corresponding estimated powers guided into the W1 waveguide are comprised between 250 and 400  $\mu$ W.

In conclusion, the use of our cavity appears appealing for bacterial analysis: trapping was possible with very low powers for all the specimen tested and the SIBA effects that our system support can provide information to identify bacteria or to determine their viability. All this information can be acquired at the single cell level and in a fast and non destructive way. In the following section, the application to Gram-type determination is showed.

<b>Bacteria</b>	<b>Minimun trapping power injected(mW)/estimated(<math>\mu</math>W)</b>
<i>N. sicca</i>	6 / 400
<i>P. putida</i>	4 / 250
<i>Y. ruckeri</i>	4 / 250
<i>E. coli</i>	4 / 250
<i>B. subtilis</i>	4 / 250
<i>L. innocua</i>	6 / 400
<i>S. epidermidis</i>	6 / 400

**Table 5.2** – Minimal powers necessary for stable bacteria trapping. The laser power is reported together with the estimated power guided in the vicinity of the W1 waveguide, as explained in Section 4.1.3.

## 5.4 Bacterial Gram-type distinction

Once assessed the trapping capabilities of our cavity, the objective of the experiments was to obtain information on the trapped bacteria by analysing the transmission curves. We used the same cavity described in the previous section ( $Q = 4500$ , resonance wavelength at 1526.7 nm) and we used a trapping power of 10 mW in the cage regime, i.e. by injecting light at the empty cavity resonance wavelength. Moreover, to take into account variations in the bacteria population and in their overlap with the confined mode, at least 10 measurements for every bacterial strain were performed. Every measurements lasted for at least 5 seconds and then the laser was turned off, some time was let for bacteria to move away by Brownian motion and for new ones to arrive close to the cavity region. The laser was turned on again and the procedure was repeated 10 times. For better comparison, during the data analysis every curve was normalised with respect to the empty cavity level.

## 5.4.1 Gram-type differentiation

In a similar way to what was observed for polystyrene nanoparticles of different sizes, bacteria-dependent differences in the transmitted intensities were monitored and the most evident variation between curves consisted in different mean transmission augmentations, related to different induced resonance shifts.

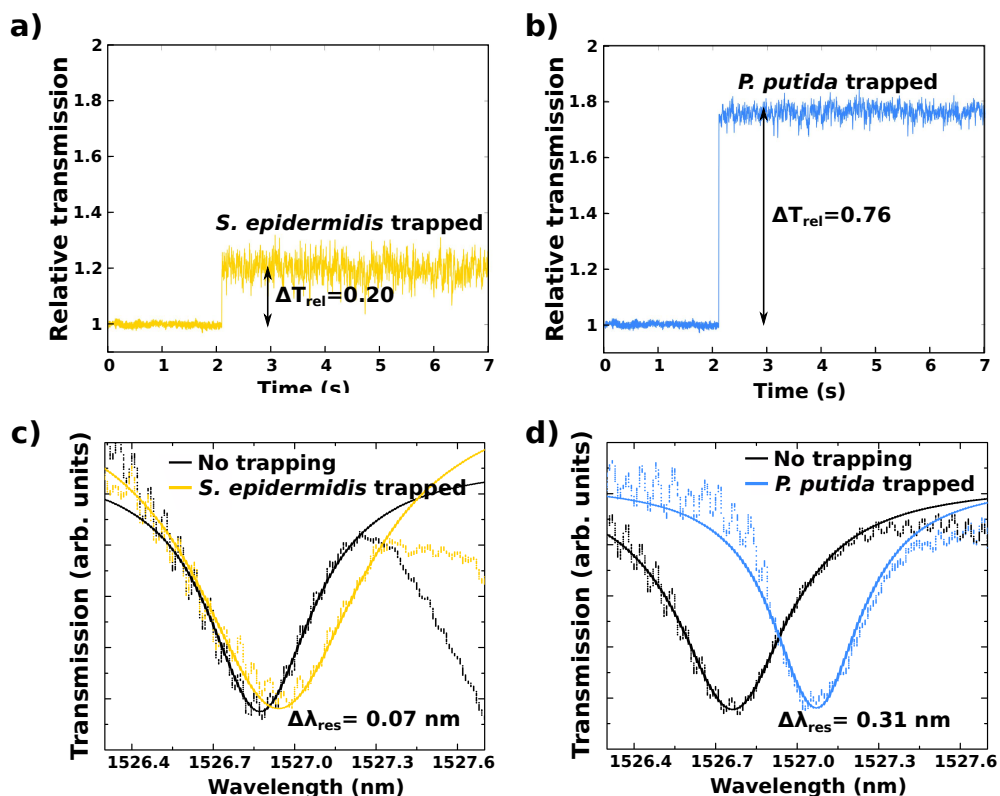


**Figure 5.13** – (a) Minimum relative transmission augmentation for *S. epidermidis*, a Gram + coccus. (b) Maximum  $\Delta T_{rel}$  observed for *P. putida*, a Gram - bacillus. (c) and (d) The corresponding resonance wavelength shift are measured. Image adapted from Ref. [86].

In Fig. 5.13 (a) and (b) are plotted the relative transmissions corresponding to the minimum and to the maximum  $\Delta T_{rel}$  measured on the entire experimental set. The corresponding resonance wavelength shift is also presented in Fig. 5.13 (c) and (d). Those curves correspond to different bacteria. The minimum shift in the resonance wavelength was induced by *S. epidermidis*, a Gram positive coccus. It was of 0.07 nm and resulted in a  $\Delta T_{rel}$  of 0.20. On the contrary, the maximum shift observed (0.31 nm) was induced by *P. putida*, a Gram negative bacillus. It corresponded to a variation in relative transmission of 0.76.

By plotting the mean value of the relative transmission increase for all the measurements performed (Fig. 5.14), the same trend is highlighted: Gram negative bacteria exhibit a larger transmission augmentation than Gram positive ones. In particular, for this optical cavity a demarcation around  $\Delta T_{rel} = 0.4$  appears. Despite a very large variation in the values obtained

#### 5.4. Bacterial Gram-type distinction

for every bacterial species, this demarcation is never crossed and Gram type determination is possible without ambiguity for the entire experimental set. Moreover, it has to be noted that the measurements plotted in Fig. 5.14 were performed in 3 different days, over a period of 5 months, proving the robustness of the response over time and over different bacteria cultures. For this analysis, we considered only bacterial species. Referring to Tab. 5.1, we used SE26 for *S. epidermidis*, PP46 for *P. putida* and EC28 for *E. coli*.

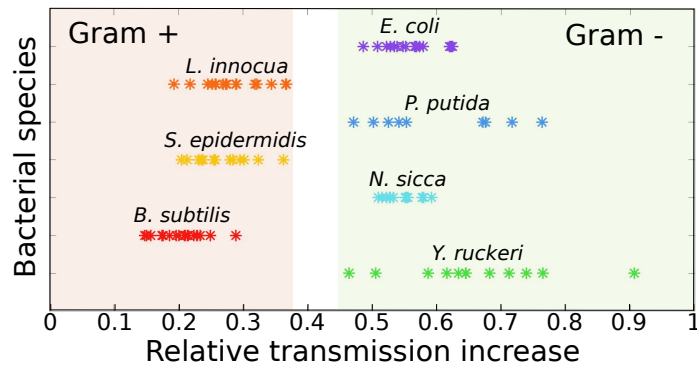


**Figure 5.14** – The mean transmission increase for all the measurements performed are plotted. Despite a large variation of  $\Delta T_{rel}$  for every bacterial strain, Gram + and Gram - bacteria create two distinct groups, with the Gram negative ones exhibiting a larger transmission augmentation.

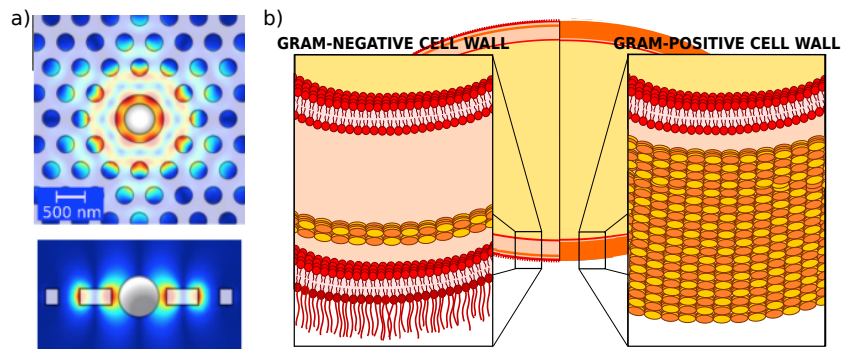


**Figure 5.15** – (a) FEM simulation of the field confined into the cavity. It extends over a distance of the order of 100 nm from the silicon surface, which is also the thickness order of the bacterial cell wall (b). Image adapted from Ref. [25] and [86].

This strong dependence on the cell wall properties of the bacteria can be explained by considering the properties of the confined cavity field and of the cell walls themselves, reported in Fig. 5.15 for clarity. Bacteria cell wall has a thickness of the order of 80-100 nm. It is thus the part of the cell that interacts more with the confined field, which extends in the hollow volume for a distance of the order of 100 nm. Moreover, it has to be noted that several bacteria (6 to 10) were simultaneously trapped on the optical cavity, maximising the overlap with the confined field.

When considering the difference in response for the two types of cell wall, the larger resonance shift induced by the Gram negative bacteria with respect to the Gram positive ones can be

## Chapter 5. Bacterial Gram-type differentiation

explained by two factors: first, the cell deformability plays a central role. As it was mentioned before, the peptidoglycan layers create the rigid structure of the cell. For Gram + , this layer is very thick (up to 100 nm), while for Gram - ones it is much thinner, measuring only 5-10 nm. Moreover, Gram negative bacteria present a liquid periplasmic space between the two cellular membranes. Gram - bacteria can thus deform more [150, 165] and hence overlap to a larger extent with the confined mode. Moreover, the lipopolysaccharides can also play an important role: they are large molecules that project only from the Gram negative outer membrane. Their large refractive index could result in a contribution in the larger resonance shift.

Finally, few remarks on the large variations in the mean  $\Delta T_{rel}$  shown in Fig. 5.14. First, the intrinsic phenotypic variability of the bacterial population (in size and shape for instance) is certainly responsible for those differences. Secondly, the number, the orientation and the position with the trapping field can also cause variations in the response: indeed, diversities in those parameters result in different overlaps with the confined field. Nevertheless, those differences do not prevent the bacterial Gram-type distinction: for instance, for every bacterial Gram-type at least one coccus and one bacillus was selected. In this case, the shape difference is large, but the Gram-type determination is still achieved.

### 5.4.2 Bacteria identification

As the mean value of the transmitted intensity increase allowed for Gram-type distinction, it is natural to wonder if more information can be retrieved by the trapping curves, that could for instance allow for bacterial identification.

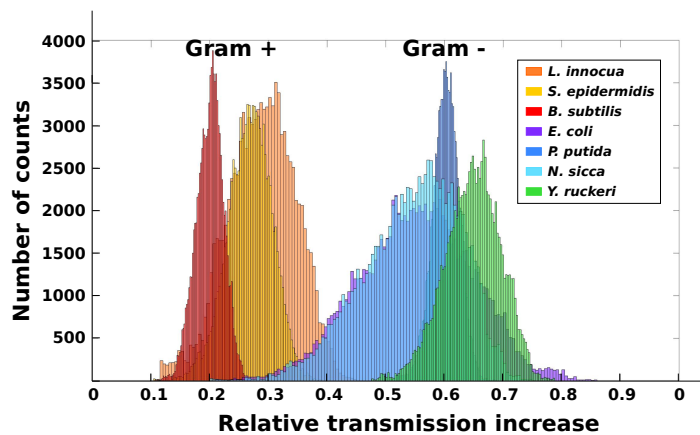


**Figure 5.16** – Mean histograms for the seven types of bacteria studied. For each strain, histograms for all the measurements were calculated and the mean and the variance were obtained. The histograms plotted here have the mean  $\Delta T_{rel}$  and the mean variance for every strain. Image from Ref. [86].

A first tentative response can be given by observing the histograms functions of the curves. In Fig. 5.16, the “mean histograms” are plotted. For every bacterial strain, the histograms corresponding to all the measurements were first plotted. The mean  $\Delta T_{rel}$  induced by that



## 5.4. Bacterial Gram-type distinction

particular bacterium and the mean transmission variance were then obtained. Finally, the histograms with the mean  $\Delta T_{rel}$  and the mean variance were plotted.

For some bacteria, identification is possible to a certain extent. For instance, *B. subtilis* shows a smaller variance with respect to other Gram + bacteria, and the same happens for *P. putida* in the Gram - group, but for the other bacteria differences are not so evident.

To go further with the analysis, calculations on the distance between the transmission curves of different bacteria were performed, in a signal analysis approach. The relative distance between two signals  $f$  and  $g$  is defined as

$$d(f, g) = \min_{0 \leq \tau \leq T} \sqrt{\int_0^T dt |f(t) - g(t - \tau)|^2} \quad (5.1)$$

and the results are shown in Fig. 5.17.

Both strains for *S. epidermidis* were considered. From the distance calculations, we observe that the Gram + / Gram - distinction is retrieved. Other bacteria clusters, on the other hand, are not evident: the parameter that impacts more in the reciprocal distance between curves is the mean transmission increase.

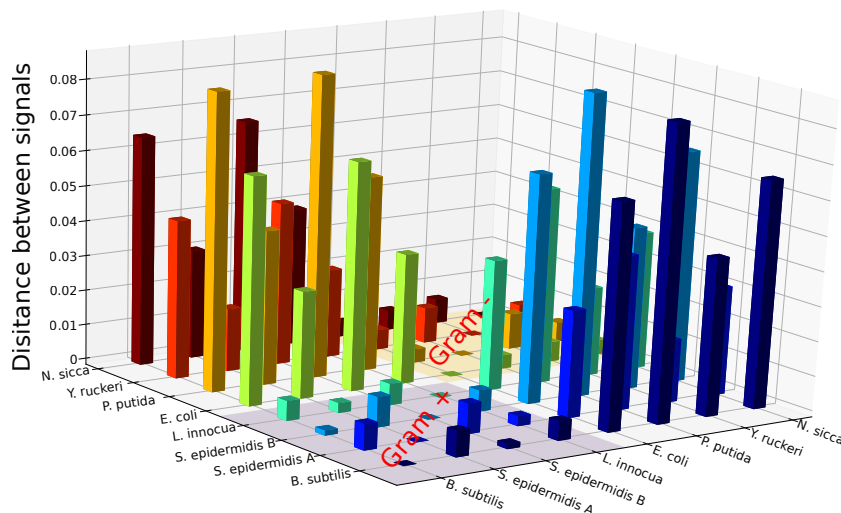


**Figure 5.17** – Distances between the transmission curves for all the bacteria studied.

The dispersion of the mean values and the standard deviations of the transmission curves are also interesting parameters to analyse. In Fig. 5.18 the standard deviations ( $\sigma$ ) of every transmission curve are plotted as a function of the mean transmission increase ( $\mu$ ). For every bacterial strain, the standard deviations for  $\sigma$  and  $\mu$  were also calculated and they are represented by ellipses. A clear bacterial identification is not possible yet, but the Gram-type determination is achieved unambiguously for all the bacterial strains investigated and some kind of clustering appears in the  $\mu$ - $\sigma$  plane.

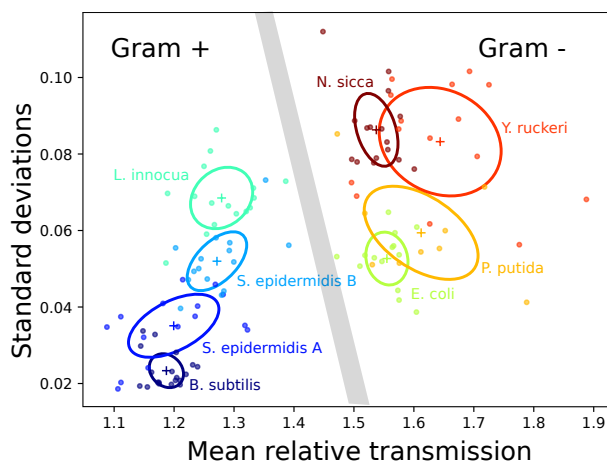


**Figure 5.18** – Standard deviations ( $\sigma$ ) of all the measurements with respect to  $\Delta T_{\text{rel}}$  ( $\mu$ ). The standard deviations of both  $\sigma$  and  $\mu$  for every bacterial strain are highlighted by ellipses.

The third and fourth statistical moments (the skewness and the kurtosis) were also calculated, but trends allowing for further bacterial differentiation were not observed.

However, this kind of analysis appears very promising for the future. To support this idea, it is important to note that we were working at high bacteria concentration and that several bacteria were trapped simultaneously on the optical cavity. This resulted in a maximum of overlap between the bacteria cell walls and the cavity mode, leading to clear Gram type determination. However, at the same time, the contributions due to single bacterium characteristics (size, shape or motility) were averaged by the large number of cells. For the future, experiments with single bacteria are scheduled and improvements in bacterial identification appear possible.

## 5.5 Conclusions

This chapter reports on the exploitation of the SIBA effects supported by our cavity for bacterial analysis. All the bacteria tested were successfully trapped and it was possible to unambiguously determine their Gram type with a transmission measurement. Thanks to the hollow geometry, large interactions occur between the cavity field and bacteria and their trapping with ultra-low powers, on the order of few hundreds of microwatts, is possible without any damage to the cells.

Gram-negative bacteria showed to cause a larger resonance shift with respect to the one induced by Gram-positive species, most probably due to the larger deformability of their cell wall, that can thus overlap with the confined field to a larger extent. Moreover, this cavity appears a promising candidate for further bacterial identification. With this results we show that the cell wall is especially probed with our system, and it opens the route to a series of exciting experiments involving cellular membranes.

## 6 Conclusions and perspectives

The work presented here continues the project carried out in these last years on the investigation of the properties of a two-dimensional hollow photonic crystal cavity. In particular, the objective of this thesis was to assess its potential use in biological applications. It was possible to trap all the bacterial species investigated and their Gram-type was determined unambiguously. With further optimisation, our optofluidic chip appears thus a convincing candidate for integrated biological analysis.

To achieve this result, three main steps were identified: first, the fabrication of good quality photonic crystal structures and the development of a “bacteria-friendly” setup were fundamental. Second, polystyrene nanoparticles (which are easier to trap because of their larger refractive index) were used to appraise that it is possible to distinguish particles by simple transmission measurements. This mechanism was indeed expected from the SIBA effects that are supported by our cavity. Finally, optical trapping experiments involving bacteria were carried out in the framework of a collaboration with the groups of Pierre Marcoux, Emmanuel Hadji and David Peyrade in CEA Grenoble.

The fabrication of the optofluidic chip was done at IPHYS and CMi cleanrooms and the entire process was carried out, from the photonic crystal fabrication to its integration with microfluidic layers. The main challenges consisted in the obtaining of structures with good quality factors and light transmission properties. In this sense, the limitation of losses due to fabrication defects was crucial and in every step optimisations were carried out. They allowed for obtaining typical quality factors of the order of 9000-10000 and the transmission intensity values were increased by a factor of five with respect of previous samples. Moreover, the development of SU8 mode adaptors allowed for a further increase in the light transmission.

Bacteria manipulation in microfluidic environment showed some additional difficulties with respect to nanoparticles. Their size, in the few-microns range, together with their tendency to attach to surfaces makes the use of microfluidic channels more difficult and fragile, as blockages in the channels are more likely to happen. The thickness of the transport channel was increased from 10  $\mu\text{m}$  to 20  $\mu\text{m}$ , but blockages were observed that led to the breaking of

## Chapter 6. Conclusions and perspectives

---

the channels. In particular, the critical points are the Quake valves: to allow for a complete closing of the channel, larger pressures were injected in the glass channels that caused the breaking of the thin PDMS membrane. To overcome these adhesion problems, BSA treatment could be a solution that needs to be tested in the future. The “swimming pool” configuration proved to be a simple and excellent solution for the trapping of bacteria at high concentration, but when conceiving more complex experiments it appears too limiting. For instance, it would be of great interest to perform an experiment consisting in the trapping of a bacterium and in the subsequent injection of an antibiotic. For this purpose, a microfluidics containing two injection channels was developed and the switch between liquids was observed. However, due to the fragilities described beforehand, the testing on bacteria analysis was not possible during the available time.

On the other hand, the experimental setup was also modified to enable experiments carried out at different temperatures and for longer times. A Peltier module was integrated to the sample holder and its mechanical stability was increased, to allow for stable coupling between the lensed fibers and the sample waveguides for several tenths of minutes.

Considering the trapping capabilities of the system, optical trapping is shown with ultra-low powers (of the order of few hundreds of microwatts) for 250 and 500 nm polystyrene nanoparticles and for seven types of bacteria. Due to their size with respect to the cavity hole (700 nm in diameter), the nanospheres were trapped inside the central volume, while the bacteria were trapped on top of the cavity. The trapping is more stable for specimen with sizes comparable to the one of the central hole, as the objects can overlap with all the mode lobes. Moreover, a free Brownian motion is possible only in the direction perpendicular to the plane of the crystal. For the future, it is conceivable to exploit the scaling properties of photonic crystals to create cavities adapted to different sizes, while conserving this mode profile and especially its large overlap with the hollow medium. For instance, the system could be scaled down by a factor of three (thus obtaining a central hole of  $\approx 200$  nm) using materials that can operate in the visible, such as III-Nitrides. This could be particularly suitable for the trapping of viruses (their size is in the 100 nm range) and of large biomolecules. On the other hand, a cavity doubled in size could contain bacteria and it could still be realised in silicon. The defect modes could be excited by lasers operating in the 3-5 microns range, such as Quantum Cascade Lasers (QCL), or lasers using Cr:ZnSe/s or Fe:ZnSe/S as a gain medium.

In all the experiments, the “cage trapping regime” was exploited. As the “classical regime”, it arises from the Self-Induced Back-Action effects, that consist in an active role of the specimen in the trapping dynamics. In the cage regime, the cavity is excited at its resonance frequency and a trapped objects causes a redshift of the resonance that results in a dynamical trapping. When in the cavity region, the particle is a free particle but as soon as it moves away the gradient forces are restored. This mechanism leads to two important consequences: first, the average field intensity experienced by the specimen is much lower than in classical optical tweezers schemes. Secondly, the field dynamical decoupling/recoupling results in a transmission increase that is particle-dependent.

---

Particle-dependent signatures were indeed observed for 250 and 500 nm particles and permitted to conclude that simple transmission measurements can be used as a tool for particle differentiation. In particular, a qualitative differentiation was achieved by observing the transmission curves, that exhibit large differences in their mean value and in their shape. A quantitative confirmation of this analysis was carried out with the help of histograms and of statistical moments.

Finally, this principle was exploited for bacterial analysis. Seven species of living bacteria with different size, shape, motility and Gram-type were studied. It was possible to trap all of them with powers as low as few hundreds of microwatts and their Gram-type was determined by considering the transmission increase. Gram negative bacteria cause a larger resonance shift with respect to the Gram positive one. This can be explained by the larger deformability (that results in a larger overlap with the field) and by the presence of the lipopolysaccharides. Further bacterial identification, to the single species level, was not possible yet. However, some trends appeared and it has to be considered that the experiments were performed at high bacteria concentration. Several bacteria were trapped at the same time and this caused an averaging of other contribution like the motion in the cavity. For the future, single-cfu experiments are scheduled and it appears possible to obtain more information, in a similar way to the results obtained for single 250 and 500 nm nanoparticles.

However, the strong dependence of the signal on the structural properties of the cell wall opens the way to a large range of experiments that involve bacterial membranes. The most exciting application for such dependence could be the testing of the antibiotic susceptibility of bacteria. As a matter of fact, the effect of some antibiotics (like the polymyxines) is the breaking of the membrane and most of the antibiotics induce modifications in the cell wall by oxydative stress: it would be of great interest if it was possible to observe this phenomenon with our cavity. Nowadays, the susceptibility to an antibiotic is usually assessed through bacterial cultures: bacteria are cultured in presence (the test group) and in absence (the control group) of the antibiotic and the growth rate is detected. This is a long process, as several hours are necessary. Moreover, this technique does not allow for the determination of the time necessary for an antibiotic to act: remembering the growth curve in Fig. 5.7, during the first two hours the bacteria are adapting to the new environment. The use of our microfluidic-integrated optical cavity, on the other hand, could permit a fast detection of the viability of the bacteria with a simple transmission measurement. Moreover, the dynamics of the antibiotic action could be assessed by trapping the bacteria for the whole time and by recording the evolution of the transmission signal. A fast determination of antibiotics susceptibility is of crucial importance especially in diagnostics and it could allow to prevent the prescription of inappropriate antibiotics, a behaviour that is partly responsible for the rising phenomena of bacterial resistance.

Finally, an alternative possibility consists in studying the interactions between bacteria and bacteriophages (often referred to simply as phages). Phages are bacterium-specific viruses that infect bacteria and cause their death. The main interests in understanding the mechanisms

## **Chapter 6. Conclusions and perspectives**

---

that could led to the developement of phage therapies are twofolds: first, the use of phages as an alternative to antibiotics could overcome the problem of bacterial resistance. Secondly, they are much more specific than antibiotics. Some versions of the cavities used in this thesis, with different sizes, could be used in two ways: either by trapping a bacterium and observing its signal evolution while in presence of phages, either by directly trap a single phage and then to analyse the response to the subsequent trapping of a bacterium.

# Bibliography

- [1] Shinya Yoshioka and Shuichi Kinoshita. Wavelength-selective and anisotropic light-diffusing scale on the wing of the Morpho butterfly. *Proc. R. Soc. Lond. B*, 271(October 2003):581–587, 2004.
- [2] Glenn S Smith. Structural color of Morpho butterflies Structural color of Morpho butterflies. *American Journal of Physics*, 77(1010), 2009.
- [3] Jian Zi, Xindi Yu, Yizhou Li, Xinhua Hu, Chun Xu, Xingjun Wang, Xiaohan Liu, and Rongtang Fu. Coloration strategies in peacock feathers. *Proceedings of the National Academy of Sciences*, 100(22):12576–12578, 2003.
- [4] Eloïse Gaillou, Emmanuel Fritsch, Bertha Aguilar-Reyes, Benjamin Rondeau, Jeffrey Post, Alain Barreau, and Mikhail Ostroumov. Common gem opal: An investigation of micro- to nano-structure. *American Mineralogist*, 93(11-12):1865–1873, 2008.
- [5] Jean Pol Vigneron and Priscilla Simonis. Natural photonic crystals. In *Physica B: Condensed Matter*, volume 407, pages 4032–4036. Elsevier, 2012.
- [6] Jérémie Teyssier, Suzanne V Saenko, Dirk Van Der Marel, and Michel C Milinkovitch. Photonic crystals cause active colour change in chameleons. *Nature Communications*, 6:1–7, 2015.
- [7] Eileen Armstrong and Colm O’Dwyer. Artificial opal photonic crystals and inverse opal structures-fundamentals and applications from optics to energy storage. *Journal of Materials Chemistry C*, 3(24):6109–6143, 2015.
- [8] Eli Yablonovitch. Inhibited Spontaneous Emission in Solid-State Physics and Electronics. *Physical Review Letters*, 58(20):13–20, 1987.
- [9] Sajeev John. Strong localization of photons in certain disordered dielectric superlattices. *Physical Review Letters*, 58(23):2486–2489, 1987.
- [10] E. Yablonovitch, T. J. Gmitter, and K. M. Leung. Photonic band structure: The face-centered-cubic case employing nonspherical atoms. *Physical Review Letters*, 67(17):2295–2298, 1991.

## Bibliography

---

- [11] M. Plihal and A. A. Maradudin. Photonic band structure of two-dimensional systems: The triangular lattice. *Physical Review B*, 44(16):8565–8571, 1991.
- [12] S L McCall, P M Platman, R Dalichaouch, David Smith, and S Schultz. Microwave Propagation in Two-Dimensional Dielectric Lattices. *Physical Review*, 67(15):2017–2020, 1991.
- [13] W. M. Robertson, G. Arjavalingam, R. D. Meade, K. D. Brommer, A. M. Rappe, and J. D. Joannopoulos. Measurement of photonic band structure in a two-dimensional periodic dielectric array. *Physical Review Letters*, 68(13):2023–2026, 1992.
- [14] T Yoshie, A Scherer, C Ell, H M Gibbs, J Hendrickson, G Khitrova, O B Shchekin, D G Deppe, and G Rupper. Vacuum Rabi splitting with a single quantum dot in a photonic crystal nanocavity. *Nature*, 432(November):200–203, 2004.
- [15] Yosuke Terada, Keisuke Kondo, Ryotaro Abe, and Toshihiko Baba. Full C-band Si photonic crystal waveguide modulator. *Optics Letters*, 42(24):5110, 2017.
- [16] Kengo Nozaki, Takasumi Tanabe, Akihiko Shinya, Shinji Matsuo, Tomonari Sato, Hideaki Taniyama, and Masaya Notomi. Sub-femtojoule all-optical switching using a photonic-crystal nanocavity. *Nature Photonics*, 4(7):477–483, 2010.
- [17] Mindy R. Lee and Philippe M. Fauchet. Two-dimensional silicon photonic crystal based biosensing platform for protein detection. *Optics Express*, 15(8):4530, 2007.
- [18] Gary Shambat, Sri Rajasekhar Kothapalli, J Provine, Tomas Sarmiento, James Harris, Sanjiv Sam Gambhir, and Jelena Vučković. Single-cell photonic nanocavity probes. *Nano Letters*, 13(11):4999–5005, 2013.
- [19] Thijs van Leest and Jacob Caro. Cavity-enhanced optical trapping of bacteria using a silicon photonic crystal. *Lab on a Chip*, 13(22):4358, 2013.
- [20] J.-M. Lourtioz, H. Benisty, V. Berger, J.-M. Gérard, D. Maystre, and A. Tchelnokov. *Les cristaux photoniques ou la lumière en cage*. Hermès Science, 2003.
- [21] J. D. Joannopoulos, S. G. Johnson, J. N. Winn, and R. D. Meade. *Photonic crystals: molding the flow of light*. Princeton University Press, 2011.
- [22] Jelena Vučković, Marko Lončar, Hideo Mabuchi, and Axel Scherer. Optimization of the Q factor in photonic crystal microcavities. *IEEE Journal of Quantum Electronics*, 38(7):850–856, 2002.
- [23] J Jágerská, H Zhang, N. Le Thomas, and R. Houdré. Radiation loss of photonic crystal coupled-cavity waveguides. *Applied Physics Letters*, 95(11):11–13, 2009.
- [24] L. Collot, V. Lefèvre-Seguin, M. Brune, J. M. Raimond, and S. Haroche. Very high-q whispering-gallery mode resonances observed on fused silica microspheres. *EPL*, 23(5):327–334, 1993.



- [25] Ulagalandha Perumal Dharanipathy. *On the Investigation of Light-Matter Interactions in Slab Photonic Crystal Cavities*. PhD thesis, EPFL TH6092, 2014.
- [26] Susumu Noda, A Chutinan, and M Imada. Trapping and emission of photons by a single defect in a photonic bandgap structure. *Nature*, 407(6804):608–610, 2000.
- [27] Mindy R Lee and Philippe M Fauchet. Nanoscale microcavity sensor for single particle detection. *Optics Letters*, 33(7):756, 2008.
- [28] Zheng Han, Xavier Checoury, Laurent-Daniel Haret, and Philippe Boucaud. High quality factor in a two-dimensional photonic crystal cavity on silicon-on-insulator. *Optics Letters*, 36(10):1749, 2011.
- [29] Ulagalandha Perumal Dharanipathy, Momchil Minkov, Mario Tonin, Vincenzo Savona, and Romuald Houdré. High-Q silicon photonic crystal cavity for enhanced optical nonli-nearities. *Applied Physics Letters*, 105(10), 2014.
- [30] Takashi Asano, Yoshiaki Ochi, Yasushi Takahashi, Katsuhiko Kishimoto, and Susumu Noda. Photonic crystal nanocavity with a Q factor exceeding eleven million. *Optics Express*, 25(3):1769, 2017.
- [31] Shigeru Nakayama, Satomi Ishida, Satoshi Iwamoto, and Yasuhiko Arakawa. Effect of cavity mode volume on photoluminescence from silicon photonic crystal nanocavities. *Applied Physics Letters*, 98(17):1–4, 2011.
- [32] Masahiro Nomura, Katsuaki Tanabe, Iwamoto Satoshi, and Yasuhiko Arakawa. High-Q design of semiconductor-based ultrasmall photonic crystal nanocavity. *Optics Express*, 18(6):8144, 2010.
- [33] R. Frisch. Experimenteller Nachweis des Einsteinschen Strahlungsrückstosses. *Z. Phys*, 86(1-2):42–48, 1933.
- [34] A Ashkin. Acceleration and Trapping of Particles by Radiation Pressure. *Physical Review Letters*, 24(4):156–159, 1970.
- [35] A. Ashkin, J. M. Dziedzic, J. E. Bjorkholm, and Steven Chu. Observation of a single-beam gradient force optical trap for dielectric particles. *Optics Letters*, 11(5):288, 1986.
- [36] A. Ashkin, J. M. Dziedzic, and T. Yamane. Optical trapping and manipulation of single cells using infrared laser beams. *Nature*, 330(24):769–771, 1987.
- [37] Karel Svoboda and Steven M. Block. Biological Applications of Optical Forces. *Annual Review of Biophysics and Biomolecular Structure*, 23(1):247–285, 1994.
- [38] Yasuhiro Harada and Toshimitsu Asakura. Radiation forces on a dielectric sphere in the Rayleigh scattering regime. *Optics Communications*, 124(5-6):529–541, 1996.

## Bibliography

---

- [39] Keir C. Neuman and Steven M. Block. Optical trapping. *Review of Scientific Instruments*, 75(9):2787, 2004.
- [40] A Ashkin and Life Fellow. History of Optical Trapping and Manipulation of Small-Neutral Particle , Atoms , and Molecules. *IEEE Journal on Selected Topics in Quantum Electronics*, 6(6):841–856, 2000.
- [41] David G Grier. A revolution in optical manipulation. *Nature*, 424(6950):810–6, 2003.
- [42] P. Rodríguez-Sevilla, L. Labrador-Páez, D. Jaque, and P. Haro-González. Optical trapping for biosensing: Materials and applications. *Journal of Materials Chemistry B*, 5(46):9085–9101, 2017.
- [43] M. D. Wang, H. Yin, R. Landick, J. Gelles, and S. M. Block. Stretching DNA with optical tweezers. *Biophysical Journal*, 72(3):1335–1346, 1997.
- [44] Yuanjie Pang and Reuven Gordon. Optical trapping of a single protein. *Nano Letters*, 12(1):402–406, 2012.
- [45] Giuseppe Pesce, Giulia Rusciano, Antonio Sasso, Rachele Isticato, Teja Sirec, and Ezio Ricca. Surface charge and hydrodynamic coefficient measurements of *Bacillus subtilis* spore by optical tweezers. *Colloids and Surfaces B: Biointerfaces*, 116:568–575, 2014.
- [46] Kamilla Norregaard, Ralf Metzler, Christine M. Ritter, Kirstine Berg-Sørensen, and Lene B. Oddershede. Manipulation and Motion of Organelles and Single Molecules in Living Cells. *Chemical Reviews*, 117(5):4342–4375, 2017.
- [47] Patrick Lie Johansen, Federico Fenaroli, Lasse Evensen, Gareth Griffiths, and Gerbrand Koster. Optical micromanipulation of nanoparticles and cells inside living zebrafish. *Nature Communications*, 7:1–8, 2016.
- [48] Onofrio M. Maragò, Philip H. Jones, Pietro G. Gucciardi, Giovanni Volpe, and Andrea C. Ferrari. Optical trapping and manipulation of nanostructures. *Nature Nanotechnology*, 8(11):807–819, 2013.
- [49] K Svoboda and S M Block. Optical trapping of metallic Rayleigh particles. *Optics letters*, 19(13):930–2, 1994.
- [50] O M Maragò, P H Jones, F Bonaccorso, V Scardaci, P G Gucciardi, A G Rozhin, and A C Ferrari. Femtonewton Force Sensing with Optically Trapped Nanotubes. *Nano Letters*, 8(10):3211–3216, 2008.
- [51] Thomas Rodgers, Satoru Shoji, Zouheir Sekkat, and Satoshi Kawata. Selective Aggregation of Single-Walled Carbon Nanotubes Using the Large Optical Field Gradient of a Focused Laser Beam. *Physical Review Letters*, 101(September):127402, 2008.
- [52] Liselotte Jauffred, Andrew C Richardson, and Lene B Oddershede. Three-Dimensional Optical Control of Individual Quantum Dots. *Nano Letters*, 8(10):3376–3380, 2008.

- [53] Alexander S Urban, Sol Carretero-palacios, Andrey A Lutich, and Theobald Lohm. Nanoscale nanoparticles : fundamentals , applications , and perspectives. *Nanoscale*, 6:4458–4474, 2014.
- [54] Erik Hebestreit, Martin Frimmer, René Reimann, and Lukas Novotny. Sensing Static Forces with Free-Falling Nanoparticles. *Physical Review Letters*, 121(6):1–5, 2018.
- [55] T. W. Hänsch and A.L. Schawlow. Cooling of gases by laser radiation. *Optics Communications*, 13(1):68–69, 1975.
- [56] Li Tongcang, Simon Kheifets, and Mark G Raizen. Millikelvin cooling of an optically trapped microsphere in vacuum. *Nature Physics*, 7(7):527–530, 2011.
- [57] Jan Gieseler, Bradley Deutsch, Romain Quidant, and Lukas Novotny. Subkelvin parametric feedback cooling of a laser-trapped nanoparticle. *Physical Review Letters*, 109(10):1–5, 2012.
- [58] John David Jackson. *Classical Electrodynamics*. 1962.
- [59] O Latinne, C. J. Joachain, and M. Dörr. Atomic hydrogen in a superintense high-frequency field: Testing the dipole approximation. *EPL*, 26(5):333–338, 1994.
- [60] Edward M. Purcell and Carlton R. Pennypacker. Scattering and absorption of light by small particles. *The Astrophysical Journal*, 186:705–714, 1973.
- [61] B. T. Draine. The discrete-dipole approximation and its application to interstellar graphite grains. *The Astrophysical Journal*, 333:848–872, 1988.
- [62] P. W. Smith, P. J. Maloney, and A. Ashkin. Use of a liquid suspension of dielectric spheres as an artificial Kerr medium. *Optics Letters*, 7(8):347, 2008.
- [63] Lukas Novotny and Bert Hecht. *Principles of Nano-Optics*. Cambridge University Press, Cambridge, second edition, 2012.
- [64] Jeffrey E. Melzer and Euan McLeod. Fundamental Limits of Optical Tweezer Nanoparticle Manipulation Speeds. *ACS Nano*, 12(3):2440–2447, 2018.
- [65] Henrik Bruus. *Theoretical Microfluidics (Oxford Master Series in Physics)*. 18, 2007.
- [66] M. B. Rasmussen, L. B. Oddershede, and H. Siegmundfeldt. Optical tweezers cause physiological damage to Escherichia coli and Listeria bacteria. *Applied and Environmental Microbiology*, 74(8):2441–2446, 2008.
- [67] Arthur Ashkin. Optical trapping and manipulation of neutral particles. *Proc. Natl. Acad. Sci. USA*, 94(May):4853–4860, 1997.
- [68] Changan Xie, Yong-qing Li, Wei Tang, and Ronald J Newton. Study of dynamical process of heat denaturation in optically trapped single microorganisms by near-infrared Raman spectroscopy. *Journal of Applied Physics*, 94(6138), 2003.

## Bibliography

---

- [69] Mario Tonin, Stefan Bálint, Pau Mestres, Ignacio A Martínez, and Dmitri Petrov. Electrophoretic mobility of a growing cell studied by photonic force microscope microscope. *Applied Physics Letters*, 97(November 2010):203704, 2010.
- [70] Lukas Novotny, Randy X Bian, and X Sunney Xie. Theory of Nanometric Optical Tweezers. *Physical Review Letters*, 79(4), 1997.
- [71] Maurizio Righini, A. Zelenina, and Romain Quidant. Parallel and selective trapping in a patterned plasmonic landscape. *Nature Physics*, 3:477–480, 2007.
- [72] Maurizio Righini, Giovanni Volpe, Christian Girard, Dmitri Petrov, and Romain Quidant. Surface Plasmon Optical Tweezers : Tunable Optical Manipulation in the Femtonewton Range. *Physical Review Letters*, 100(186804):8–11, 2008.
- [73] Kai Wang and Kenneth B Crozier. Plasmonic trapping with a gold nanopillar. *ChemPhysChem*, 13(11):2639–2648, 2012.
- [74] Weihua Zhang, Lina Huang, Christian Santschi, and Olivier J F Martin. Trapping and Sensing 10 nm Metal Nanoparticles Using Plasmonic Dipole Antennas. *Nano Letters*, pages 1006–1011, 2010.
- [75] Changjun Min, Zhe Shen, Junfeng Shen, Yuquan Zhang, Hui Fang, and Guanghui Yuan. Focused plasmonic trapping of metallic particles. *Nature Communications*, 4:1–7, 2013.
- [76] S Kawata and T Tani. Optically driven Mie particles in an evanescent field along a channeled waveguide. *Optics Letters*, 21(21):1768, 1996.
- [77] Balpreet Singh Ahluwalia, Peter Mccourt, Thomas Huser, and Olav Gaute Hellesø. Optical trapping and propulsion of red blood cells on waveguide surfaces. *Optics Express*, 18(20):4–6, 2010.
- [78] Allen H J Yang, Sean D Moore, Bradley S Schmidt, Matthew Klug, Michal Lipson, and David Erickson. Optical manipulation of nanoparticles and biomolecules in sub-wavelength slot waveguides. *Nature*, 457(7225):71–75, 2009.
- [79] S E Skelton, M Sergides, R Patel, E Karczewska, O M Maragò, and P H Jones. Journal of Quantitative Spectroscopy & Radiative Transfer Evanescent wave optical trapping and transport of micro- and nanoparticles on tapered optical fibers. *Journal of Quantitative Spectroscopy and Radiative Transfer*, 113:2512–2520, 2012.
- [80] Haotian Wang, Xiang Wu, and Deyuan Shen. Localized optical manipulation in optical ring resonators. *Optics Express*, 23(21):27650, 2015.
- [81] Ovidiu Toader, Sajeev John, and Kurt Busch. Optical trapping, Field enhancement and Laser cooling in photonic crystals. *Optics Express*, 8(3):217, 2009.
- [82] Adel Rahmani and Patrick C Chaumet. Optical trapping near a photonic crystal. *Optics Express*, 14(13):6353, 2006.

- [83] Michael Barth and Oliver Benson. Manipulation of dielectric particles using photonic crystal cavities. *Applied Physics Letters*, 89(253114):1–4, 2006.
- [84] Sudeep Mandal, Julie M. Goddard, and David Erickson. A multiplexed optofluidic biomolecular sensor for low mass detection. *Lab on a Chip*, 9(20):2924, 2009.
- [85] Mario Henri Lucien Tonin. *Piégeage optique résonant et analyse du mouvement de nanoparticules piégées dans des cristaux photoniques à cavités creuses*. PAR. PhD thesis, EPFL TH6874, 2016.
- [86] R. Therisod, M. Tardif, P. R. Marcoux, E. Picard, J. B. Jager, E. Hadji, D. Peyrade, and R. Houdré. Gram-type differentiation of bacteria with 2D hollow photonic crystal cavities. *Applied Physics Letters*, 113(11), 2018.
- [87] M. Tardif, J. B. Jager, P. R. Marcoux, K. Uchiyamada, E. Picard, E. Hadji, and D. Peyrade. Single-cell bacterium identification with a SOI optical microcavity. *Applied Physics Letters*, 109(13), 2016.
- [88] Pau Mestres, Johann Berthelot, Srdjan S. Acimovic, and Romain Quidant. Unraveling the optomechanical nature of plasmonic trapping. *Light: Science and Applications*, 5(7):1–14, 2016.
- [89] Mathieu L. Juan, Reuven Gordon, Yuanjie Pang, Fatima Eftekhari, and Romain Quidant. Self-induced back-action optical trapping of dielectric nanoparticles. *Nature Physics*, 5(12):915–919, 2009.
- [90] P. Gravesen, J. Branebjerg, and O. Søndergård jensen. Microfluidics - a review. *Journal of Micromechanics and Microengineering*, 3:168–182, 1993.
- [91] Jessamine M K Ng, Abraham D Stroock, and George M Whitesides. Components for integrated poly ( dimethylsiloxane ) microfluidic systems. *Electrophoresis*, 23:3461–3473, 2002.
- [92] James Friend and Leslie Yeo. Fabrication of microfluidic devices using polydimethylsiloxane. *Biomicrofluidics*, 4(2):1–5, 2010.
- [93] Daniel Figeys and Devanand Pinto. Lab-on-a-Chip: A Revolution in Biological and Medical Sciences. *Analytical Chemistry*, 72(9):330 A–335 A, 2000.
- [94] Demetri Psaltis, Stephen R Quake, and Changhuei Yang. Developing optofluidic technology through the fusion of microfluidics and optics. *Nature*, 442(7101):381–386, 2006.
- [95] Lin Pang, H Matthew Chen, Lindsay M Freeman, and Yeshaiahu Fainman. Optofluidic devices and applications in photonics, sensing and imaging. *Lab on a Chip*, 12(19):3543–3551, 2012.

## Bibliography

---

- [96] Arvind Chandrasekaran, Ashwin Acharya, Jian Liang You, Kim Young Soo, Muthukumar Packirisamy, Ion Stiharu, and Andre Darveau. Hybrid integrated silicon microfluidic platform for fluorescence based biodetection. *Sensors*, 7(9):1901–1915, 2007.
- [97] Ali Kemal Yetisen, Muhammad Safwan Akram, and Christopher R Lowe. Paper-based microfluidic point-of-care diagnostic devices. *Lab on a Chip*, 13(12):2210–2251, 2013.
- [98] Holger Becker and Claudia Gärtner. Polymer microfabrication methods for microfluidic analytical applications. *Electrophoresis*, 21:12–26, 2000.
- [99] Marc A Unger, Hou Pu Chou, Todd Thorsen, Axel Scherer, and Stephen R Quake. Monolithic microfabricated valves and pumps by multilayer soft lithography. *Science*, 288(5463):113–116, 2000.
- [100] Teruo Fujii. PDMS-based microfluidic devices for biomedical applications. In *Micro-electronic Engineering*, volume 61-62, pages 907–914, 2002.
- [101] Chia Wen Tsao. Polymer microfluidics: Simple, low-cost fabrication process bridging academic lab research to commercialized production. *Micromachines*, 7(12), 2016.
- [102] Younan Xia and George M. Whitesides. Soft Lithography. *Annual Review of Materials Science*, 28(1):153–184, 1998.
- [103] John A Rogers and Ralph G Nuzzo. Recent progress in soft lithography. *Materials Today*, 8(2):50–56, 2005.
- [104] S Talaei, O Frey, P. D. van der Wal, N. F. de Rooij, and M. Koudelka-Hep. Hybrid microfluidic cartridge formed by irreversible bonding of SU-8 and PDMS for multi-layer flow applications. In *Procedia Chemistry*, volume 1, pages 381–384. Elsevier B.V., 2009.
- [105] Mario Tonin, Nicolas Descharmes, and Romuald Houdré. Hybrid PDMS/glass microfluidics for high resolution imaging and application to sub-wavelength particle trapping. *Lab on a Chip*, 16(3):465–470, 2016.
- [106] <https://cmi.epfl.ch/photo/files/simulation/resist.simulation.php>.
- [107] <https://cmi.epfl.ch/photo/VPG200.php>.
- [108] [https://cmi.epfl.ch/ebeam/Writing\\_strategy.php](https://cmi.epfl.ch/ebeam/Writing_strategy.php).
- [109] <http://www.gel.usherbrooke.ca/casino/What.html>.
- [110] Xu Hou, Yu Shrike Zhang, Grissel Trujillo De Santiago, Mario Moisés Alvarez, João Ribas, Steven J. Jonas, Paul S. Weiss, Anne M. Andrews, Joanna Aizenberg, and Ali Khademhosseini. Interplay between materials and microfluidics. *Nature Reviews Materials*, 2(5), 2017.
- [111] <https://cmi.epfl.ch/etch/AMS200.php>.

- [112] <https://www.adnano-tek.com/magnetron-sputtering-deposition-msd.html>.
- [113] Robert K Waits. Planar magnetron sputtering. *Journal of Vacuum Science and Technology*, 15(2):179–187, 1978.
- [114] Nicolas Descharmes. *Resonant Optical Trapping in Microfluidic-Integrated Hollow Photonic Crystal Cavities*. PhD thesis, EPFL TH6874, 2013.
- [115] Nicolas Descharmes, Ulagalandha Perumal Dharanipathy, Zhaolu Diao, Mario Tonin, and Romuald Houdré. Single particle detection, manipulation and analysis with resonant optical trapping in photonic crystals. *Lab on a Chip*, 13(16):3268, 2013.
- [116] S Lopera and R D Mansano. Plasma-Based Surface Modification of Polydimethylsiloxane for PDMS-PDMS Molding. *ISRN Polymer Science*, 2012:1–5, 2012.
- [117] [https://www.electrolube.com/products/thermal-management/tbs/rtvs\\_and\\_bonding\\_products/](https://www.electrolube.com/products/thermal-management/tbs/rtvs_and_bonding_products/).
- [118] World Health Organization. <https://www.who.int/news-room/fact-sheets/detail/antibiotic-resistance>, 2018.
- [119] Erin R Sanders. Aseptic Laboratory Techniques : Volume Transfers with Serological Pipettes and Micropipettors. (May):1–12, 2012.
- [120] Manon Tardif. *Piégeage et caractérisation de bactéries par cristaux photoniques*. PhD thesis, Université Grenoble Alpes, 2018.
- [121] Yoshihiro Akahane, Takashi Asano, Bong-shik Song, and Susumu Noda. Fine-tuned high- Q photonic-crystal nanocavity. *Optics Express*, 13(4):1908–1910, 2005.
- [122] Guk-Hyun Kim, Yong-Hee Lee, Akihiko Shinya, and Masaya Notomi. Coupling of small, low-loss hexapole mode with photonic crystal slab waveguide mode. *Optics Express*, 12(26):6624, 2005.
- [123] Chun-wei Liao, Yao-tsu Yang, Sheng-wen Huang, and Ming-chang M Lee. Fiber-Core-Matched Three-Dimensional Adiabatic Tapered Couplers for Integrated Photonic Devices. *Journal of Lightwave Technology*, 29(5):770–774, 2011.
- [124] Hemant Sankar, Amit Kumar, Varun Srivastava, and Suchandan Pal. Coupling light in photonic crystal waveguides : A review. *Photonics and Nanostructures - Fundamentals and Applications*, 20:41–58, 2016.
- [125] Oscar A. Jimenez Gordillo, Mohammad Amin Tadayon, You-chia Chang, and Michal Lipson. 3D photonic structure for plug-and-play fiber to waveguide coupling. In *CLEO 2018*, page STh4B.7, 2018.
- [126] Tymon Barwicz, Senior Member, Senior Member, Bo Peng, Robert Leidy, Alexander Janta-polczynski, Thomas Houghton, Marwan Khater, Senior Member, Swetha Kamalapurkar, Sebastian Engelmann, Paul Fortier, Nicolas Boyer, William M J Green, Senior

## Bibliography

---

- Member, and Senior Member. Integrated Metamaterial Interfaces for Self-Aligned Fiber-to-Chip Coupling in Volume Manufacturing. *IEEE Journal of Selected Topics in Quantum Electronics*, 25(3):1–13, 2019.
- [127] Nicolas Deschermes, Ulagalandha Perumal Dharanipathy, Zhaolu Diao, Mario Tonin, and Romuald Houdré. Observation of backaction and self-induced trapping in a planar hollow photonic crystal cavity. *Physical Review Letters*, 110(12):1–4, 2013.
- [128] Erwin J.G. Peterman, Frederick Gittes, and Christoph F. Schmidt. Laser-induced heating in optical traps. *Biophysical Journal*, 84(2 1):1308–1316, feb 2003.
- [129] Nicolas Deschermes, Ulagalandha Perumal Dharanipathy, Zhaolu Diao, Mario Tonin, and Romuald Houdré. Single particle detection, manipulation and analysis with resonant optical trapping in photonic crystals. *Lab on a Chip*, 13(16):3268–3274, aug 2013.
- [130] M. Tonin, F. M. Mor, L. Forró, S. Jeney, and R. Houdré. Thermal fluctuation analysis of singly optically trapped spheres in hollow photonic crystal cavities. *Applied Physics Letters*, 109(24), dec 2016.
- [131] R. S. Dutra, N. B. Viana, P. A. Maia Neto, and H. M. Nussenzveig. Absolute calibration of forces in optical tweezers. *Physical Review A - Atomic, Molecular, and Optical Physics*, 90(1):1–13, 2014.
- [132] S. Karel. Biological Applications of Optical Forces. *Annual Review of Biophysics and Biomolecular Structure*, 23(1):247–285, 2002.
- [133] Kirstine Berg-Sørensen and Henrik Flyvbjerg. Power spectrum analysis for optical tweezers. *Review of Scientific Instruments*, 75(3):594–612, 2004.
- [134] Steven M. Block and Keir C. Neuman. All-optical trapping. *Review of Scientific Instruments*, 75(2787), 2004.
- [135] Raquel Quatrini and D. Barrie Johnson. Microbiomes in extremely acidic environments: functionalities and interactions that allow survival and growth of prokaryotes at low pH. *Current Opinion in Microbiology*, 43:139–147, 2018.
- [136] L Weiss. Survival of Bacteria at Low pH and High Temperature. *Limnology and Oceanography*, 18(November):877 – 883, 1973.
- [137] Alexandre Bagnoud, Karuna Chourey, Robert L. Hettich, Ino De Bruijn, Anders F. Andersson, Olivier X. Leupin, Bernhard Schwyn, and Rizlan Bernier-Latmani. Reconstructing a hydrogen-driven microbial metabolic network in Opalinus Clay rock. *Nature Communications*, 7:1–10, 2016.
- [138] Naji M. Bassil, Nicholas Bryan, and Jonathan R. Lloyd. Microbial degradation of isosaccharinic acid at high pH. *ISME Journal*, 9(2):310–320, 2015.



- [139] Farouk Karoum, J. W. Commissiong, N. H. Neff, and R. J. Wyatt. Biochemical evidence for uncrossed and crossed locus coeruleus projections to the spinal cord. *Brain Research*, 196(1):237–241, 1980.
- [140] Sean McMahon and John Parnell. Weighing the deep continental biosphere. *FEMS Microbiology Ecology*, 87(1):113–120, 2014.
- [141] C. Kato, L. Li, Y. Nakamura, Y. Nogi, J. Tamaoka, and K. Horikoshi. Properties of Hyper-Barophilic Bacteria Isolated from the Mariana Trench at a Depth of 11,000m. *the Review of High Pressure Science and Technology*, 7(4):1274–1276, 1998.
- [142] Ron Sender, Shai Fuchs, and Ron Milo. Revised Estimates for the Number of Human and Bacteria Cells in the Body. *PLoS biology*, 14(8):e1002533, 2016.
- [143] Cynthia L. Sears. A dynamic partnership: Celebrating our gut flora. *Anaerobe*, 11(5):247–251, 2005.
- [144] C Lee Ventola. The antibiotic resistance crisis: part 1: causes and threats. *P & T: A peer-reviewed journal for formulary management (2015)*, 40(4):277–83, 2015.
- [145] K. D. Young. The Selective Value of Bacterial Shape. *Microbiology and Molecular Biology Reviews*, 70(3):660–703, 2006.
- [146] Petra Anne Levin and Esther R. Angert. Small but mighty: Cell size and bacteria. *Cold Spring Harbor Perspectives in Biology*, 7(7):1–11, 2015.
- [147] Michael Silverman and Melvin Simon. Flagellar rotation and the mechanism of bacterial motility. *Nature*, 249(5452):73–74, 1974.
- [148] E. M. Purcell. Life at low Reynolds number. *American Journal of Physics*, 45(1):3–11, 1977.
- [149] Gerard J. Tortora, Berdell R. Funke, and Christine L. Case. *Microbiology: An Introduction*. Harlow:Pearson Education, twelfth ed edition, 2016.
- [150] Thomas Silhavy, Daniel Kahne, and Suzanne Walker. The bacterial cell envelope. *Cold Spring Harbor perspectives in biology*, 2(5):1–16, 2010.
- [151] C. Gram. Über die isolierte Färbung der Schizomyceten in Schnitt- und Trockenpräparaten. *Fortschr Med*, 2:185–189, 1884.
- [152] Ann C. Smith and Marise A. Hussey. Gram stain protocols. *American Society for Microbiology*, (September 2005):14852, 2005.
- [153] T. J. Beveridge. Use of the Gram stain in microbiology. *Biotechnic and Histochemistry*, 76(3):111–118, 2001.
- [154] <https://ib.bioninja.com.au/options/untitled/b1-microbiology-organisms/gram-staining.html>.

## Bibliography

---

- [155] T. J. Beveridge. Mechanism of gram variability in select bacteria. *Journal of Bacteriology*, 172(3):1609–1620, 1990.
- [156] Sujata Mani and Ram Naresh Bharagava. *Exposure to Crystal Violet, Its Toxic, Genotoxic and Carcinogenic Effects on Environment and Its Degradation and Detoxification for Environmental Safety*, pages 71–104. Springer International Publishing, Cham, 2016.
- [157] R. G. Benedict, J. Corman, E.S. Sharpe, C. E. Kemp, H. H. Hall, and Jackson R. W. Preservation of microorganisms by freeze-drying. *Applied Microbiology*, 6(6):401, 1958.
- [158] R. J. Heckly. Preservation of Microorganisms. *Advances in Applied Microbiology*, 24:1–53, 1978.
- [159] M B Kupletskaya and A I Netrusov. Viability of Lyophilized Microorganisms after 50 Year Storage. *Microbiology*, 80(6):850–853, 2011.
- [160] Yukie Miyamoto-shinohara, Takashi Imaizumi, Junji Sukenobe, and Yukie Murakami. Survival Rate of Microbes after Freeze-Drying and Long-Term Storage. *Cryobiology*, 41:251–255, 2000.
- [161] M. D. Rolfe, C. J. Rice, S. Lucchini, C. Pin, A. Thompson, A. D. S. Cameron, M. Alston, M. F. Stringer, R. P. Betts, J. Baranyi, M. W. Peck, and J. C. D. Hinton. Lag Phase Is a Distinct Growth Phase That Prepares Bacteria for Exponential Growth and Involves Transient Metal Accumulation. *Journal of Bacteriology*, 194(3):686–701, feb 2012.
- [162] C. Forsberg and H.J. Rogers. Autolytic Enzymes in Growth of Bacteria. *Nature*, 229:272–273, 1971.
- [163] K. C. Rice and K. W. Bayles. Molecular Control of Bacterial Death and Lysis. *Microbiology and Molecular Biology Reviews*, 72(1):85–109, mar 2008.
- [164] Daniel López, Hera Vlamakis, and Roberto Kolter. Biofilms. *Cold Spring Harbor perspectives in biology*, pages 1–12, 2010.
- [165] Virginia Vadillo-Rodriguez, Sarah R. Schooling, and John R. Dutcher. In situ characterization of differences in the viscoelastic response of individual gram-negative and gram-positive bacterial cells. *Journal of Bacteriology*, 191(17):5518–5525, 2009.

# Acknowledgements

The years spent during this PhD thesis leave me with so many people to thank: at times, it was a difficult journey, but I met so many nice people that I will always keep the best memories of my stay at EPFL. First of all, I would like to sincerely thank my supervisor, Prof. Romuald Houdré, for accepting me as a PhD student at the beginning and for constant support during these four years. He gave me the opportunity to find my place in Physics, the cleanroom, and to acquire scientific self-confidence through the perfect balance between independence and guidance. At any time it was possible to just pass by Romuald's office and discuss and he was always of great help. I would like to thank him especially for his support during tough times, he was always there when I needed him, and one lesson that I will keep with me is that it is important to do things step by step and that "le mieux est l'ennemi du bien". Moreover, he is one of the most knowledgeable people that I had the chance to meet in many non-academic fields: besides the technical discussions, I will miss the ones about cooking and about more or less exotic ingredients, as well as exchanging opinions about life in general. Finally, I would like to thank Romuald for helping me in improving my French, it allowed me to get the most authentic experience of living in a French-speaking country.

I also would like to thank the other members of the group: a big thanks goes to Mario, for its patience in teaching me all about fabrication and optical measurements and for sharing his deep love for optics, but also for his help during the ski weekends and for the nice afternoon breaks at Arcadie. Thanks to Mohamed, for the scientific discussions, for his enthusiasm for photonics and for allowing me to get in touch with the American culture. A big thanks to Jun, for being such a nice person, for his sincerity in facing the world and for making me think that sometimes things are just simple. Finally, a huge thanks to Nicolas, for his friendship and for his support. He is one of the most open people that I met, with an always positive attitude and a lot of enthusiasm and kindness, it was easy to become friends. During the writing of the thesis it was of great help to interact with him, and he also took the time to read my manuscript, thanks also for that.

I would like to thank all the people that I met in Grenoble: our collaboration was the best experience both scientifically and personally and it showed that in a collaborative and enjoyable environment good results always arrive. Thanks to Emmanuel and David for their kindness and scientific advices, to Manu for his endless enthusiasm and motivation and to Pierre for teaching me so many things about bacteria and for his scientific rigour. I would also like to

## Acknowledgements

---

thank him for accepting to be part of the jury and to carefully review my manuscript. Last but far from least, a huge thanks goes to Manon. We shared experiments and conferences but also holidays, dinners and, at times, the loneliness that PhD students can experience during tough moments. Sharing all of this with a friend makes a big difference and I'm very grateful for that.

All the results achieved in this thesis would not have been possible without the help of the "cleanroom family" in the Institute of Physics. I would like to thank Nicolas, Damien, Yoan, Jonathan, Adrien and Florian for their constant support. For any technical problem, they always found the best solution in the shortest time. A big thanks also goes to Jean-Michel, Nino, Mauro, Fulvio, Pascal, Benny and François for their precious advices and for helping me with sometimes capricious machines. Moreover, I would like to thank all of them for making the time spent inside and outside the cleanroom such an enjoyable experience, those moments will be missed.

A big thanks also goes to CMi staff, especially to Zdenek and Joffrey for ebeam and etching, without whom the quality of my samples would have been much lower. They were always available for discussion and for solving problems and they taught me so much about processing. Also, I would like to thank Rémy, Cyrille and Patrick for usefull discussions.

Moreover, I would like to thank all the members of the IPHYS with whom I interacted all through the thesis, in particular Florence and Andrea for the IT support, Laurence, Nadja and Diane for admisitrative tasks, Anh for everything related to the EDPY doctoral school and for being the best office neighbour, Gilles and Adrien from the mechanical workshop for their precious help on the experimental setup.

Thanks to my friends in Lausanne for making my stay so pleasant, and to my friends abroad for their support despite the distance that has separated us. A special thanks goes to Davide, many of the results in this thesis were achieved thanks to his loving support. We shared tough and happy moments and, besides the emotional support, all over the thesis he was a source of inspiration for committment, scientific rigour and patience. Thanks to him I had always the feeling that at the end things would work fine and I sincerely thank him for that.

Finally, my deepest thanks goes to my parents and to my sister. Their love and support accompanied me all through my life and studies and the efforts they did to support me mean a lot to me: thank you from the deep of my heart.

*Lausanne, 25 juillet 2019*

Rita

# RITA THERISOD



Phone: +41789335282 | e-mail: rita.therisod@gmail.com | Skype: rita.therisod  
Address: 59, rue du Maupas, 1004, Lausanne (CH)  
Nationality : italian | Date of birth: June 12<sup>th</sup> 1986

## PROFILE

I am a physicist with experience in micro- and nano-fabrication, microfluidics, optical systems and biosensing

## EDUCATION

### ECOLE POLYTECHNIQUE FEDERALE DE LAUSANNE

*PhD in Physics*

*Supervisor:* Prof. Romuald Houdré

Lausanne, CH  
February 2015 – August 2019

### UNIVERSITA' DEGLI STUDI DI PAVIA

*Master in Physics*

*Supervisors:* Prof. Franco Marabelli, Dr. Lucia Fornasari  
*Grade:* 103/110

Pavia, IT  
October 2010 – April 2013

### UNIVERSITA' DEGLI STUDI DI PAVIA

*Bachelor in Physics*

*Supervisor:* Prof. Franco Marabelli  
*Grade:* 89/110

Pavia, IT  
October 2005 – July 2010

## CORE EXPERIENCE

### ECOLE POLYTECHNIQUE FEDERALE DE LAUSANNE

*Doctoral candidate*

Microfluidic-integrated photonic crystals for optical trapping applications

- Fabrication of Silicon photonic crystal cavities and integration with microfluidic layers
- Optical characterization: transmission and surface emission measurements
- Bacterial culture and manipulation
- Optical trapping of nanoparticles and living bacteria. Distinction of particles sizes and bacterial Gram-type determination.

Lausanne, CH  
January 2015 – August 2019

### UNIVERSITA' DEGLI STUDI DI PAVIA

*Master thesis student*

*Thesis title:* Sensitivity of localized plasmons and plasmonic polaritons to refractive index variations.

- Experimental demonstration of the refractive index dependence in the response of plasmonic structures.

Pavia, IT  
October 2010 - April 2013

## ADDITIONAL EXPERIENCE

### ACADEMIC TEACHING/SUPERVISING

- Responsible for two TP4 projects and two stages at EPFL.
- Assistant for the following courses at EPFL:
  - Optics I and Optics III in English
  - Optique I, Optique II and Physique Générale II in French

### HIGH-SCHOOL TEACHING

- Teaching Mathematics and Physics in High School, in Italian and in French

Aosta, IT  
September 2013 – September 2014

## TECHNICAL SKILLS

- *Clean room processing*: ebeam lithography, UV lithography, dry etching, DRIE, wet etching, laser writing, excimer laser etching, PDMS, scanning electron microscopy.
- *Optical Spectroscopy and characterization*: refractometry, ellipsometry, lock-in detection.
- *Imaging and interferometric systems*: laser beam expansion/cleaning, lens systems, fiber coupling.
- *Biology*: culture and manipulation of Class 1 bacteria.
- *Softwares*: L-Edit, LabView, Matlab, CAD (AutoCAD), Microsoft office package, CATS, Layout Beamer, Inkscape, Latex.
- *Professional communication*: presenter at several international conferences. Writing of scientific papers.

## PERSONAL AND INTERPERSONAL SKILLS

I am independent in the organization of the work and patient and rigorous in the fabrication processing and during the experiments. I usually have good relationships with my colleagues and with the students. I like to exchange ideas and information with my colleagues.

## OTHER INTERESTS

My favourite free-time activity is cooking. I like to try new recipes and ingredients and to keep up-to-date with cooking trends and techniques. I also enjoy outdoor activities that allow me to see beautiful natural scenarios. Cycling, trekking and paddling are among my favorites.

## LANGUAGES

**Italian**: Native speaker

**French**: technical and conversational proficiency (C1 certified by DALF)

**English**: technical and conversational proficiency (C1)



